Technische Universität Dresden

Advanced Focused Ion Beam: Preparation Optimization and Damage Mitigation

Jin Huang

von der Fakultät Elektrotechnik und Informationstechnik der
Technische Universität Dresden

zur Erlangung des akademischen Grades eines

Doktoringenieurs

(Dr.-Ing.)

genehmigte Dissertation

Vorsitzender:	Prof. Dr. rer. nat. Stefan Mannsfeld (TU Dresden)	
Gutachter:	Prof. Dr. rer. nat. Ehrenfried Zschech (Fraunhofer-IKTS Dresden)	
	Prof. Dr.-Ing. Christian Boit (TU Berlin)	Tag der Einreichung 03.05.2018
	Prof. Dr. Wolfhard Möller (TU Dresden)	Tag der Verteidigung 07.12.2018

Acknowledgement

This doctoral thesis is the invaluable result from the project "MaKiZu" (material integration and kinetics of reliability-limiting degradation mechanisms in 1D-electronic systems), funded by the Federal Ministry for Education and Research of Germany. Cfaed (Center for Advancing Electronics Dresden) and DCN (Dresden Center for Nanoanalysis) from Technical University of Dresden, as well as Thermo Fisher Scientific (formerly FEI) have also given tremendous amount of support throughout my entire PhD time.

I would like to thank my supervisor Prof. Ehrenfried Zschech and Post-Doc Dr. Markus Löffler, who continuously give me support and guidance, professionally and morally, in this four years journey. My gratitude also goes to the colleagues who have worked with me and contributed their irreplaceable efforts to make this work possible.

To the love from my family and friends. You have always been there for me, at a place where I call home again, helping me make it through the darkest nights.

Thank You.

May 2018 in Dresden

Table of Contents

Abstract VII

List of Abbreviations IX

List of Symbols X

List of Figures XI

List of Tables XVI

Motivation 1

Introduction to Focused Ion Beam 7

2.1 Principles of Focused Ion Beam 8

2.2 Typical FIB Applications 12

2.2.1 Cross-section preparation 12

2.2.2 TEM lamella preparation 13

2.2.3 Circuit Modification 15

2.2.4 3D EDS and 3D EBSD analysis 16

References 19

Gallium Focused Ion Beam on Silicon 23

3.1 SEM study of gallium FIB milling rate of silicon 27

3.1.1 SEM experiment procedure 28

3.1.2 SEM experiment result 32

3.2 TEM study of gallium FIB induced silicon amorphization 34

3.2.1 Gallium FIB experiment procedures 34

3.2.2 TEM images and data interpretation 38

3.3 APT study of gallium FIB ion implantation in silicon 44

3.3.1 APT experiment procedures... 45

3.3.2 Data interpretation and visualization.. 54

References 58

Beam Induced Polishing System 61

4.1 BIPS hardware configuration.. 63

4.1.1 Argon supply line 64

4.1.2 Valve system 65

4.1.3 Liquid Nitrogen Cold Trap.. 66

4.1.4 Gas Injection System (GIS) port 68

4.1.5 Ionization nozzle 69

4.1.6 Sample holder... 71

4.2 BIPS experiment procedure and results 73

References 80

Dynamic Binary Collision Approximation and its FIB Application.........................81

5.1 Ion-beam induced damage generation and accumulation 85

5.2 Point Defect Density and Amorphous Layer Thickness...................................... 88

5.3 Amorphous layer thickness 90

5.4 Gallium concentration 93

5.5 Milling Rate 95

References 99

Discussion and Conclusions 103

6.1 Discussion of Experiments and Simulations 105

6.1.1 FIB milling rate 105

6.1.2 Gallium Ion Implantation 108

6.1.3 FIB-Induced Silicon Amorphization 110

6.1.4 Reduced Sample Damage and Optimization of FIB Sample Preparation 111

6.2 Conclusions 114

Abstract

Focused Ion Beam (FIB) is an important analytical and sample modification technique in the field of electron and ion microscopy. It has been widely used in different kinds of applications including semiconductor device failure analysis, material science research, nanoscale 3D tomography, as well as microstructure prototyping and surface modification. Recent developments from the rapid growing industry and our frontier research have posted new challenges on the FIB technology itself. Higher resolution has been realized by state-of-the-art hardware infrastructures and less sample destruction has been achieved by efficient operation recipes.

In this doctoral thesis, a study of advanced Focused Ion Beam sample preparation is presented, with the goal to prepare samples with low or no damage. The study is divided into two aspects according to various aspects in the FIB applications: sample damage and in-situ preparation. In the first aspect, sample damage, namely amorphization, ion implantation and FIB milling rate are investigated on crystalline silicon specimens with a gallium FIB tool. To study the ion-beam induced amorphous layer thickness under certain conditions, silicon specimens were prepared by FIB into specific geometry, so that the induced amorphous layer can be imaged and the thickness can be determined quantitatively using Transmission Electron Microscopy (TEM). Atom Probe Tomography (APT) was carried out to study the implanted ion concentration of gallium FIB prepared silicon specimens. In addition, the gallium FIB milling rate was also studied for a silicon substrate using Scanning Electron Microscopy (SEM). These experimental

results provide detailed information of beam-sample interactions from the FIB sample preparation. In order to gain a systematic understanding of the processes, as well as to be able to predict the outcome of a specific FIB recipe, a physics model and an adapted algorithm (TRIDYN) based on Binary Collision Approximation (BCA) were used for the simulation of FIB processes. The predicted results based on simulations were compared with experiments. The proposed model was successfully validated by the experimental results, i.e., the TRIDYN algorithm has the capability to provide predictions for the multi-step FIB sample preparation process and the respective recipes.

The other aspect involves a novel design of a hardware configuration of a SEM/FIB system add-on to perform in-situ surface modification tasks such as argon ion polishing of specimens. This Beam Induced Polishing System (BIPS) overcomes the disadvantages that some of the ex-situ methods have, and it completes some of the advanced FIB recipes for extremely thin and pristine specimens. In the thesis, the functionality of a BIPS system is explained in detail, and first experimental results are shown to demonstrate the proof of concept of the system.

To summarize, this doctoral thesis presents an adapted algorithm, which is validated by experiments, to simulate the multi-step Focused Ion Beam process for recipes of low-damage sample preparation; A novel in-situ experiment system BIPS is also introduced, providing an option to complement SEM/FIB systems for advanced FIB sample preparation recipes.

List of Abbreviations

1D	One-dimension(al)
2D	Two-dimension(al)
3D	Three-dimension(al)
APT	Atom Probe Tomography
BCA	Binary Collision Approximation
BIPS	Beam Induced Polishing System
c-a	Crystalline-amorphous
CMOS	Complementary Metal Oxide Semiconductor
EBSD	Electron Backscatter Diffraction
EDS	Energy-Dispersive X-ray Spectroscopy
FIB	Focused Ion Beam
FinFET	Fin Field-Effect Transistor
GAE	Gas Assisted Etching
GIS	Gas Inject System
IBID	Ion Beam Induced Deposition
IC	Integrated Circuit
LMIS	Liquid Metal Ion Source
LNCT	Liquid Nitrogen Cold Trap
MD	Molecular Dynamics
PDD	Point Defect Density
RBS	Rutherford backscattering spectroscopy
ROI	Region of Interest
RT	Room temperature
SEM	Scanning Electron Microscope
TEM	Transmission Electron Microscopy
TRIDYN	Transport of Ions including Dynamics
TRIM	Transport of ions in matter

List of Symbols

(k)/(M)eV	(kilo)/(mega) electron volt
(k)V	(kilo)volt
°	Degree
∂	Partial derivative
$\int$	Integration
°C	Degree Celsius
µm	micrometer
$d(z)$	number of collision events per unit volume and unit ion dose at substrate depth z
E_d	Displacement threshold energy
K	Kelvin
mbar	minibar
min	minute
N	atomic density
nA	nanoampere
nC	nanocoulomb
N_d	Ion dose
nJ	nanojoule
nm	nanometer
pA	picoampere
pC	picocoulomb
D_{pd}	Point Defect Density
R	Milling rate

List of Figures

2.1 Basic schematic of a Focused Ion Beam microscope

2.2 Basic schematic of a double beam (electron and ion) microscope

2.3 A Dualbeam microscope manufactured by Thermo Fisher Scientific

2.4 SEM image of two perpendicular cross-sections of an Integrated Circuit done with FIB

2.5 Illustration of TEM lamella preparation with in-situ lift-out technique

2.6 Damage removal and recreation by high and low ion-energy milling in the final thinning process

2.7 A FIB-repaired IC manufactured using semiconductor process of 0.18 µm line width and 5 metal layers

2.8 Principles of 3D FIB applications

3.1 FIB induced amorphization of crystalline silicon at the surface

3.2 Two Gaussian beam profiles with higher level of overlapping and lower level of overlapping

3.3 Top view and side view of the silicon specimen milled by gallium FIB with a 5° glancing angle

3.4 A trench is form by gallium FIB milling on the silicon specimen

3.5 Gallium FIB milling rates on silicon

3.6 A rectangular slice was extracted from a crystalline silicon specimen and the mounted on a half-moon TEM grid

3.7 Ion image from top and electron image from side of two “H-bar” lamellae fabricated by gallium FIB milling on the substrate

3.8 Side view and top view image of the lamella being thinned down, one edge was cut free from the substrate

3.9 The volume where the H-bar lamella locates is depicted in blue on the substrate

3.10 Additional FIB milling is applied on the free edge facet of the lamella to create an amorphous region

3.11 TEM images of the free edge facet of the lamellae after 30/5/2/1/0.5 kV gallium FIB milling at 5° glancing angle to the facet

3.12 Normalized intensity and its derivative, data from the TEM image of the lamella milled by 30 kV gallium FIB

3.13 Normalized intensity and its derivative, data from the TEM image of the lamella milled by 5 kV gallium FIB

3.14 Normalized intensity and its derivative, data from the TEM image of the lamella milled by 2 kV gallium FIB

3.15 Normalized intensity and its derivative, data from the TEM image of the lamella milled by 1 kV gallium FIB

3.16 Normalized intensity and its derivative, data from the TEM image of the lamella milled by 0.5 kV gallium FIB

3.17 SEM image and optical image of a typical microtip coupon for APT analysis

3.18 A lamella is extracted from the silicon substrate, similar to TEM lamella preparation

3.19 The lamella is placed above a microtip and cut at the free end after mounted with deposited platinum

3.20 SEM images of a single specimen after being cut from the lamella and fixed on top of the microtip

3.21 Stage is tilted by 52° for normal incidence from the ion beam

3.22 A ring shape milling pattern is applied on the specimen

3.23 Another ring shape milling pattern is applied on the specimen, with small inner diameter and lower acceleration voltage

3.24 A secondary pillar might be formed if the ring patterns are not aligned, or the outer diameter does not cover the whole specimen

3.25 SEM image of a APT-ready specimen with a cone geometry tip

3.26 SEM images of the seven microtip eligible for further APT experiment

3.27 SEM images of post-experiment tips are superposed on the pre-experiment SEM images

3.28 A snapshot of the reconstructed tomography of one specimen

3.29 A cylindrical sampling volume with 10 nm diameter was placed perpendicular to the surface at the cross-section plane of the cone

3.30 Gallium atomic concentration along silicon substrate depth from 3 specimens

4.1 Removal of FIB produced amorphous surface layers on specimen by an argon ion polishing system (PIPS II)

4.2 A system scheme of the Beam Induced Polishing System (BIPS)

4.3 Argon pressure from the supply line is reduced by a pressure regulator from 10 bars to 1-2 bars

4.4 A scheme of the valve system of BIPS

4.5 Liquid nitrogen cold trap (LNCT) with a Dewar flask and a spiral pipeline going in and out of the flask

4.6 Illustration of the argon purification in the LNCT

4.7 A simplified sketch of the Gas Injection System (GIS) port of the BIPS system

4.8 Schematic of the cross-section of the nozzle

4.9 Top-view SEM image of the letterbox opening at the nozzle

4.10 A possible sample orientation for the BIPS process

4.11 Photos of the BIPS hardware configuration

4.12 SEM image of a typical “BIPS spot” with a dark center (bare specimen surface) and a bright halo (oxidation)

4.13 Vertical distance between the nozzle and the specimen surface

4.14 Operation workflow of the BIPS procedure

4.15 BIPS spots on SiOx1 with varies stage bias from 300 V to 75 V

4.16 BIPS spots on SiPt with varies stage bias from 300 V to 75 V

4.17 BIPS spots on SiOx2 with varies stage bias from 300 V to 75 V

5.1 Molecular Dynamics simulation considers all atoms in its computation volume at one calculation step, whereas BCA simulation only considers the two collision particles for a single calculation

5.2 A Frenkel pair is formed when an atom dislocates from its lattice position, creating an interstitial and a vacancy

5.3 Cerva and Hobler analytically derived the Frenkel Pair density and compared it to experimentally taken TEM images to find the critical Point Defect Density at the c-a interface

5.4 TRIDYN simulated PDD distribution along the depth of a gallium-ion-milled silicon substrate with several ion energies

5.5 TRIM simulated PDD distribution along the depth of a gallium-ion-milled silicon substrate with several ion energies

5.6 TRIDYN simulated gallium concentration along the depth of gallium-ion-milled silicon substrate with several ion energies

5.7 TRIM simulated gallium concentration along the depth of gallium-ion-milled silicon substrate with several ion energies

5.8 Milling rate of gallium ions on silicon substrate in progression of the ion dose in the TRIDYN simulation with several ion energies in 5˚ glancing angle

5.9 Milling rate of several ion energy are plotted and suggests a near logistic distribution, which implies a potential physical limit

6.1 Experimental gallium FIB milling rate and the TRIDYN calculated prediction as a function of the ion energy

6.2 Peak gallium concentration based on APT experiments for three specimens, and the corresponding TRIDYN and TRIM simulation results

6.3 Experimentally determined and TRIDYN/TRIM predicted FIB-induced amorphous layer thicknesses of silicon as a function of ion energy for identical beam conditions

List of Tables

3.1 Ion beam current used for milling experiments corresponding to the respective ion energy

3.2 FIB parameters for eight locations milled on the specimen

3.3 Step heights measured from trenches prepared by FIB milling

3.4 Amorphous layer thickness of the five FIB-milled lamellae for several ion energies

4.1 Standard parameters of BIPS procedure

5.1 C-a interface position predicted by TRIDYN and TRIM simulations for several ion energies, determined by the depth of the critical Point Defect Density

5.2 Mean milling rate R and its standard deviation with corresponding ion energy in mentioned TRIDYN simulations

6.1 Peak concentration of gallium in the silicon substrate predicted by TRIDYN and TRIM for identical FIB conditions

Chapter 1

Motivation

Over the last three decades, Focused Ion Beam (FIB) technology has been largely developed. Its potential has been expanded from Integrated Circuit modification and cross-section imaging in semiconductor industry to becoming an indispensable target sample preparation tool in electron microscopy for further analysis such as Transmission Electron Microscopy or Atom Probe Tomography. By focusing and aiming an accelerated ion beam to an arbitrary defined region on the specimen, FIB is able to modify the surface topography as a result of material sputtering. With the help of additional signal detectors or gas-inducing devices, FIB can also perform tasks like imaging or material deposition.

Traditionally, a FIB sample preparation recipe has been made based on experience. Hours or days of operation time have been spent before finding an optimized recipe for a specific application, which is limited by several aspects of the FIB sample preparation. For example, the accelerated ion beam introduces damage to the original sample material, dictated by the ion and specimen species, the beam conditions, the strategy of the milling procedure etc. A typical trade-off is to obtain mitigated damage with a low-energy ion beam, i.e. longer preparation time due to a low milling/sputter rate. Such an empirical method has been put into practice and worked well, because the application requirements have been extreme and ultimate optimization have not been needed to be reached.

Nowadays, high-resolution and low-energy applications with a vast variety of materials have posted new challenges for the FIB technique. The nature of mutually exclusion between high-resolution and low-energy has determined a more time-consuming and delicate task for the FIB operation. Considering also the emergence of several new materials integrated and new types of ion species used, empirical FIB

methods are no longer able to cope with such situation. More systematic approaches are needed in order to find optimized FIB solutions for different applications. On the other hand, an analytical tool with stand-alone FIB technology is not able to satisfy the growing needs from the applications. Scanning Electron Microscopes have been extended with FIB in dual-beam systems to expand its functionality. Extra components and add-ons have been designed and attached to such systems to make them complex analytical instruments.

Taking the case of sample preparation of silicon nanowires for Transmission Electron Microscopy (TEM) analysis, as an example, the need of low-damage optimized sample preparation procedures will be motivated. Silicon nanowires are one of the most promising candidates to substitute CMOS devices and to become the foundation of beyond-CMOS devices. TEM studies are desired to understand crystal orientation at Schottky junctions and to measure strain locally. Due to the extreme small size of its diameter (10-20 nm), a lamella with similar thickness is required. Using FIB, the task is achievable with a high ion-energy operation applying a 30 keV gallium ion beam, however, the induced damage layer will be even thicker than the lamella itself, destroying the atomic (crystalline) structure of the silicon nanowire completely. Consequently, lower energy operation is needed, however, it is practically impossible to establish an optimized recipe empirically, as the parameters to be considered are too many to comprehend. For an optimized recipe, the time to spend for each low-energy operation and the risk of destroying the lamella due to the poor resolution in low-energy operations have to be considered and studied in a systematic way.

In this thesis, the frontier of Focused Ion Beam technology is explored and pushed forward, by investigating the FIB-induced sample damage in a systematic way as well as

developing an advanced in-situ sample preparation technique, eventually to achieve a reduced-damage optimized FIB sample preparation procedure and respective recipes. There are several aspects to be addressed in this thesis:

- What is the milling rate of FIB on specimen?
- How much amorphization is induced by FIB preparation?
- How much ions are implanted in the specimen by FIB preparation?
- How to completely remove the damage in-situ?

The answers of these questions are going to build the foundation of the methodology to optimized FIB recipes.

Within this thesis, chapter 1 introduces the motivation of this doctoral thesis and formulates the structure. Chapter 2 reviews the Focused Ion Beam technology and its major applications. FIB-induced damage of the specimen is described in Chapter 3. Several experimental approaches are used to assess the damages induced from the FIB sample preparation. Chapter 4 describes a novel hardware system designated to work with a double beam system with the purpose to achieve an advanced FIB application for even higher quality sample preparation. In Chapter 5, a physics model suitable to describe the FIB milling process is adopted. This improved model, TRIDYN, is derived from a classical ion-solid interaction model, and its prediction results of specimen damage under specific FIB conditions are compared to the prediction from the conventional TRIM model. The last chapter is a combination of the discussion from the presented results and the conclusion of the thesis. Experimental data and simulation predictions are put together for comparison to demonstrate that reduced-damage FIB sample preparation can be achieve systematically and that optimized recipes can be established based on these

systematic studies. At the end of the thesis, visions of future advanced FIB sample preparation are drawn and developed.

Chapter 2

Introduction to Focused Ion Beam

Focused Ion Beam (FIB) technology has been brought to the electron microscopy community for more than three decades [1-10]. In its early development, FIB technique was primarily used in semiconductor industry for physical failure analysis and integrated circuit (IC) modification thanks to its site-specific modification capability [11, 12]. Nowadays, it is also used as a target-specific sample preparation technique for further analytical studies, such as Transmission Electron Microscopy (TEM) [13-17] or Atom Probe Tomography (APT) [16, 18-21]. In addition, its imaging capability is widely used, since information acquired from the secondary ion provides strong material contrast. With the development of double beam tools equipped with both electron beam column and ion beam column, Energy-Dispersive X-ray Spectroscopy (EDS) and Electron Backscatter Diffraction (EBSD) analysis [22-26] deliver information about chemical composition and crystal orientation. In addition, A triple beam system [27], nano-indentation [28] or electrical testing with nano-probes [29] have been shown to improve the power of the FIB technology.

In this chapter, the working principles of the Focused Ion Beam technology will be briefly described, followed by several typical applications.

2.1 Principles of Focused Ion Beam

A Focused Ion Beam microscope targets a focused and accelerated ion beam onto the specimen, which resembles a similar process as an Scanning Electron Microscope (SEM). Ions generated from an ion source are focused into a deflected beam by the ion optics before entering the vacuum chamber where the target specimen locates.

The most commonly adopted ion species is gallium generated from a Liquid Metal Ion Source (LMIS) [30, 31]. The LMIS is installed at the top of the ion column. By being heated up, liquid gallium wets a tungsten tip, forming an atomically sharp Taylor cone [32] with a typical radius of about 2 nm. The Taylor cone is the common result of the opposite force caused by surface tension and the applied field on the tungsten tip. Ionization and field emission of gallium happen at the apex of the tip because of the strong electric field. Emitted ions are accelerated to desired energy and condensed by electromagnetic lenses, forming a focused ion beam. The ion beam is deflected further by the Electro-magnetic lenses according to the scanning pattern set by the operator and targeted onto the specimen surface.

In principle, the beam size, i.e., the diameter of the focused beam, and the interaction volume of the beam with the specimen determine the resolution limits of the FIB microscope. Nowadays, state-of-art FIBs are able to achieve a resolution limit of 0.5 nm in the case of a helium ion microscope [33] and 4 nm in case of a gallium FIB [34].

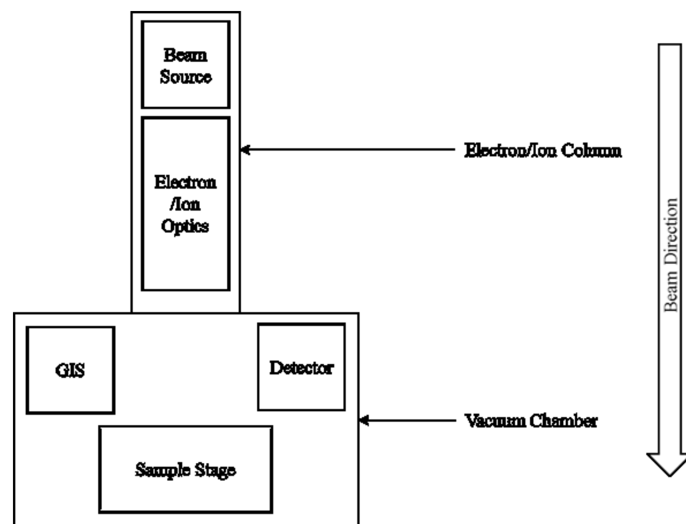

Fig. 2.1 Basic schematic of a Focused Ion Beam microscope.

The specimen material is sputtered away with a desire pattern by scanning the focused ion beam within a predefined area. The procedure can be repeated to create a deeper profile. This site-specific modification capability is the foundation of the most common FIB applications.

To fully exploit the advantages of FIB, modern FIB microscopes are usually equipped with an electron column as well. Such a double beams system uses the electron beam as the imaging tool and the ion beam as the micro/nano-fabrication tool. This configuration not only gives the operators the opportunity to perform real-time monitoring of the ion-beam process, new applications that utilize both beams to achieve high-resolution three-dimensional analysis have also been realized [35].

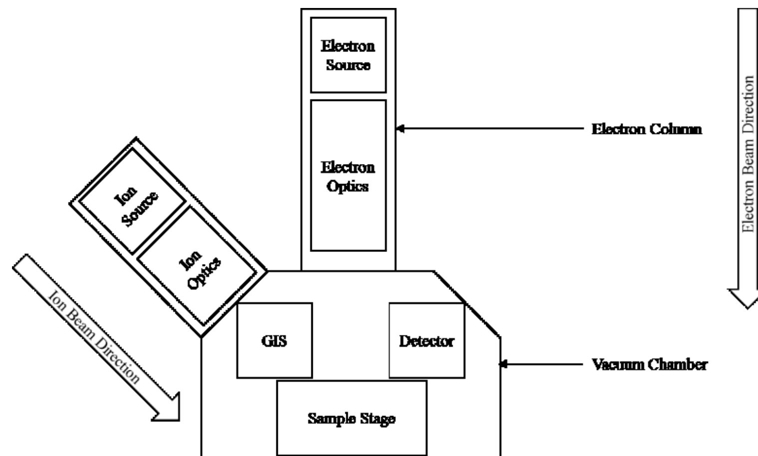

Fig. 2.2 Basic schematic of a double beam (electron and ion) microscope.

Modern FIB systems are often equipped with a gas injection system (GIS) [36]. The GIS provides the opportunity to either deposit material on the specimen surface or to enhance the sputter rate of the FIB process by injecting certain types of gases into the chamber. To deposit material, a process called ion beam induced deposition (IBID) is

performed [37-39]. Beam-sensitive gas is released and targeted onto the desired location of the specimen surface. The ion beam exposure breaks the chemical bonds in the gas molecules mainly with the generated secondary electrons, forming molecules to be deposited and volatile molecules to be pumped out of the chamber. On the other hand, for gas assisted etching (GAE) [39-41], a compound gas is injected from the GIS. These gas molecules are absorbed on the specimen substrate and ionized by the ion beam, forming volatile substance with the specimen element to enhance the removal rate.

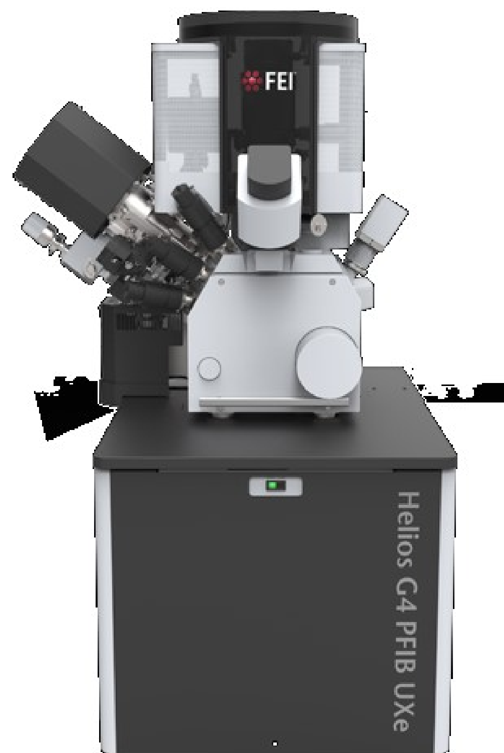

Fig 2.3 A Dualbeam microscope manufactured by Thermo Fisher Scientific [42].

2.2 Typical FIB Applications

The capability of site-specific ion-material interactions forms the foundation of FIB applications. These applications are based on specimen material sputtering or on deposition of materials like tungsten, platinum or carbon. Deposited materials are often shaped into a specially designed geometry using the beam scanning and blanking functions. In this way, the added material can play a role as sacrificial material or form an extra electrical path for extra functions.

2.2.1 Cross-section preparation

Scanning Electron Microscopy (SEM) is limited to its near-surface analysis capability. The primary electron beam usually has an interaction volume of several nanometers beneath the specimen surface. If the region of interest (ROI) is buried, material above must be removed before any analysis can be done. In many cases, hetero-layer information is of interest and a cross-section inspection is needed. In semiconductor industry, cross-sections are prepared for constructional analysis for further analysis of multi-layer stacks. Although it can be done mechanically, the cross-section preparation is preferred to be done with FIB as it provides a local target preparation approach and introduces much less damage to the adjacent area of the ROI. The preparation usually starts with depositing a protective/sacrificial layer of platinum directly on the specimen surface above the ROI. This is critical especially if the near-surface region must be preserved. The focused ion beam usually has a Gaussian beam profile. Such a beam profile results in material sputtering outside the pattern area due to the existence of a beam

tail. A protective layer on top ensures the material at the near-surface is intact while the ion beam is removing material towards the depth.

Fig. 2.4 SEM image of two perpendicular cross-sections of an Integrated Circuit done with FIB[43].

2.2.2 TEM lamella preparation

To perform a Transmission Electron Microscopy (TEM) analysis, specimen must be thin enough to become electron-transparent. Such electron-transparent specimens are often prepared with FIB, if the specimen is a bulk sample. There are several ways to prepare lamellae form the bulk.

Similar to preparing a cross-section with FIB, a protective layer is deposited on the sample surface above the ROI. A regular cross-section milling [34] is done by FIB on both sides of the protected area, forming a thin lamella between the two trenches. The lamella is lifted out from the bulk substrate and placed on a specially fabricated TEM grid. For in-situ lift-out, the lamella is cut free from the bulk by FIB and attached to a nano-manipulator by beam induced deposition. The lifted-out lamella is then transferred

to the TEM grid by the manipulator, attached onto the grid again by beam induced deposition material and cut away from the manipulator by FIB. The final thinning is then done on the TEM grid by FIB to achieve the desired thickness before the TEM analysis. For ex-situ lift-out, finally thinning is done before the lamella being lifted out from the substrate. Instead of being attached to a TEM grid, the lifted-out lamella is placed onto membrane structures and imaged in the TEM directly. Both in-situ and ex-situ lift-out are being practiced according to the requirements from the TEM analysis.

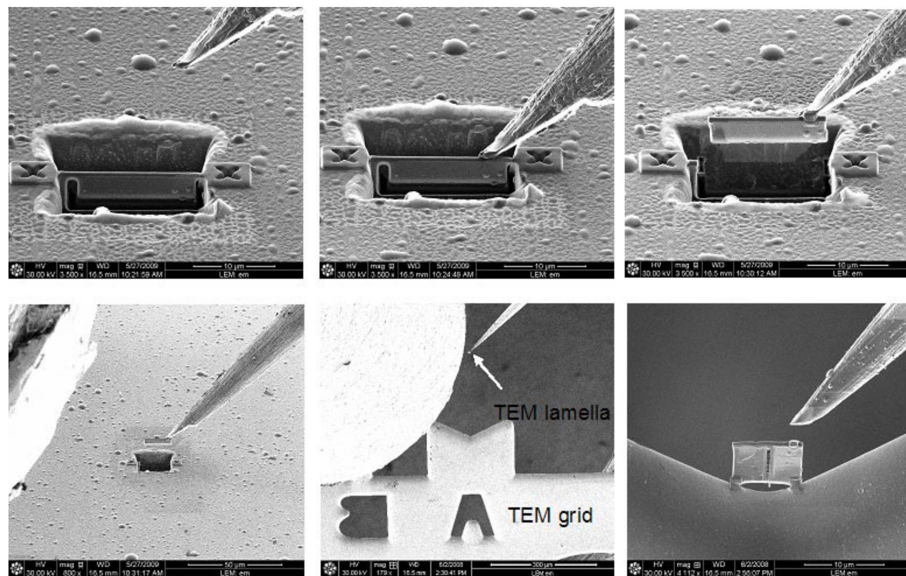

Fig. 2.5 Illustration of TEM lamella preparation with in-situ lift-out technique [44].

Whether in-situ or ex-situ lift-out is preferred, the final thinning of the lamella uses a multi-ion-energy strategy to mitigate the final sample damage. The damage layer formed during the high ion-energy milling is removed by the low ion-energy milling. The dose of low ion-energy millings should be large enough to remove the existing damage layer. In this way, the damage layer is removed and only the amorphous layer from the low ion energy FIB millings remains.

Figure 2.6 illustrates how the damage removal and recreation in the final thinning is achieved. Firstly, the FIB milling pattern of higher ion energy is placed at the location where material should be milled away. Secondly, while the material is removed, an undesired damaged region is formed outside of the FIB milling pattern. Thirdly, another FIB milling pattern of lower ion energy is placed at the remaining material, covering the damage layer previously created by the higher ion energy FIB milling. Lastly, the damage region is removed and another damage layer is created by the lower ion energy FIB milling, which should be the maximum acceptable damage in the application.

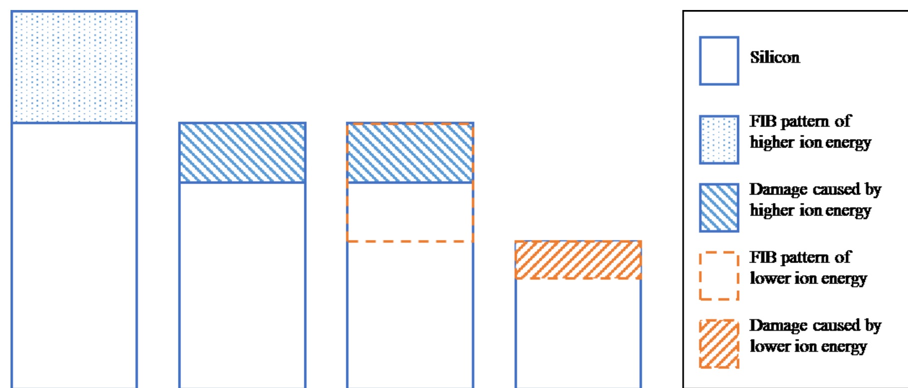

Fig. 2.6 (from left to right) Damage removal and recreation by high and low ion-energy milling in the final thinning process.

2.2.3 Circuit Modification

Benefited from the beam induced deposition capability, FIB also plays a role in integrated circuit (IC) modification. Rapid testing or modification of semiconductor integrated circuits can be done with FIB. To cut off a conductive metal connection of an IC, FIB is used to sputter away the connection metal. To connect two electrical points, conductive material like tungsten can be deposited onto the target region. More

importantly, FIB shows its value when the desired electrical points are beneath the IC surface. If some applications can be done with the help of nano electrical probers, where conductive probers are placed directly on top of the metal contacts of the IC, FIB is the only way to expose the buried contacts by removing the materials on top without damaging the remaining circuit integrity.

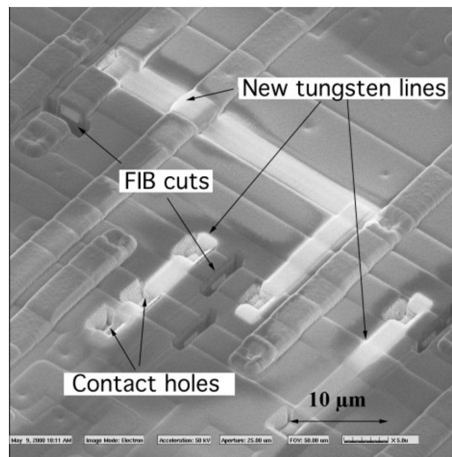

Fig. 2.7 A FIB repaired IC originally manufactured using semiconductor process of 0.18 µm line width and five metal layers. The cuts and the new tungsten conductor lines deposited in the repairing process are shown by arrows[45].

2.2.4 3D EDS and 3D EBSD analysis

Creating three-dimensional analytical data is an important FIB application for material science. Different from non-destructive methods like X-ray Tomography, 3D FIB analysis is a destructive approach. Such applications require incorporation of an electron beam. The electron beam is to generate two-dimensional information such as secondary electron image data and optionally with elemental or crystallographic data

from a cross-section of the specimen from Energy-dispersive X-ray Spectroscopy (EDS) or Electron Backscatter Diffraction (EBSD) maps from a cross-section of the specimen.

The ion beam and the electron beam are operated in an alternating fashion. After the 2D information is acquired, FIB is used to sputter away the material so that the previously hidden region is now exposed and can be analyzed to generate a new piece of 2D information. As a certain volume of material is consumed and analyzed, a full stack of 2D slices is acquired and stored. Each image has the x and y information of a certain plane where z is represented by the corresponding image number. For imaging, the spacing in x and y is limited only by the resolution of the SEM tool, while the z-resolution depends on the slice thickness cut with the FIB.

The stack of 2D images is then processed using special software for reconstruction and segmentation. These processes require the image acquisition, i.e. FIB/SEM process, to be stable and in good focus. Because usually hundreds of images are taken for reconstruction, and the whole acquisition time takes up to several hours, automation is adopted. With the help of image recognition of a certain preselected feature near the ROI, automatic beam shifting or re-focusing corrections can be done in the process.

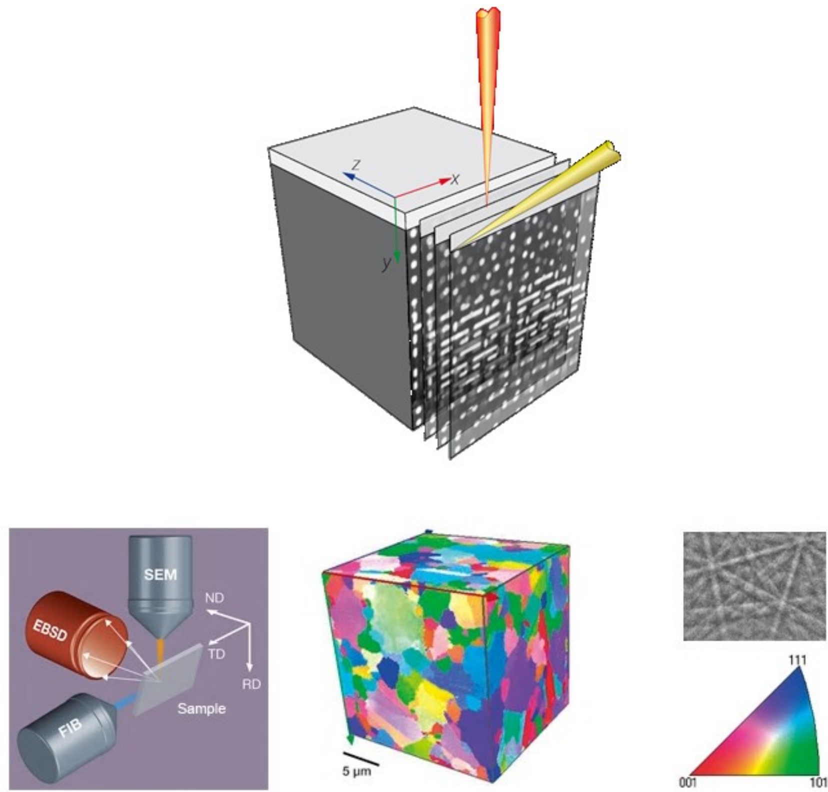

Fig. 2.8 Principles of 3D FIB applications[46, 47]. Electron beam and ion beam are operated alternatively to generate 3D data set.

References

1. Seliger, R., et al., *High‐resolution, ion‐beam processes for microstructure fabrication.* Journal of Vacuum Science and Technology, 1979. **16**(6): p. 1610-1612.

2. Seliger, R., et al., *A high‐intensity scanning ion probe with submicrometer spot size.* Applied Physics Letters, 1979. **34**(5): p. 310-312.

3. Orloff, J., *High‐resolution focused ion beams.* Review of Scientific Instruments, 1993. **64**(5): p. 1105-1130.

4. Matsui, S. and Y. Ochiai, *Focused ion beam applications to solid state devices.* Nanotechnology, 1996. **7**(3): p. 247.

5. Reyntjens, S. and R. Puers, *A review of focused ion beam applications in microsystem technology.* Journal of micromechanics and microengineering, 2001. **11**(4): p. 287.

6. Orloff, J., L. Swanson, and M. Utlaut, *High Resolution Focused Ion Beams: FIB and its Applications: Fib and Its Applications: The Physics of Liquid Metal Ion Sources and Ion Optics and Their Application to Focused Ion Beam Technology*. 2003: Springer Science & Business Media.

7. Giannuzzi, L.A., *Introduction to focused ion beams: instrumentation, theory, techniques and practice*. 2006: Springer Science & Business Media.

8. Volkert, C.A. and A.M. Minor, *Focused ion beam microscopy and micromachining.* MRS bulletin, 2007. **32**(5): p. 389-399.

9. Yao, N., *Focused ion beam systems: basics and applications*. 2007: Cambridge University Press.

10. Melngailis, J., *Focused ion beam technology and applications.* Journal of Vacuum Science & Technology B: Microelectronics Processing and Phenomena, 1987. **5**(2): p. 469-495.

11. Harriott, L., A. Wagner, and F. Fritz, *Integrated circuit repair using focused ion beam milling.* Journal of Vacuum Science & Technology B: Microelectronics Processing and Phenomena, 1986. **4**(1): p. 181-184.

12. Ward, B., et al. *Microcircuit modification using focused ion beams*. in *Electron-Beam, X-Ray, and Ion Beam Technology: Submicrometer Lithographies VII*. 1988. International Society for Optics and Photonics.

13. Giannuzzi, L.A. and F.A. Stevie, *A review of focused ion beam milling techniques for TEM specimen preparation.* Micron, 1999. **30**(3): p. 197-204.

14. Li, J., T. Malis, and S. Dionne, *Recent advances in FIB–TEM specimen preparation techniques.* Materials characterization, 2006. **57**(1): p. 64-70.

15. Kamino, T., et al., *A FIB micro-sampling technique and a site specific TEM specimen preparation method.* Introduction to Focused Ion Beams, 2005: p. 229-245.

16. Lozano-Perez, S., *A guide on FIB preparation of samples containing stress corrosion crack tips for TEM and atom-probe analysis.* Micron, 2008. **39**(3): p. 320-328.

17. Overwijk, M., F. Van den Heuvel, and C. Bulle-Lieuwma, *Novel scheme for the preparation of transmission electron microscopy specimens with a focused ion beam.* Journal of Vacuum Science & Technology B: Microelectronics and Nanometer Structures Processing, Measurement, and Phenomena, 1993. **11**(6): p. 2021-2024.

18. Miller, M.K., et al., *Review of atom probe FIB-based specimen preparation methods.* Microscopy and Microanalysis, 2007. **13**(6): p. 428-436.

19. Miller, M., K. Russell, and G. Thompson, *Strategies for fabricating atom probe specimens with a dual beam FIB.* Ultramicroscopy, 2005. **102**(4): p. 287-298.

20. Saxey, D., et al., *Atom probe specimen fabrication methods using a dual FIB/SEM.* Ultramicroscopy, 2007. **107**(9): p. 756-760.

21. Thompson, K., et al., *In situ site-specific specimen preparation for atom probe tomography.* Ultramicroscopy, 2007. **107**(2): p. 131-139.

22. Groeber, M., et al., *3D reconstruction and characterization of polycrystalline microstructures using a FIB–SEM system.* Materials Characterization, 2006. **57**(4): p. 259-273.

23. Michael, J. and L. Giannuzzi, *Improved EBSD sample preparation via low energy Ga+ FIB ion milling.* Microscopy and Microanalysis, 2007. **13**(S02): p. 926.

24. Lasagni, F., et al., *Nano-characterization of Cast Structures by FIB-Tomography.* Advanced Engineering Materials, 2008. **10**(1-2): p. 62-66.

25. West, G. and R. Thomson, *Combined EBSD/EDS tomography in a dual-beam FIB/FEG–SEM.* Journal of microscopy, 2009. **233**(3): p. 442-450.

26. Lasagni, F., et al. *3D nano-characterisation of materials by FIB-SEI/EDS tomography*. in *IOP Conference Series: Materials Science and Engineering*. 2010. IOP Publishing.

27. Hitachi High-Technologies Corporation. *Focused Ion and Electron Beam System & Triple Beam System NX2000*. 2018; Available from: https://www.hitachi-hightech.com/global/product_detail/?pn=em-nx2000.

28. Volkenandt, T., et al. *Automatic FIB-SEM Preparation of Straight Pillars for In-Situ Nanoindentation*. in *European Microscopy Congress 2016: Proceedings*. 2016. Wiley Online Library.

29. Löffler, M., et al., *In-Situ Investigations of Individual Nanowires within a FIB/SEM System.* Microscopy and Microanalysis, 2014. **20**(S3): p. 360-361.

30. Swanson, L., *Liquid metal ion sources: Mechanism and applications.* Nuclear Instruments and Methods in Physics Research, 1983. **218**(1-3): p. 347-353.

31. Clampitt, R., *Advances in molten metal field ion sources.* Nuclear Instruments and Methods in Physics Research, 1981. **189**(1): p. 111-116.

32. Taylor, G. *Disintegration of water drops in an electric field*. in *Proceedings of the Royal Society of London A: Mathematical, Physical and Engineering Sciences*. 1964. The Royal Society.

33. Carl Zeiss Microscopy GmbH *ORION NanoFab Product Information*. 2016.

34. FEI Company *Helios NanoLab 660 DualBeam System User's Guide*. 2014.

35. Wirth, R., *Focused Ion Beam (FIB) combined with SEM and TEM: Advanced analytical tools for studies of chemical composition, microstructure and crystal structure in geomaterials on a nanometre scale.* Chemical Geology, 2009. **261**(3): p. 217-229.

36. Rasmussen, J., *Gas injection system*. 1995, Google Patents.

37. Tao, T., et al., *Focused ion beam induced deposition of platinum.* Journal of Vacuum Science & Technology B: Microelectronics Processing and Phenomena, 1990. **8**(6): p. 1826-1829.

38. Tao, T., W. Wilkinson, and J. Melngailis, *Focused ion beam induced deposition of platinum for repair processes.* Journal of Vacuum Science & Technology B: Microelectronics and Nanometer Structures Processing, Measurement, and Phenomena, 1991. **9**(1): p. 162-164.

39. Utke, I., P. Hoffmann, and J. Melngailis, *Gas-assisted focused electron beam and ion beam processing and fabrication.* Journal of Vacuum Science & Technology B:

Microelectronics and Nanometer Structures Processing, Measurement, and Phenomena, 2008. **26**(4): p. 1197-1276.

40. Casey, J.D., et al., *Gas-assisted etching with focused ion beam technology.* Microelectronic Engineering, 1994. **24**(1-4): p. 43-50.

41. Young, R., J. Cleaver, and H. Ahmed, *Characteristics of gas-assisted focused ion beam etching.* Journal of Vacuum Science & Technology B: Microelectronics and Nanometer Structures Processing, Measurement, and Phenomena, 1993. **11**(2): p. 234-241.

42. Thermo Fisher Scientific. *Helios G4 PFIB UXe DualBeam for Materials Science*. 2018; Available from: https://www.fei.com/products/dualbeam/helios-g4-pfib-uxe-for-materials-science/.

43. GreyB Services. *Reverse Engineering Tools*. 2017; Available from: https://www.greyb.com/our-services/infringement-solutions/ip-reverse-engineering-tools/.

44. Müller, E. *Focused-Ion-Beam (FIB) Mikroskopie und Nanostrukturierung*. 2018; Available from: https://www.lem.kit.edu/192.php.

45. EMPART. *Infotech Oulu Annual Report 2000*. 2000; Available from: http://www.infotech.oulu.fi/Annual/2000/EMPART.html.

46. Brackx, E., et al., *Recent analytical developments for powder characterization.* The European Physical Journal Special Topics, 2015. **224**(9): p. 1787-1804.

47. Hitachi High Technologies America. *FIB-SEM System for True 3D Structural Analysis*. 2018; Available from: https://www.hitachi-hightech.com/us/product_detail/?pn=em-nx9000.

Chapter 3

Gallium Focused Ion Beam on Silicon

Focused Ion Beam is an essential method to prepare Transmission Electron Microscopy (TEM) specimens [1, 2], especially for target preparation needed in e.g. semiconductor industry [3, 4]. There are several ways how FIB is applied in the TEM sample preparation process. For example, FIB can be used from the beginning of the process: by forming two back-to-back trenches, a thin lamella can be extracted from the bulk substrate using the so-called lift-out technique [5, 6]. Often in the in-situ lift-out approach, this lamella is further thinned down until the desired thickness after being attached to a TEM grid. In the ex-situ cases, further thinning is performed before the lamella being transferred ex-situ to a TEM grid. Alternatively, the specimen can be first mechanically thinned down to about 1 μm. Followed by a secondary FIB process, desired thickness of the specimen can be achieved. FIB is widely used to perform cross-section inspection of specimen. A trench with one vertical sidewall is cut out by FIB directly on the substrate over the region of interest. A secondary fine milling (usually with lower ion energy) is then applied to this sidewall to view the interested cross-section.

On the other hand, there are also many other FIB applications such as 2D/3D nanoscale characterization of materials [7, 8], or direct prototyping of complex nanoscale structures [9, 10]. No matter how the focused ion beam is applied in these applications, most of them involve material removal/sputtering. While the material from the unwanted region is removed by FIB, the adjacent region is unavoidably damaged [11-13]. These damages appear in many forms according to what is actually concerned in the study. The primary focused ion beam causes undesired ion implantation in the specimen. Although the concentration is as low as a few percent, induced ions can indeed change the intrinsic

properties of the specimen such as conductivity. For crystalline materials, amorphization is commonly observed in the near surface region.

In semiconductor industry, sample preparation becomes increasingly challenging for TEM analysis of advanced microelectronic devices. Due to the ongoing shrinking of the feature size for advanced technology nodes and with the movement to 3D devices (e.g. FinFETs), thinner lamellae without an amorphous layer as well as much less ion implantation are required. For gallium FIB, which is the most commercial available FIB microscope, depending on the beam conditions, the thickness of an amorphous layer induced by FIB on silicon varies between 20 nm and 30 nm for a 30-kV gallium ion beam with small glancing angles applied [14]. The implanted gallium concentration is usually around 10% [14].

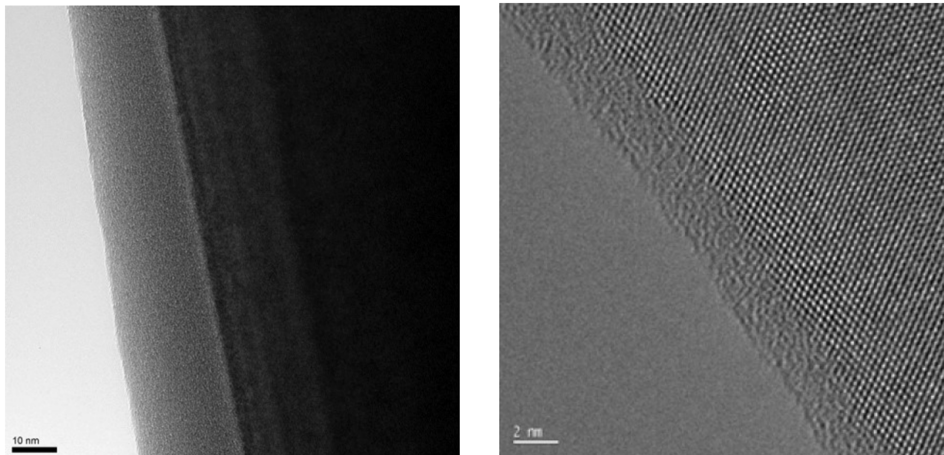

Fig. 3.1 FIB induced amorphization of crystalline silicon at the surface. HRTEM images of amorphization damage in silicon due to 5 kV gallium FIB milling: (left) on a cone structure and (right [15]) on a side wall.

In this chapter, three studies using the FEI Helios 660 DualBeam [16] tool were carried out. Firstly, experiments were done to investigate the gallium FIB milling rate on

silicon specimens. To measure the amorphization layer thickness, a TEM study was carried out. Finally, to determine the local implanted gallium concentration induced by FIB, Atom Probe Tomography was done.

3.1 SEM study of gallium FIB milling rate of silicon

One of the key parameters to engineer an optimized FIB sample preparation recipe is the FIB milling rate on the specimen [17-19]. The FIB milling rate is defined as the difference between the material removal rate and the material redeposition rate during the sputtering. A high milling rate with high energy ion shortens the total recipe time, however, it also introduces a high level of damage to the specimen.

Several aspects were considered in the design of the experiment to determine the FIB milling rate. Firstly, the milling location should be at a relatively open space in order to avoid undesired redeposition from the surrounding of the site. If the specimen is uneven (structural topography), the extended beam tail of the Gaussian distribution ion beam profile might mill material from the surrounding and sputtered material might be redeposited onto the defined milled region, instead of going into the vacuum. Secondly, homogeneous dose density should be considered. In FIB milling, individual beam spots are assigned to fill the whole milled region. The ion beam remains at each spot for a period a time and moves to the next subsequently, while being blanked in between. Since the ion beam profile has a Gaussian distribution, an overlap of two beam spots is usually introduced to compensate the non-uniformity of the dose distribution. The overlap area must be large enough (>50%) to obtain a uniform dose density in the milled region. Then, the average milling rate can be determined by normalizing the resulting depth with the unit dose.

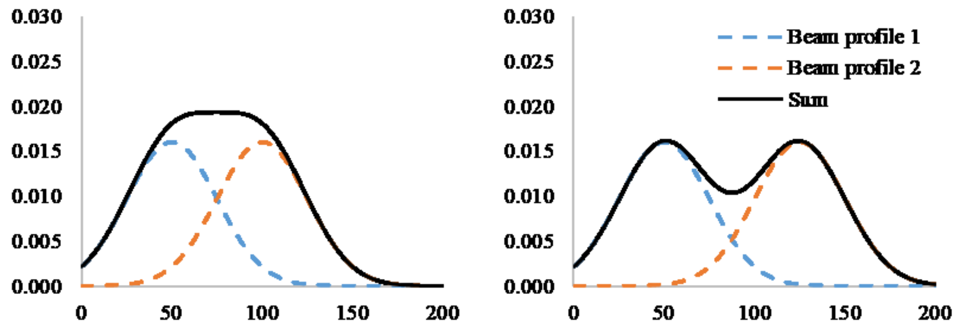

Fig. 3.2 Two Gaussian beam profile with higher level of overlapping (left) and lower level of overlapping (right). A more uniform overall dose density is seen with higher overlapping.

These experiments were carried out to measure the FIB milling rate at a small glancing angle. FIB milling with normal incidence is usually used in the beginning of the recipe, e.g. for TEM lamella preparation.

3.1.1 SEM experiment procedure

The ion beam alignment was performed for one single aperture to have the same instrument conditions for all experiments. The aperture acts as beam current selector and remained unchanged for experiments with several ion energies. For a single aperture, the resulting beam current is different according to the ion energy due to different ion source conditions. The actual beam current regarding to the selected ion energies are shown in Table 3.1.

Ion energy	30kV	16kV	8kV	5kV	2kV	1kV	0.5kV
Beam current	0.79 nA	0.43 nA	0.21 nA	0.12 nA	72 pA	0.14 nA	0.36 nA

Tab. 3.1 Ion beam current used for milling experiments corresponding to the respective ion energy.

A flat crystalline silicon substrate was used as the specimen in this study. The defined milled region was located at the edge of the specimen, giving the advantage of easy observation of the cross-section of the milled trench to measure the height between the original specimen surface and the bottom of the milled trench.

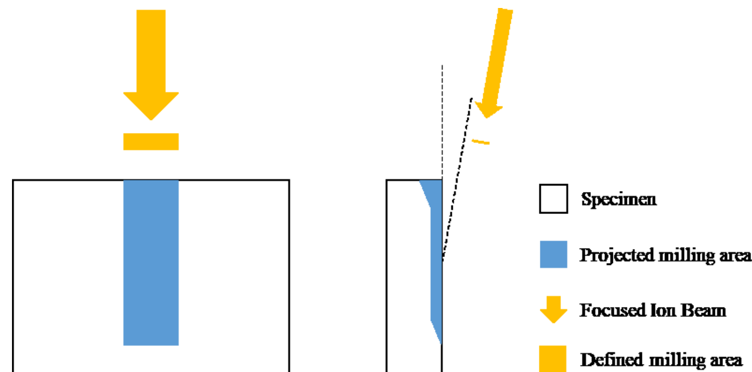

Fig. 3.3 Top view (left) and side view (right) of the silicon specimen milled by gallium FIB with a 5° glancing angle.

The specimen was horizontally mounted on the sample holder and the stage was tilted so that the specimen surface had a 5° angle with respect to the ion beam direction. The FIB milling pattern was a rectangle pattern. Because of the incident angle, the projected area was about 11 times larger on the specimen. To avoid the inhomogeneous milling profile caused by the edge of the specimen and the trench, the trench bottom to be investigated later was chosen to be at the center. Eight locations were milled with different FIB conditions given in Table 3.2.

Ion energy	Beam current	Pattern size	Milling time	Ion dose @5000X	Overlap	Beam diameter
30 kV	790 pA	20x10 μm^2	15 min	3.44 nC/μm^2	50%	77 nm
16 kV	430 pA	15x10 μm^2	30 min	4.95 nC/μm^2	50%	119 nm

Ion energy	Beam current	Pattern size	Milling time	Ion dose @5000X	Overlap	Beam diameter
8 kV	210 pA	15x10 μm^2	60 min	4.31 $nC/\mu m^2$	50%	118 nm
5 kV	120 pA	15x10 μm^2	120 min	5.79 $nC/\mu m^2$	50%	159 nm
2 kV	72 pA	15x10 μm^2	240 min	6.25 $nC/\mu m^2$	50%	281 nm
1 kV	140 pA	15x10 μm^2	480 min	26.29 $nC/\mu m^2$	75%	751 nm
0.5 kV	360 pA	15x10 μm^2	960 min	109.94 $nC/\mu m^2$	75%	2700 nm
0.5 kV	360 pA	15x10 μm^2	960 min	107.28 $nC/\mu m^2$	75%	2700 nm

Tab. 3.2 FIB parameters for eight locations milled on the specimen.

These parameters were chosen to ensure that the trench was large and deep enough, so that the height between the original specimen surface and the trench bottom can be clearly distinguished in the SEM image. Note that due to the insufficient resolution of the ion beam with the energy of 0.5 kV, its experiment was repeated to demonstrate the repeatability of the measurement and to improve the statistical relevance of the results.

After the trench had been formed, a layer of ion beam induced deposition platinum was made on the trench, crossing both the original specimen surface and the trench bottom. A cross-section was prepared beneath this platinum layer. The sharp contrast between platinum and silicon makes it possible to measure the step height. Three cross-sections were prepared for each trench, and the respective three step heights were measured.

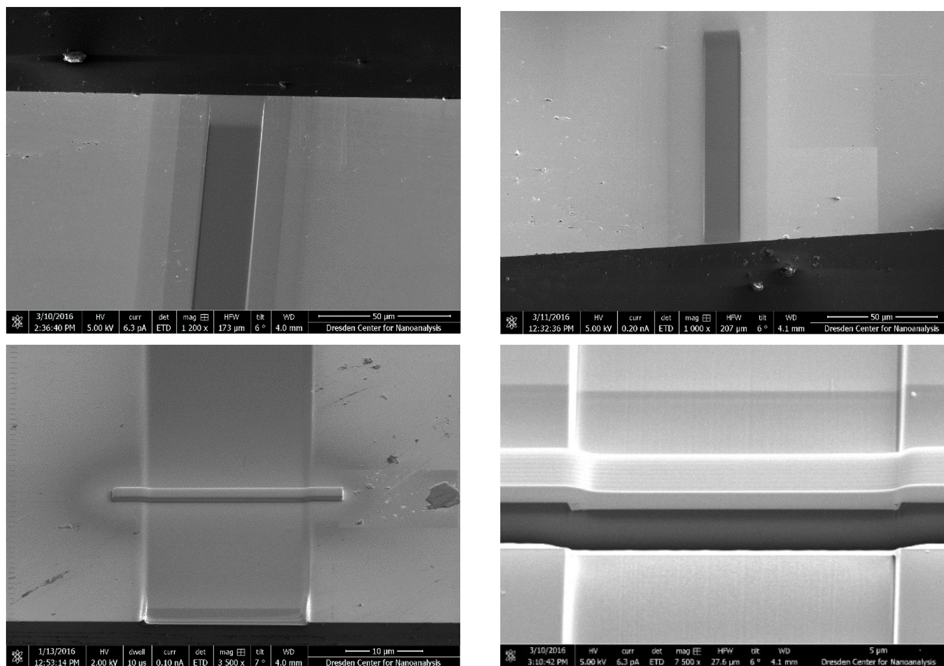

Fig. 3.4 (upper left and upper right) A trench is form by gallium FIB milling on the silicon specimen. (lower left) Platinum is deposited on the trench across both edges. (lower right) A cross-section is prepared to measure the step height between the original specimen surface and the trench bottom.

3.1.2 SEM experiment result

The twenty-four measured step heights are listed in Table 3.3. The relatively low deviation suggests that the trench was uniformly formed by a uniformly distributed ion dose. Even in the case of 0.5 kV ion energy, in which the beam diameter is almost up to 30% of the pattern width, the measured step heights deviation is still smaller than 7%. For such a large size beam, the ion dose density near the pattern edge can be much lower than in the center and the expended beam tail can sputter matter from outside of the trench into the milled trench.

Ion energy (kV)	30	16	8	5	2	1	0.5	0.5
Step height (nm)	559	612	350	367	192	437	262	245
	541	639	358	358	203	441	286	249
	561	628	335	363	196	419	242	251
Standard deviation (nm)	8.9	11.0	9.5	3.6	4.3	9.7	17.8	2.8

Tab. 3.3 Step heights measured from trenches prepared by FIB milling.

The FIB milling rate is calculated by normalizing the trench step height with the unit ion dose applied in the milling. A time-based milling rate has to be specified with the applied beam current. However, in practice different beam currents with the same ion energy are used in preference with different applications or even for different steps in a recipe. A dose-based milling rate can avoid this problem. In order to calculate the milling time for a specific milling step, one needs only to include the chosen beam current density in the calculation. Figure 3.5 shows the milling rates normalized with the respective applied ion doses.

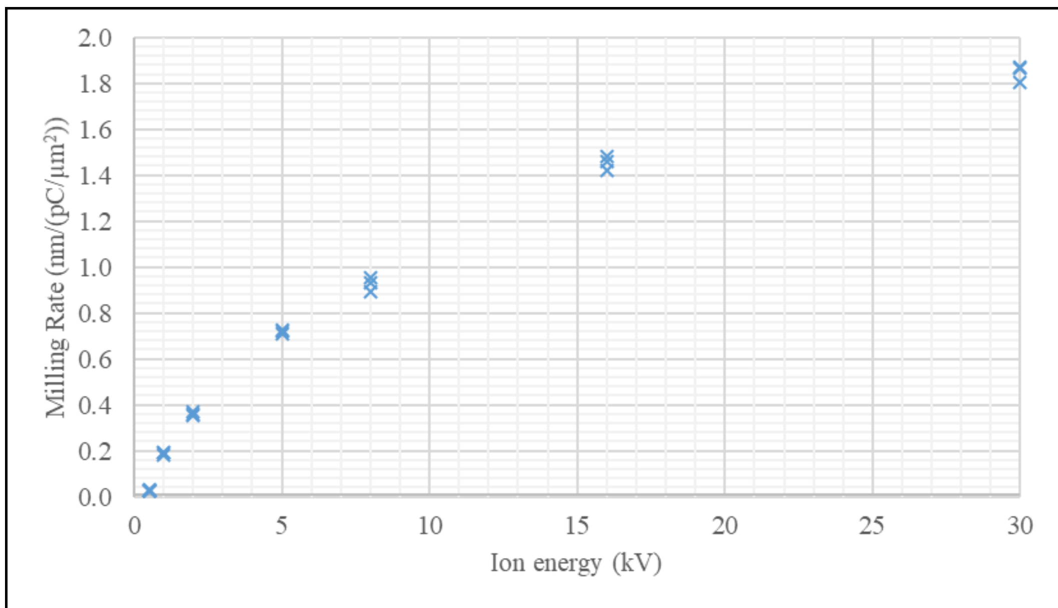

Fig. 3.5 Gallium FIB milling rates on silicon. Only small deviation is seen among the different measured values within the experiments of the same ion energy.

3.2 TEM study of gallium FIB induced silicon amorphization

It has been known that FIB sample preparation introduces amorphization to crystalline materials. Quantifying such amorphization is critical for optimizing a FIB recipe as it determines the end-point condition of the preparation. Amorphization occurs in the near-surface region of the milled region of the specimen. Therefore, cross-sections were prepared to measure the amorphous layer thickness in silicon after gallium FIB milling. Giannuzzi[13] and McCaffrey[20] used a direct FIB line milling pattern to form trenches and pits on a crystalline silicon specimen. A cross-session lift-out was performed from these trenches and pits to investigate the sidewall damage in the TEM. Rubanov[14] and Kato[21] did a cross-session lift-out from a low-angle ion-milled specimen of a near-surface region. The lift-out was investigated using TEM afterwards. These lift-out procedures are time consuming. In this study, a simpler experiment approach is designed, where the lift-out procedure for TEM analysis was omitted. Instead, a thin non-lift-out lamella was fabricated for the TEM-based measurement of the amorphous layer thickness.

3.2.1 Gallium FIB experiment procedures

A crystalline silicon specimen was sawed and mechanically grinded as a rectangular slice with the thickness down to approximately 100 μm. This slice was then mounted on a half-moon TEM grid, in a way that the original surface of the silicon substrate was

oriented upward. In the following text, this slice is referred as the substrate for the experiments. The procedure is illustrated in Figure 3.6.

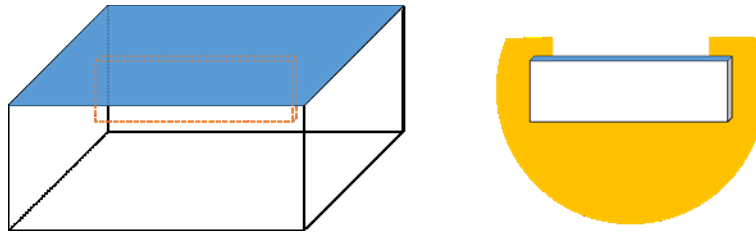

Fig. 3.6 A rectangular slice was extracted from a crystalline silicon specimen and then mounted on a half-moon TEM grid. The surface is colored in blue in the illustration.

Five lamellae were fabricated using gallium FIB milling. These lamellae were not undercut nor lifted out, i.e. each lamella was free on one side, whereas the other side and the bottom remained fixed to the substrate.

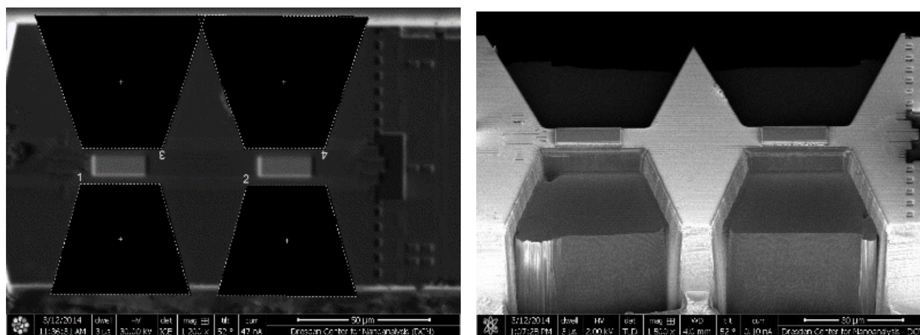

Fig. 3.7 Ion image from top (left) and electron image from side (right) of two "H-bar" lamellae fabricated by gallium FIB milling on the substrate.

First, a milling pattern of two back-to-back trapezoids was placed on the specimen surface to remove a major part of the material. The area between the two trapezoids was protected by deposited platinum to forms a lamella with a thickness of about 100 to 200 nm. This step is similar to fabricating the "H-bar" lamellae [13]. (Figure 3.7)

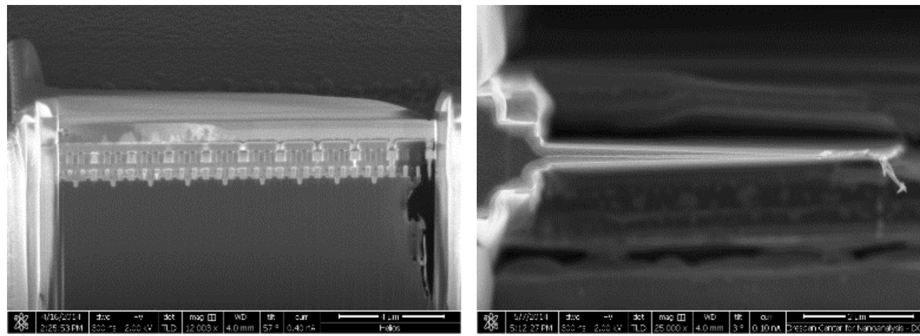

Fig. 3.8 Side view (left) and top view (right) image of the lamella being thinned down, one edge was cut free from the substrate.

Second, the lamella was thinned down by applying the ion beam on both sides of the lamella sidewalls symmetrically. As a crucial step, one edge of the lamella was cut free from its supporting substrate. As a result, the surface and one edge of the lamella were exposed, while the foundation and the other edge of the lamella were still attached and supported by the substrate. (Figure 3.8 and Figure 3.9)

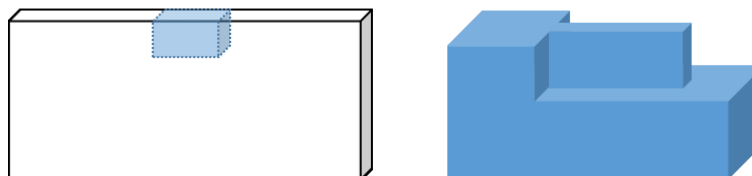

Fig. 3.9 The volume where the H-bar lamella locates is depicted in blue on the substrate. The thickness of the lamella was thinned down while one edge was cut free from its substrate.

In the last step, the lamella sidewalls were thinned by a 2-kV gallium FIB milling. FIB milling at the relatively low ion energy removes damaged material caused by the previous high ion energy milling. The damage that introduced up to this step is not the desired result to be investigated and should be removed by a relatively low ion energy milling.

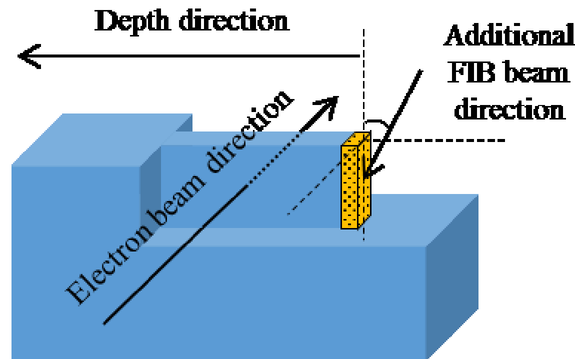

Fig. 3.10 Additional FIB milling is applied on the free edge facet of the lamella to create an amorphous region (colored in yellow). The TEM electron beam direction is perpendicular to the lamella so that the thickness of the amorphous layer thickness can be measured.

After fabrication of the special lamella geometry, the last step is to create an amorphous layer at the location where it can be examined using a TEM cross-section, i.e. the free edge. The stage was rotated by 90° and tilted by 47° to achieve a 5° angle between the free edge and the ion beam direction (the ion beam column is mounted 52° from stage normal). Consequently, when the additional ion beam starts to mill the edge facet, it creates an amorphous layer perpendicular to the original substrate surface. Then, the lamella can be viewed as a cross-section of an ion beam amorphized silicon substrate with the amorphous layer on the side. The width of the amorphous region is the depth or the thickness of the amorphous layer to be investigated. (Figure 3.10)

Five lamellae with identical geometry were fabricated on the substrate. Each of them was exposed and milled at the free edge by an additional ion beam with ion energies of 30, 5, 2, 1 and 0.5 kV, respectively, to create an amorphous layer. An ion energy of 30 kV was chosen as it is the parameter for standard FIB milling, while 5 kV and 2 kV

represent the low-voltage regime. To explore the state of the art FIB development, ultra-low-voltages of 1 kV and 0.5 kV were also included.

3.2.2 TEM images and data interpretation

The TEM images of the lamellae were taken by flipping the grid 90° till horizontal, aligning the specimen exactly along the (110)-pole axis and using a contrast aperture to enable a good distinction between crystalline and amorphous silicon on the lamella.

These images are shown in Figure 3.11 (a)-(e). In all images, three regions are distinguished by diffraction contract [22]. Different from mass contrast or thickness contrast, diffraction contract gives information depending on the atomic structure. Electrons are heavily scattered by material with a crystalline structure, and the corresponding region appears dark in the Bright Field image. The brightest region to the right represents vacuum and the darkest region to the left represents the crystalline silicon which was not amorphized by FIB milling. The grey region in between is amorphous silicon caused by FIB milling. There is a clear boundary between the vacuum and the amorphous silicon, whereas the boundary between crystalline and amorphous silicon appears to be jagged, which is more profound for high ion energies.

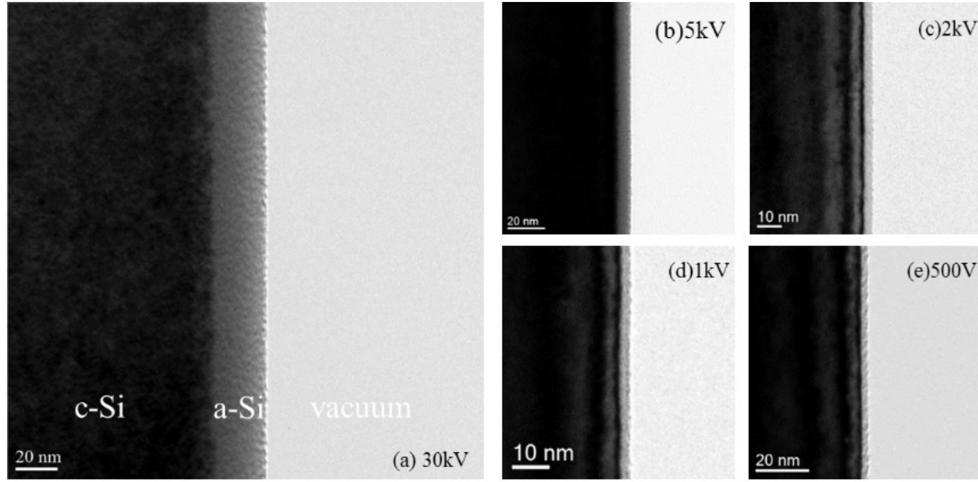

Fig. 3.11 TEM images of the free edge facet of the lamellae after 30/5/2/1/0.5 kV gallium FIB milling at 5° glancing angle to the facet.

In order to determine the amorphous layer thickness from each TEM image, a conventional approach for edge detection was used to determine the interface between the crystalline and amorphous silicon [23, 24]. Although it is fast and intuitive to measure the distance manually, a systematic method provides higher accuracy. Despite the arbitrary human error of placing the measurement markers, the jagged boarder line between the crystalline and amorphous silicon increases the uncertainty of the measurement.

Thanks to the symmetry, the 2D image was first integrated along the interface direction (vertical in the images), forming a 1D normalized intensity data set.

$$I_{1D}(x) = \int I_{2D}(x, y)\, dy \qquad \text{(Eq. 3.1)}$$

Secondly, the intensity changes along the substrate normal was found by deriving the first derivative from the normalized intensity. These changes are represented by positive maxima of the first derivative, if deriving from low intensity to high intensity.

The distance between the first two positive peaks of the derivative from the vacuum side is measured as the thickness of the corresponding amorphous layer thickness. These two peaks represent the interface between vacuum and amorphous silicon and the interface between amorphous silicon and crystalline silicon, respectively. Figures 3.12 to 3.16 show the intensity information from each TEM image, respectively.

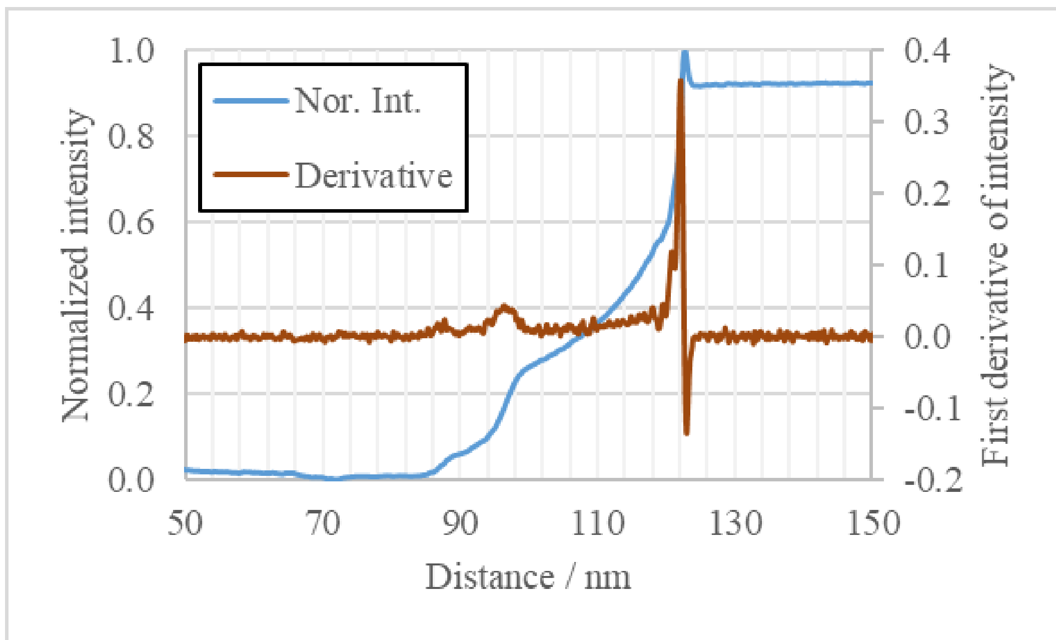

Fig. 3.12 Normalized intensity and its derivative, data from the TEM image of the lamella milled by 30 kV gallium FIB.

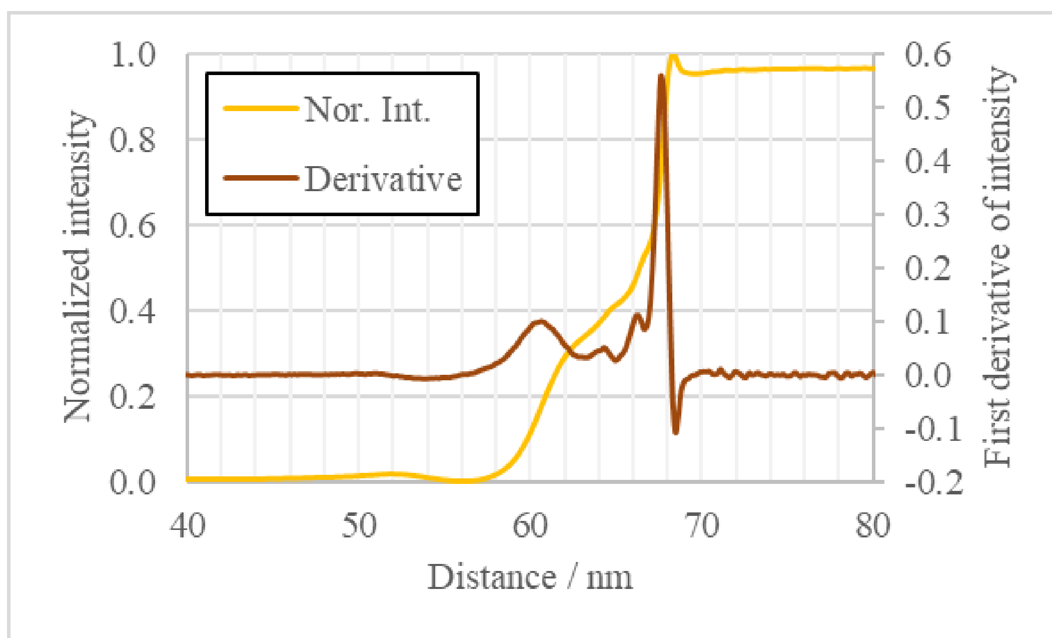

Fig. 3.13 Normalized intensity and its derivative, data from the TEM image of the lamella milled by 5 kV gallium FIB.

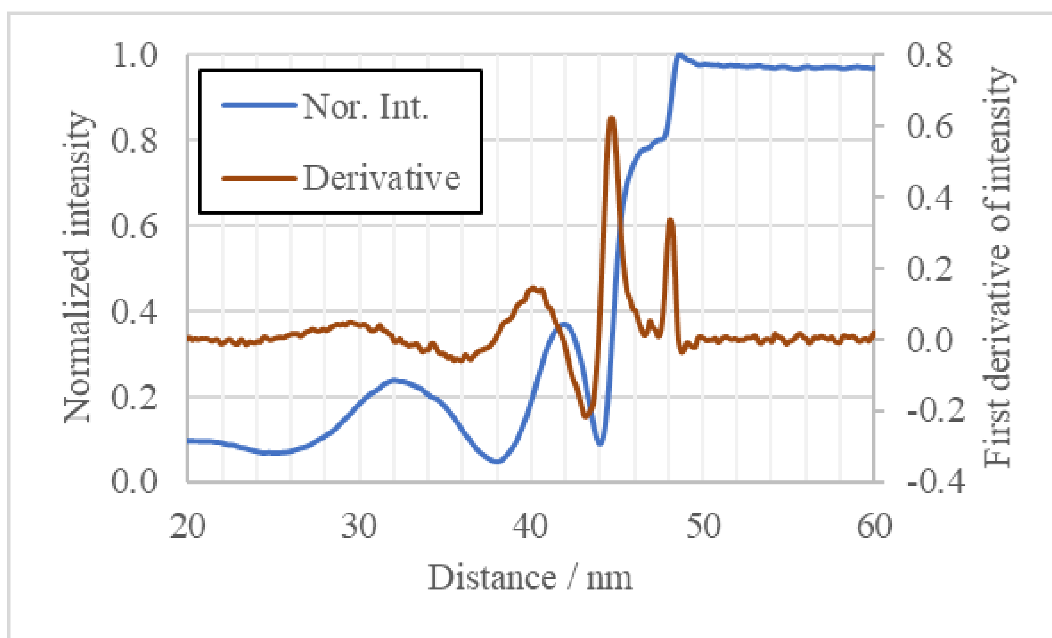

Fig. 3.14 Normalized intensity and its derivative, data from the TEM image of the lamella milled by 2 kV gallium FIB.

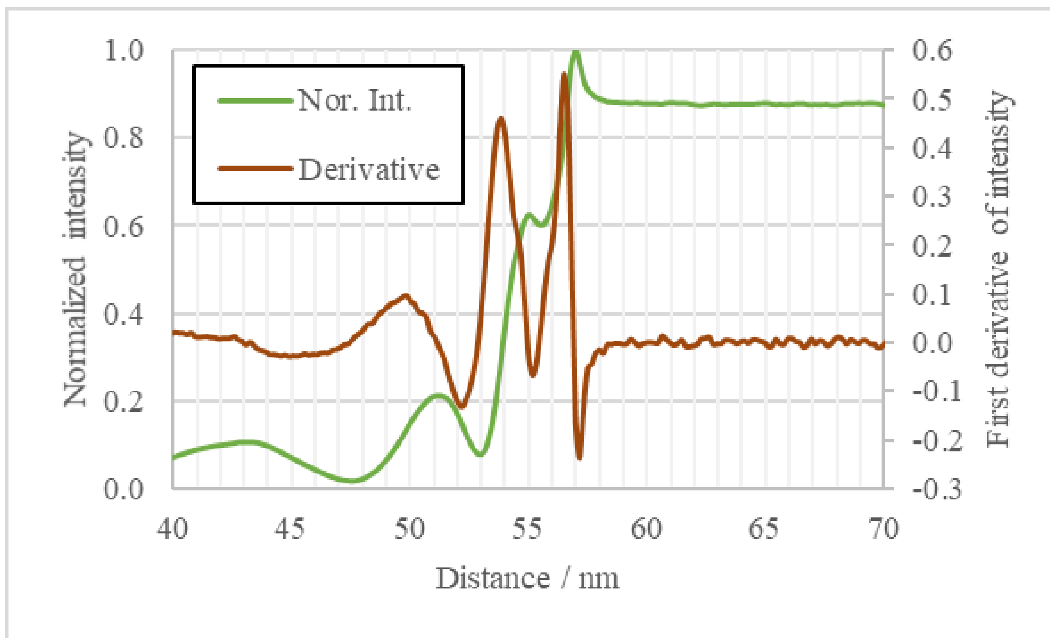

Fig. 3.15 Normalized intensity and its derivative, data from the TEM image of the lamella milled by 1 kV gallium FIB.

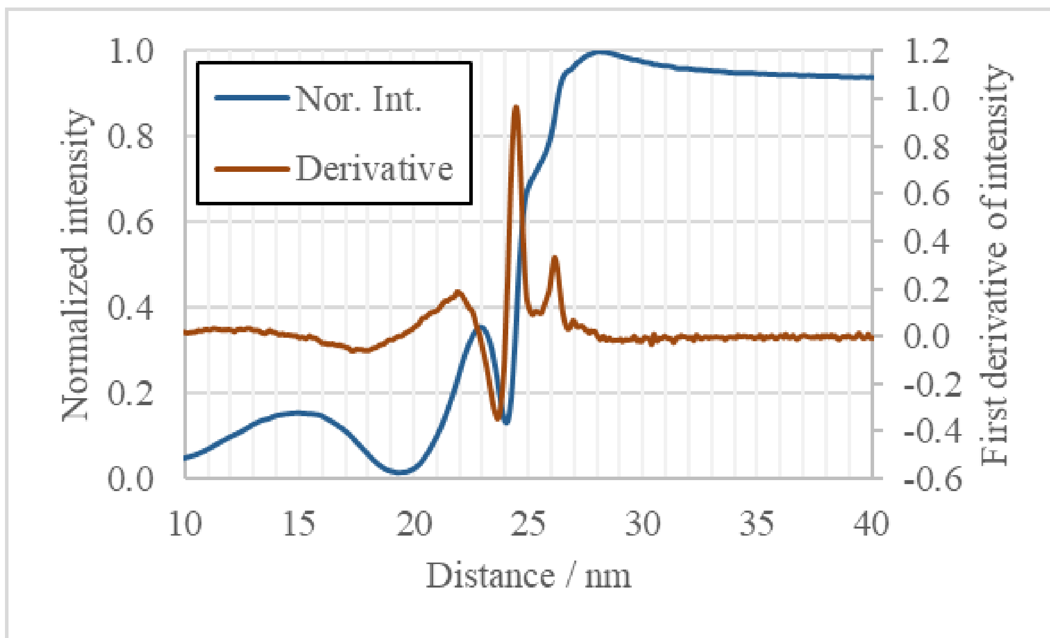

Fig. 3.16 Normalized intensity and its derivative, data from the TEM image of the lamella milled by 0.5 kV gallium FIB.

The amorphous layer thickness data measured from the first peak-to-peak distance from each lamella are listed in Table 3.4.

Energy (kV)	**30**	**5**	**2**	**1**	**0.5**
Thickness (nm)	27.8	7.0	3.3	2.7	1.7

Tab. 3.4 Amorphous layer thickness of the five FIB-milled lamellae for several ion energies. It is determined from the first peak-to-peak distance of the image intensity derivative.

3.3 APT study of gallium FIB ion implantation in silicon

The gallium ion implantation induced by FIB sample preparation is a kind of damage to the specimen, i.e. the implanted gallium changes the properties of the treated material [25, 26]. For example, the electrical conductivity of silicon increases with the gallium implantation, which in some cases is a wanted outcome of the FIB sample preparation and sometimes it is undesired. Therefore, it is important to know quantitatively how much gallium is implanted into the specimen. Although Energy-dispersive X-ray Spectroscopy (EDS) is able to provide elemental information of the specimen after FIB treatment, it is not capable to provide depth profiles of elemental concentration, which is crucial for the optimization of a FIB recipe. Besides the amorphization layer thickness, a maximum concentration of implanted gallium can also be used as an end-point condition of FIB milling. To do this, Atom Probe Tomography (APT) is one suitable option for providing the compositional information of the specimen at nearly atomic level [27-29].

APT provides a spatial elemental information of the specimen with nearly atomic resolution. This is done by extracting specimen atoms by field evaporation, followed by determining their species from the detected mass-to-charge ratio as well as spatial reconstruction. A typical specimen geometry has to be eligible to perform APT experiments; A cone shape needle from the material which contains the region of interest in its center is required. In order to achieve field evaporation of the specimen atoms, the radius of the tip must be in the order of 100 nm. Such a sample preparation is done with FIB milling. That means the APT specimen can be prepared directly from crystalline

silicon. The gallium implanted during the FIB preparation can be detected with APT experiments.

3.3.1 APT experiment procedures

A silicon coupon with a microtip array is used for the Atom Probe Tomography experiment. It enables a statistically large dataset to be collected in a similar operation without breaking the vacuum between different specimen testing. Typically, the successful rate of a single APT experiment is less than 50% because the fragile specimen tip may fracture during the experiments. The risk of specimen fracture increases with the specimen structural complexity. Figure 3.17 shows a typical microtip coupon for APT analysis.

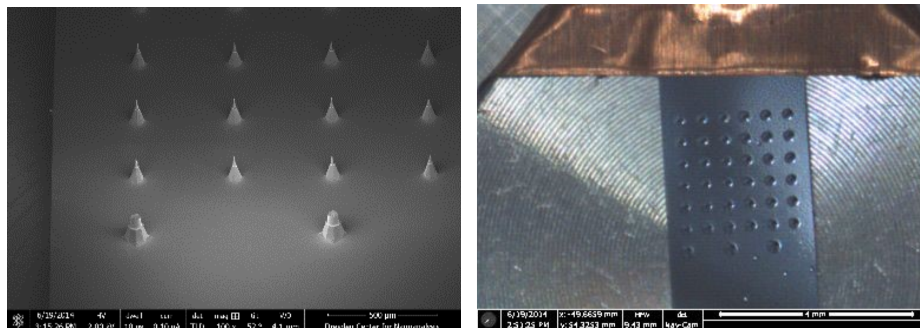

Fig. 3.17 SEM image (left) and optical image (right) of a typical microtip coupon for APT analysis.

There is a 6×5 microtip array on the silicon coupon, along with 3 bigger tips for navigation purpose. Normally, the last row of the microtips are not used, i.e., only 25 microtips are available on a single coupon. The specimen can be mounted on top of each single microtip, forming an electrode in the APT experiment. Therefore, a total of 25 APT experiments with 25 specimens can be performed with one coupon.

As mentioned, a single experiment is likely to fail. For a pure silicon specimen, the success rate is usually above 50%. However, failure of specimen fracture during the experiment tend to happen more often with increasing elemental and/or structural complexity of the material. During the experiment, a large electric field is applied on the microtip to achieve field evaporation at the specimen tip. A heterogeneous structure is unstable under this condition and can lead to fracture of the specimen. Moreover, the specimen is mounted on top of the microtip using GIS-deposited platinum. The quality of the deposition plays a significant role of fixing the specimen on the microtip in the strong electric field.

The first steps to prepare APT specimens with FIB milling are similar to preparing TEM lamellae specimens. A lamella is made from two back-to-back trenches from the specimen substrate. In contrast to the a TEM lamellae, an APT lamella is usually longer for having multiple specimens mounted on the microtip array, and it has two inclining sidewalls instead of the parallel sidewalls of a TEM lamella. The two inclining sidewalls together form a wedge at the bottom of the lamella. This wedge shape is beneficial when mounting the specimen on the microtip with GIS-deposited platinum.

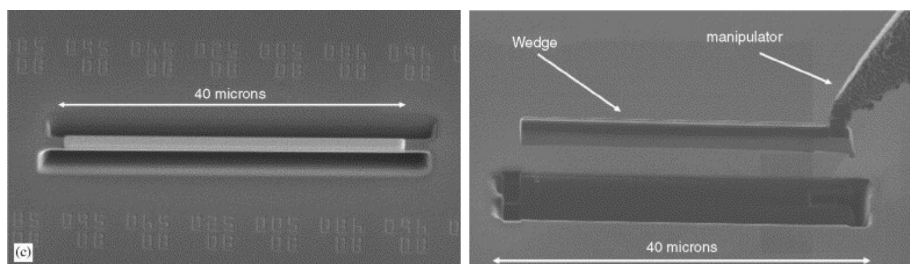

Fig. 3.18 A lamella is extracted from the silicon substrate, similar to TEM lamella preparation [30, 31].

The detail procedure to cut a single specimen from the long lamella and mount it on a microtip is demonstrated in the following 10 steps.

(1) The lift-outed lamella is inserted again and navigated to a desired microtip. The microtip is not sharp at the top. There is a circular platform with a diameter of about 2 μm. The free end of the lamella is aligned above the microtip so that the bottom of the lamella can land on the center of the platform.

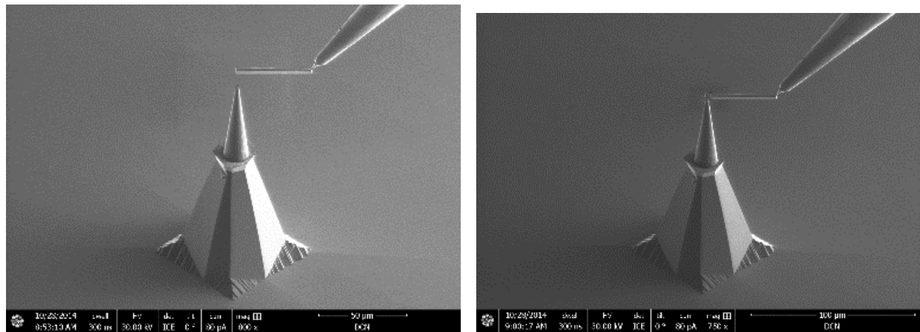

Fig. 3.19 The lamella is placed above a microtip and cut at the free end after mounted with deposited platinum.

(2) Platinum is deposited between the microtip and the bottom of the lamella. After a reasonable amount of platinum is accumulated and the two parts are well mounted together, the ion beam is used with a line milling pattern to cut away the welded part from the remaining lamella.

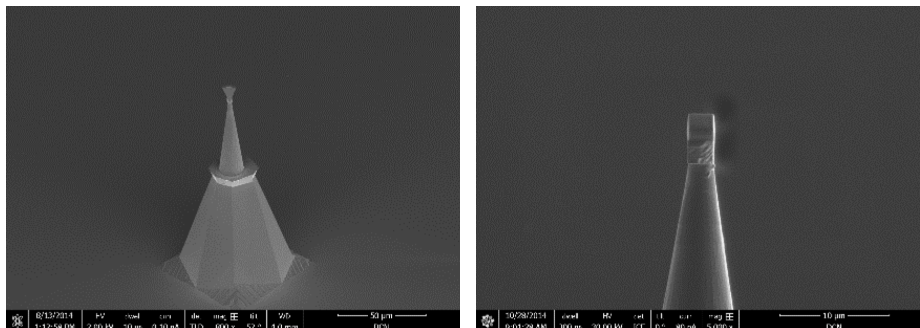

Fig. 3.20 SEM images of a single specimen after being cut from the lamella and fixed on top of the microtip.

(3) Step (1) and (2) are repeated across the microtip array until a desirable number of specimens are prepared.

(4) The stage is rotated by 180˚ and platinum is also deposited on the other side so that the specimen is well supported from both side on the microtip.

(5) The stage is then tilted by 52˚, so that the specimen surface is perpendicular to the ion beam.

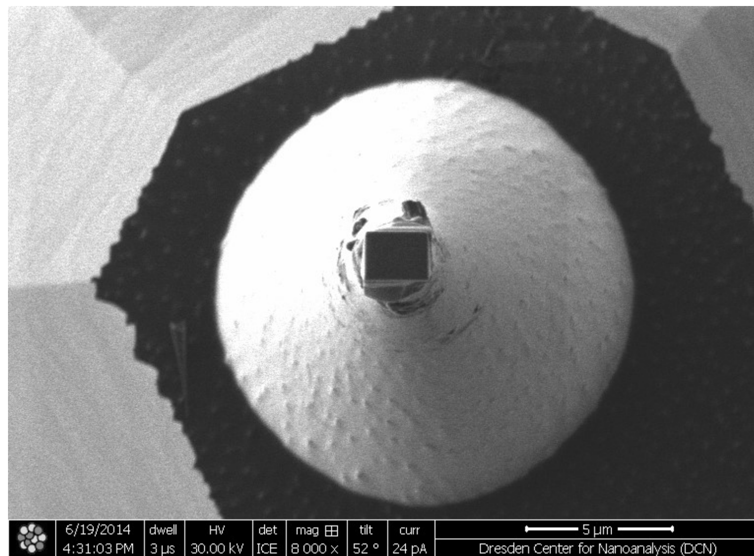

Fig. 3.21 Stage is tilted by 52˚ for normal incidence from the ion beam.

(6) A ring shape milling pattern is applied to the specimen with ion beam of 30 kV acceleration voltage. The outer diameter of the ring should cover the specimen fully and the inner diameter (typically about 500 nm) should be large enough to result in a pillar at the end of the milling. Long dwell time and single pass, as well as outwards milling direction shall be used. It is also helpful to use electron image during the ion milling to monitor the process.

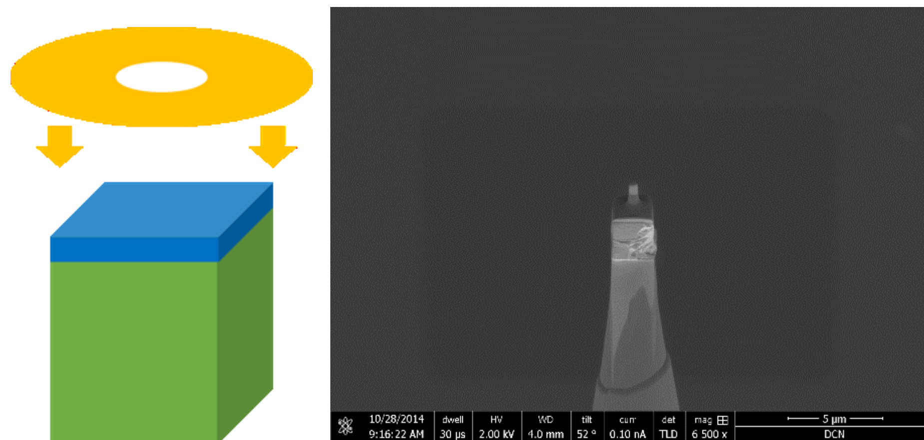

Fig. 3.22 A ring shape milling pattern is applied on the specimen. The outer diameter should cover the whole specimen.

(7) The same ion milling procedure is repeated, however, with a lower acceleration voltage such as 16 kV. The inner diameter of the ring pattern should be reduced to about 150 nm. The dwell time needs also to be reduced and multi-passes should be used. Although the pattern is not a completely filled circle, the pillar will be milled and becomes sharper due to beam spread according to a Gaussian ion beam profile.

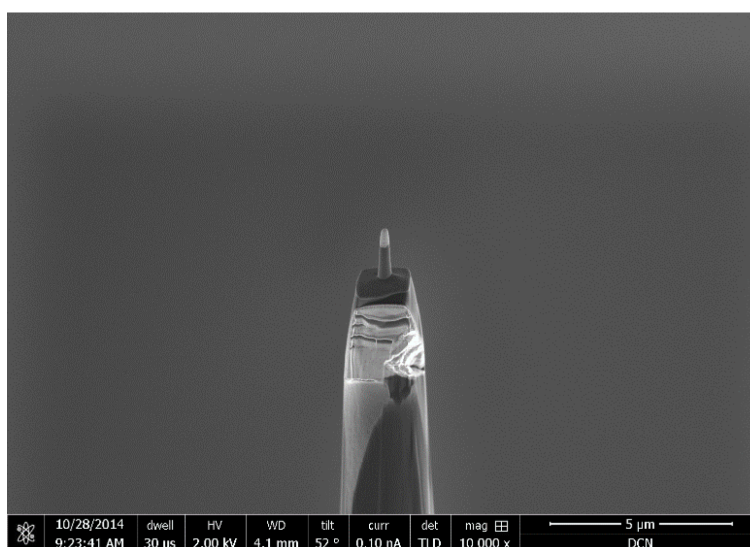

Fig. 3.23 Another ring shape milling pattern is applied on the specimen, with small inner diameter and lower acceleration voltage.

(8) It is very important to ensure that the ion column of the microscope is properly aligned. The milling patterns from the several ion energies should be ideally placed at the same physical location, i.e., the center of the specimen. This ensures that the final geometry is a cone. If the patterns are not aligned, there is a risk of the pillar being milled away and/or the risk of creating a secondary pillar at the outskirt of the specimen. A secondary pillar can severely hinder the process of scouting the center pillar in the later steps.

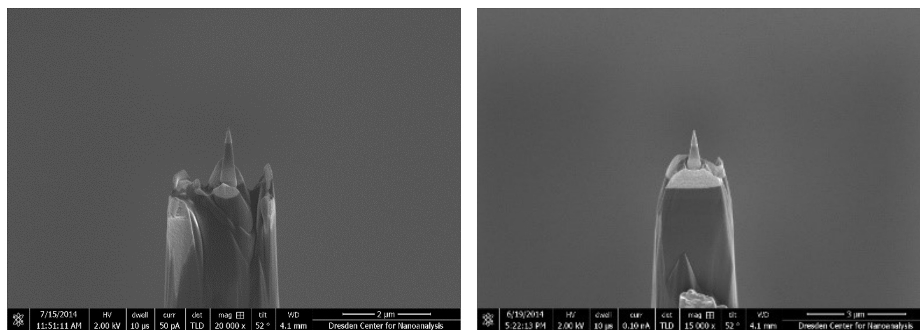

Fig. 3.24 A secondary pillar might be formed if the ring patterns are not aligned, or the outer diameter does not cover the whole specimen.

(9) The last step was performed when the platinum protection layer had been nearly disappeared. The milling pattern should be set with a longer dwell time again and with the final desired acceleration voltage. Unless the region of interest is located on the surface, the platinum protection layer should be removed in order to acquire more information from regions deeper in the substrate. In this case, the pillar is milled additionally 100 nm in the substrate direction. This is not critical because no specific region of interest is desired in the final result, rather it is the FIB milling influence on the side of the cone geometry.

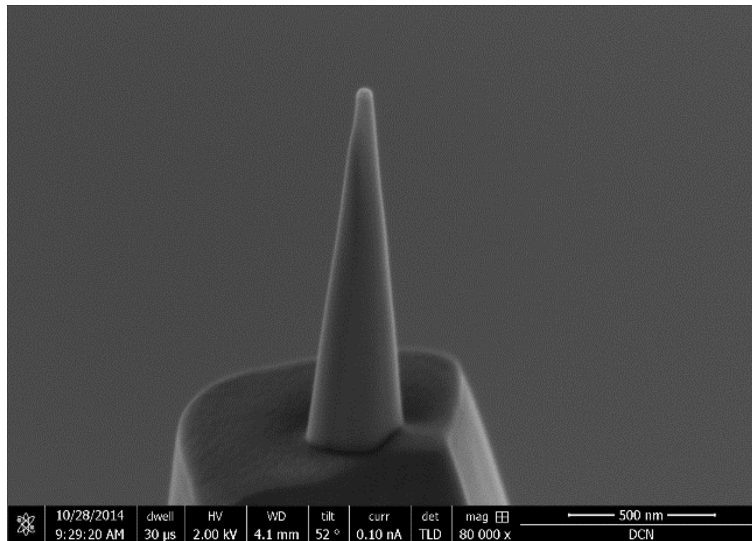

Fig. 3.25 SEM image of a APT-ready specimen with a cone geometry tip.

(10) Typically, the final tip diameter should be less than 50 nm, with a cone angle between 10˚ and 20˚. Field evaporation would not be strong enough with a larger angle. With a too small angle, the field might be so strong that the pillar might face a higher risk of facture during experiment.

Eventually, ten microtips were mounted with specimens. Seven of them were eligible for further APT experiments in terms of geometry requirements, labeled as FT11, FT15, FT16, FT17, FT23, FT31 and FT35. High resolution SEM images of each tip are shown in Figure 3.26.

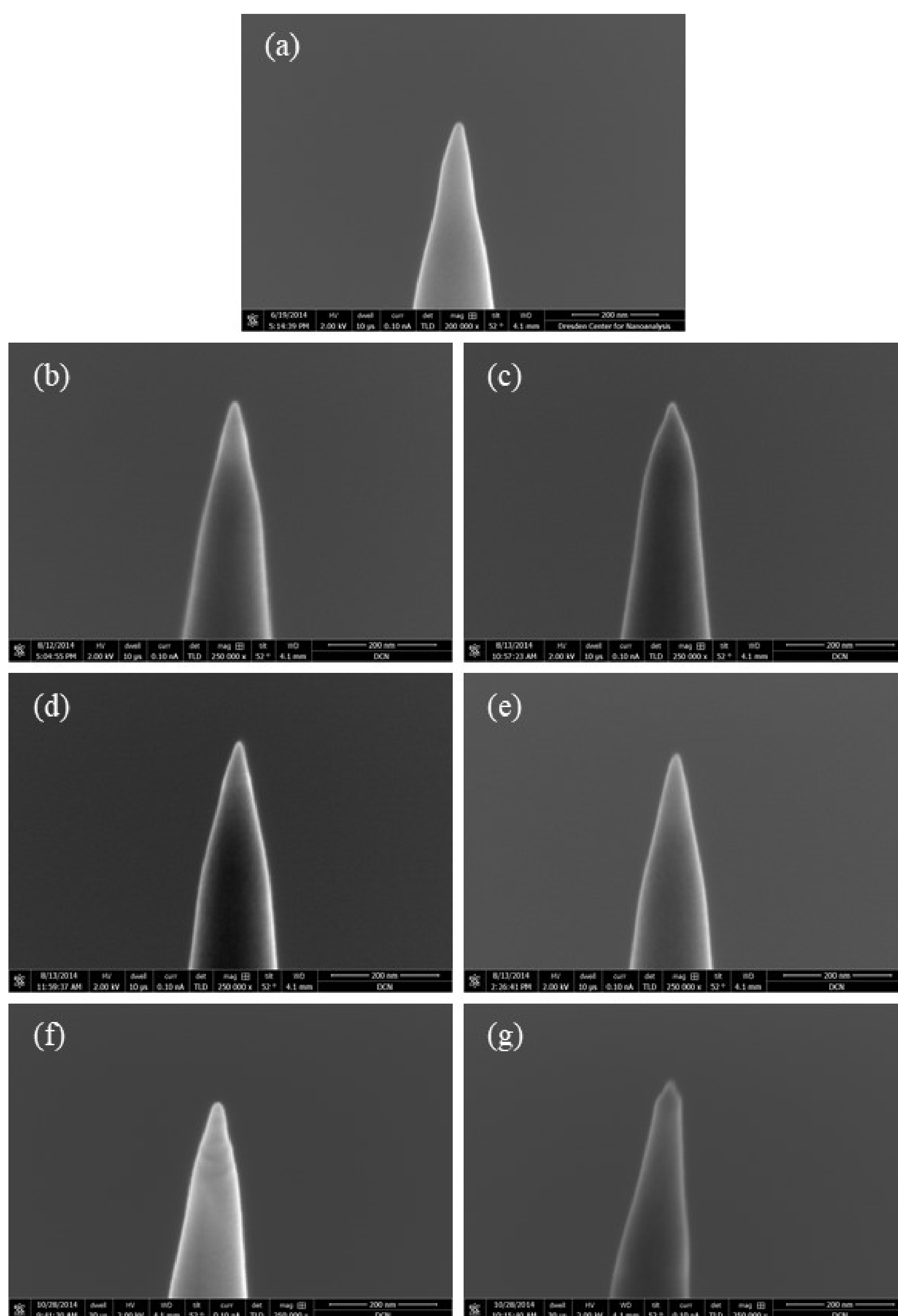

Fig. 3.26 SEM images of the seven microtip eligible for further APT experiment. (a) FT11; (b) FT15; (c) FT16; (d) FT17; (e) FT23; (f) FT31; (g) FT35.

The APT analysis of these seven tips were performed using a Cameca LEAP 3000X Si tool. In the experiments, the temperature was set between 50 K and 80 K, and the laser

power between 0.4 nJ and 0.1 nJ. FT11, FT15, FT31 and FT35 were fractured during the experiments, possibly caused either by unsounded deposition of platinum, or by the high-power laser pulse. High resolution SEM images from the remaining tips were taken and overlapped with their pre-experiment images.

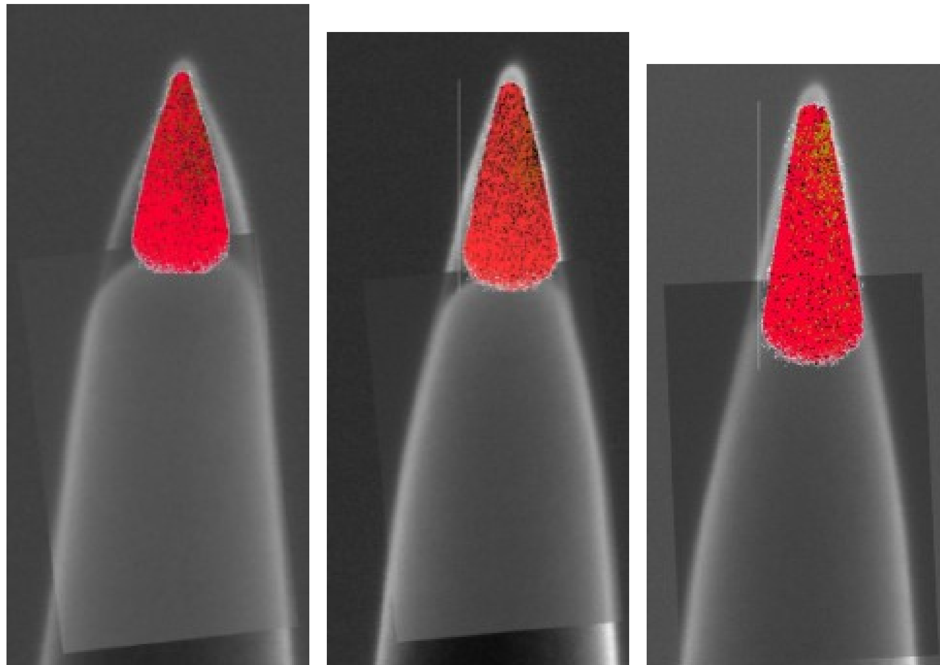

Fig. 3.27 SEM images of post-experiment tips are superposed on the pre-experiment SEM images. The mismatch volume (colored in red) is the evaporated volume during the APT experiments. (left to right: FT16, FT17 and FT23)

From these images, it is estimated that specimen FT16 has an average cone angle of 16˚, whereas it is 15˚ for FT17 and 11˚ for FT23. These angles are arbitrary, and they are the result of non-identical positioning of the ring shape milling pattern among different acceleration voltages used in the FIB preparation.

3.3.2 Data interpretation and visualization

There are two important aspects for tomography data reconstruction: element mapping and dimensions. APT is a time-of-flight mass spectrometry technique, obtaining the mass-to-charge ratio of the detected atoms. By pre-selecting the specific ranges of the mass-to-charge ratio spectrum, corresponding elements can be identified. Although APT has very high spatial resolution in the direction of the cone axis, the spatial location of the data points (atoms) in radial direction usually has to be adjusted. This is due to the fact that the evaporated atoms do not arrive at the flat detector plane at the same time, even if they are on the same parallel plane to the detector, because of the non-uniform local field distribution at the curvature of the tip. The common outcome of this artifact is the "bowing" of a plane layer material. A common way to counteract this is to refer to a known plane layer in the data. By adjusting the bowed layer back to a plane layer, the correct spatial location of the atoms can be restored. However, in this case, the specimen is a featureless silicon tip which has no reference plane layer. Therefore, only an arbitrary minor adjustment is made to these tomography data, which can cause under or over flatting of the tomography. This arbitrary adjustment may introduce a slight artifact in the gallium distribution in the specimen tomography because the gallium atoms are shifted away from their "actual" location.

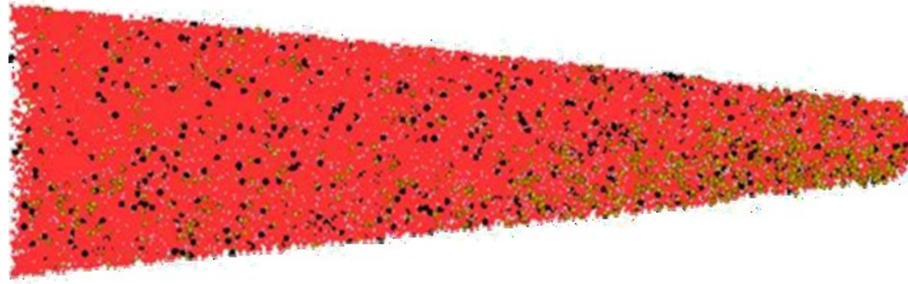

Fig. 3.28 A snapshot of the reconstructed tomography of one specimen. Only silicon (red), gallium (gold) and carbon (black) atoms are shown.

An example of the reconstructed tomography is shown in Figure 3.28. The detected elements can be manually chosen whether to be displayed in the tomography, as well as their percentage of the detected number of atoms. In the example, only silicon, gallium and carbon atoms are shown.

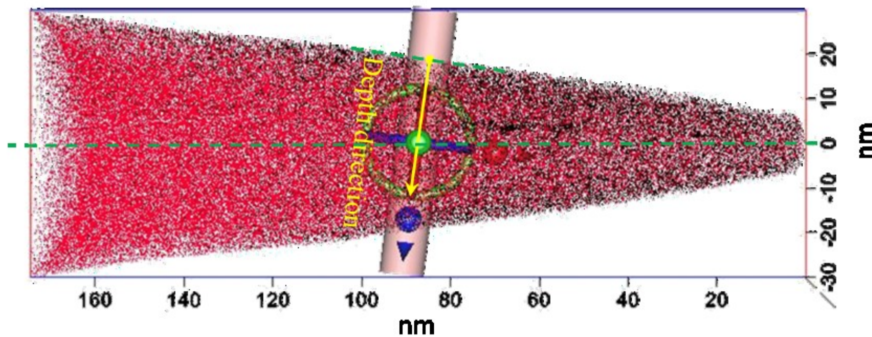

Fig. 3.29 A cylindrical sampling volume with 10 nm diameter was placed perpendicular to the surface at the cross-section plane of the cone.

A ø10 nm cylindrical sampling volume was virtually inserted perpendicularly to the surface of the cone, crossing its axis at the center for each sample. During the FIB preparation of the cone geometry, the ion beam direction was parallel to the cone axis direction. As a result, the ion beam had a glancing angle to the surface of the cone, which

is half of the cone angle. A sampling volume perpendicular to the surface ensures that the later extracted gallium concentration is along the intended "depth" direction. Although the sampling volume can be placed as close to the tip as possible to obtain more accurate data, the presence of the penetrated gallium ions from the other side becomes dominant because of the narrowing tip diameter. Therefore, the sampling volume is placed at a location where the gallium influence from the other side is insignificant. The atomic fraction of gallium along the cylindrical axis of the sapling volume is then integrated on cross-section planes and extracted along the depth direction. Increasing the diameter of the cylindrical sampling volume can include more atoms in the analysis. However, due to the curvature of three-dimensional surface of the specimen, the atoms in one cross-sectional plane of the cylindrical volume are at different depths in the depth direction. Although the same problem exists even in volumes with smaller diameter, the small depth difference can be neglected because of the large aspect ratio of the cylindrical sampling volume. The atomic fraction of gallium in the silicon from five different specimens are plotted in Figure 3.30.

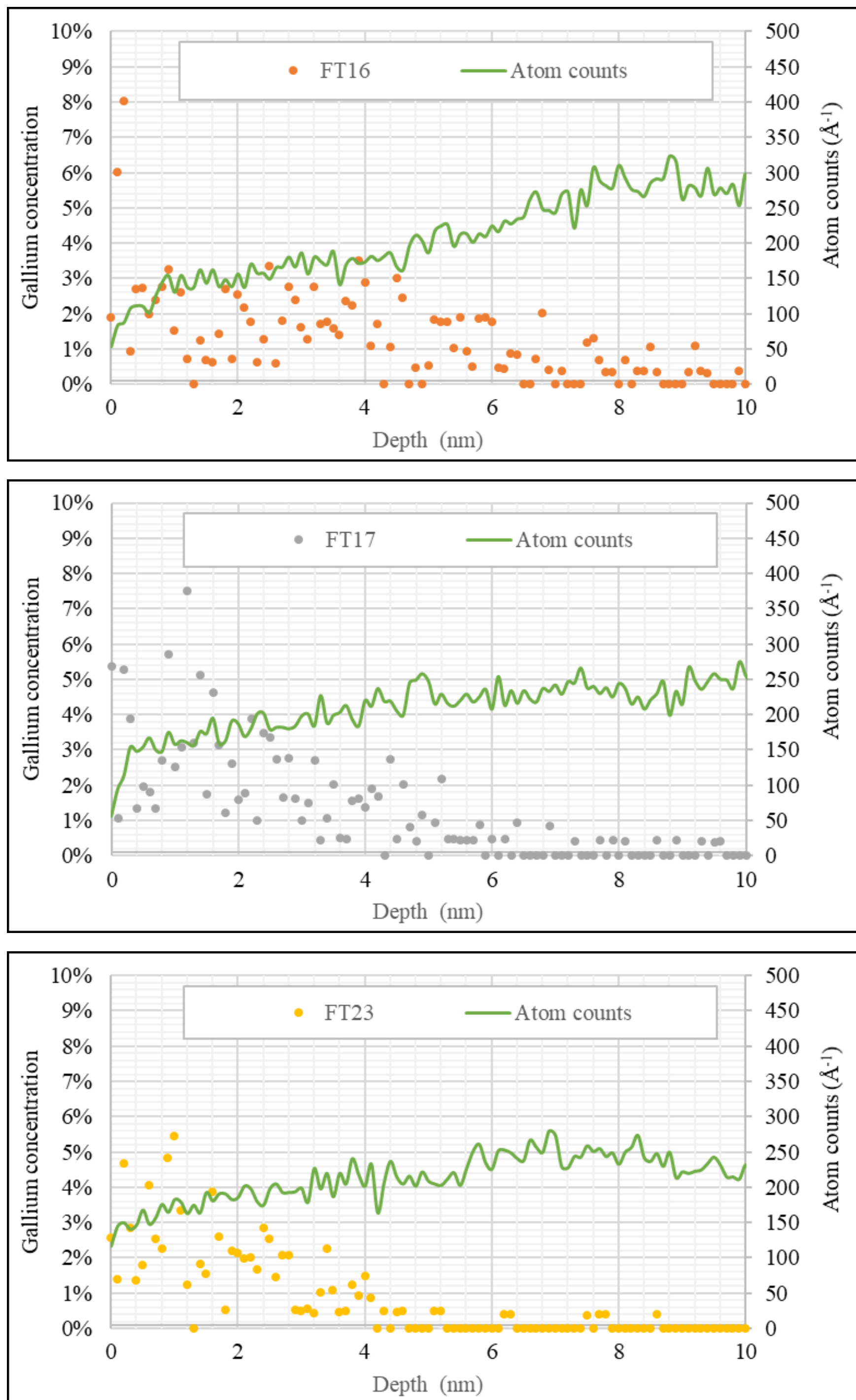

Fig. 3.30 Gallium atomic concentration along silicon substrate depth from 3 APT specimens. Strong scattering is seen at near surface.

References

1. Giannuzzi, L.A. and F.A. Stevie, *A review of focused ion beam milling techniques for TEM specimen preparation.* Micron, 1999. **30**(3): p. 197-204.

2. Patterson, R., et al., *"H-Bar Lift-Out" and "Plan-View Lift-Out": Robust, Re-thinnable FIB-TEM Preparation for Ex-Situ Cross-Sectional and Plan-View FIB Specimen Preparation.* Microscopy and Microanalysis, 2002. **8**(S02): p. 566-567.

3. Park, K.-h., *Cross-sectional TEM specimen preparation of semiconductor devices by focused ion beam etching.* MRS Online Proceedings Library Archive, 1990. **199**.

4. Nakahara, S., *Recent development in a TEM specimen preparation technique using FIB for semiconductor devices.* Surface and coatings technology, 2003. **169**: p. 721-727.

5. Giannuzzi, L., et al., *Focused ion beam milling and micromanipulation lift-out for site specific cross-section TEM specimen preparation.* MRS Online Proceedings Library Archive, 1997. **480**.

6. Giannuzzi, L.A., et al., *Applications of the FIB lift -out technique for TEM specimen preparation.* Microscopy research and technique, 1998. **41**(4): p. 285-290.

7. Uchic, M.D., et al., *Augmenting the 3D characterization capability of the dual beam FIB-SEM.* Microscopy and Microanalysis, 2004. **10**(S02): p. 1136.

8. FEI Company *Auto Slice and View*. 2005.

9. Wilhelmi, O., et al., *Rapid prototyping of nanostructured materials with a focused ion beam.* Japanese Journal of Applied Physics, 2008. **47**(6S): p. 5010.

10. Kim, C.-S., S.-H. Ahn, and D.-Y. Jang, *Developments in micro/nanoscale fabrication by focused ion beams.* Vacuum, 2012. **86**(8): p. 1014-1035.

11. Rajsiri, S., et al., *FIB damage in silicon: Amorphization or redeposition.* Microsc. Microanal, 2002. **8**(Suppl 2).

12. Langer, E., et al. *FIB induced damages of SEM/TEM samples of semiconductor devices*. in *4 th European FIB Users Group Meeting (EFUG2000)*. 2000.

13. Mayer, J., et al., *TEM sample preparation and FIB-induced damage.* MRS bulletin, 2007. **32**(5): p. 400-407.

14. Rubanov, S. and P. Munroe, *FIB - induced damage in silicon.* Journal of Microscopy, 2004. **214**(3): p. 213-221.

15. Giannuzzi, L.A., R. Geurts, and J. Ringnalda, *2 keV Ga+ FIB milling for reducing amorphous damage in silicon.* Microscopy and Microanalysis, 2005. **11**(S02): p. 828.

16. FEI Company *Helios NanoLab 660*. 2013.

17. Santamore, D., et al., *Focused ion beam sputter yield change as a function of scan speed.* Journal of Vacuum Science & Technology B: Microelectronics and Nanometer Structures Processing, Measurement, and Phenomena, 1997. **15**(6): p. 2346-2349.

18. Vasile, M.J., J. Xie, and R. Nassar, *Depth control of focused ion-beam milling from a numerical model of the sputter process.* Journal of Vacuum Science & Technology B: Microelectronics and Nanometer Structures Processing, Measurement, and Phenomena, 1999. **17**(6): p. 3085-3090.

19. Lugstein, A., et al., *FIB processing of silicon in the nanoscale regime.* Applied Physics A: Materials Science & Processing, 2003. **76**(4): p. 545-548.

20. McCaffrey, J., M. Phaneuf, and L. Madsen, *Surface damage formation during ion-beam thinning of samples for transmission electron microscopy.* Ultramicroscopy, 2001. **87**(3): p. 97-104.

21. Kato, N., Y. Kohno, and H. Saka, *Side-wall damage in a transmission electron microscopy specimen of crystalline Si prepared by focused ion beam etching.* Journal of Vacuum Science & Technology A: Vacuum, Surfaces, and Films, 1999. **17**(4): p. 1201-1204.

22. Fultz, B. and J. Howe, *Diffraction Contrast in TEM Images*, in *Transmission Electron Microscopy and Diffractometry of Materials*. 2013, Springer. p. 349-427.

23. Schalkoff, R.J., *Digital image processing and computer vision*. Vol. 286. 1989: Wiley New York.

24. Canny, J., *A computational approach to edge detection.* IEEE Transactions on pattern analysis and machine intelligence, 1986(6): p. 679-698.

25. Tamura, M., et al., *Focused ion beam gallium implantation into silicon.* Applied Physics A: Materials Science & Processing, 1986. **39**(3): p. 183-190.

26. Prewett, P., et al., *Gallium staining in FIB repair of photomasks.* Microelectronic Engineering, 1993. **21**(1): p. 191-196.

27. Miller, M.K., *Atom probe tomography: analysis at the atomic level*. 2012: Springer Science & Business Media.

28. Miller, M.K. and R. Forbes, *Atom probe tomography.* Materials Characterization, 2009. **60**(6): p. 461-469.

29. Kelly, T.F. and M.K. Miller, *Atom probe tomography.* Review of Scientific Instruments, 2007. **78**(3): p. 031101.

30. Thompson, K., et al., *In situ site-specific specimen preparation for atom probe tomography.* Ultramicroscopy, 2007. **107**(2): p. 131-139.

31. Miller, M.K., et al., *Review of atom probe FIB-based specimen preparation methods.* Microscopy and Microanalysis, 2007. **13**(6): p. 428-436.

Chapter 4

Beam Induced Polishing System

For High Resolution Transmission Electron Microscopy (HRTEM), sample preparation is the most crucial step in obtaining atomically resolved images. Focused Ion Beam (FIB) milling is typically used to prepare electron transparent lamellae especially for target preparation [1-3]. When site-specific preparation is not necessary, another common technique is to combine classical sample preparation [4] (dicing, grinding, dimpling) and broad argon ion-beam milling [5]. More often, the two practices are combined. Specimens are usually FIB-milled down to a certain thickness that is close to the target, and then transferred ex-situ to broad argon ion-beam milling tools as the last step of the sample preparation to achieve the final thickness as well as to remove the layer damaged by FIB milling.

One of the advantages of sample preparation with FIB milling is a precise selection of the region of interest and of the specific specimen orientation. Compared to conventional preparation, state-of-the-art FIB tools offer a high sputter rate, which translates into short preparation time. However, material alteration, redeposition, surface roughness and selective sputtering are typical damages as a drawback of this technique. What is even more critical is that FIB milling results in near-surface amorphization of crystalline material, and consequently, it severely hinders the subsequent TEM analysis. As mentioned in the previous chapter, the degree of amorphization depends mostly on the acceleration voltage and the resulting ion energy. Although low-energy FIB milling mitigates the situation, the advantages of high accuracy positioning and high milling rate are diminished if low-energy ions are used. On the other hand, broad argon ion-beam milling provides an alternative of low-damage milling with high milling rate. Inert argon gas is ionized at varies energy and forms an ion flux with a beam diameter in the

millimeter range [6]. Although the penetration depth in silicon of light (low-Z) ions is larger than that of heavy (high-Z) ions (in this case argon versus gallium), the low-energy ions create a thinner damage layer of the specimen. As a result, the relatively thick FIB-induced damage layer can be removed by the low-energy ions and only a thin damage layer remains on the specimen. To achieve a high sputtering rate, the ion flux must be large enough, which is practically achieved with standalone equipment dedicated for this purpose. Combining the advantages of both methods, a TEM lamella is usually fabricated with FIB in a dual-beam microscope and subsequently transferred ex-situ to a broad argon ion-beam milling tool for final polishing to remove the damage layers.

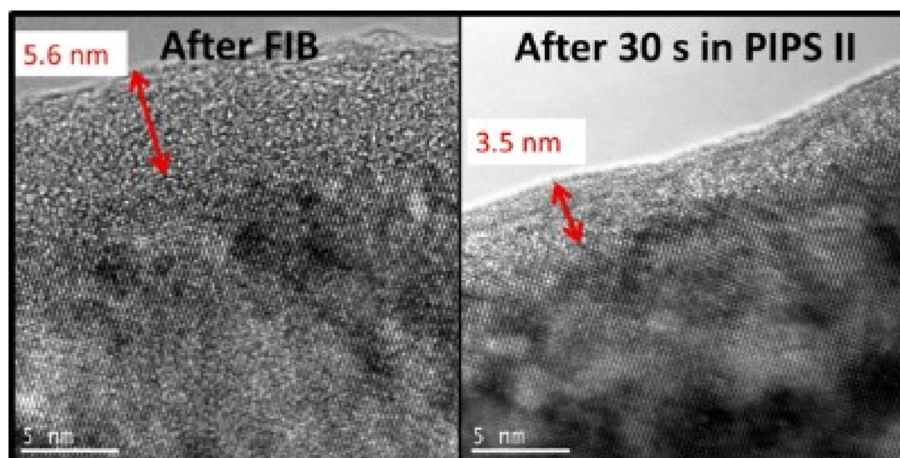

Fig. 4.1 Removal of FIB produced amorphous surface layers on specimen by an argon ion polishing system (PIPS II) [7].

4.1 BIPS hardware configuration

A novel Beam Induced Polishing System (BIPS) has been designed as an attachment to a commercial dual-beam tool (FEI Helios 660) [8]. Over the course of the experiments, the system configuration was modified several times. Only the latest version

of setup is described here. The system can be functionally separated into two parts: Argon purification and specimen polishing. The argon purification is done within the hardware installed outside of the vacuum chamber, whereas the purified argon is then guided into the chamber for specimen polishing.

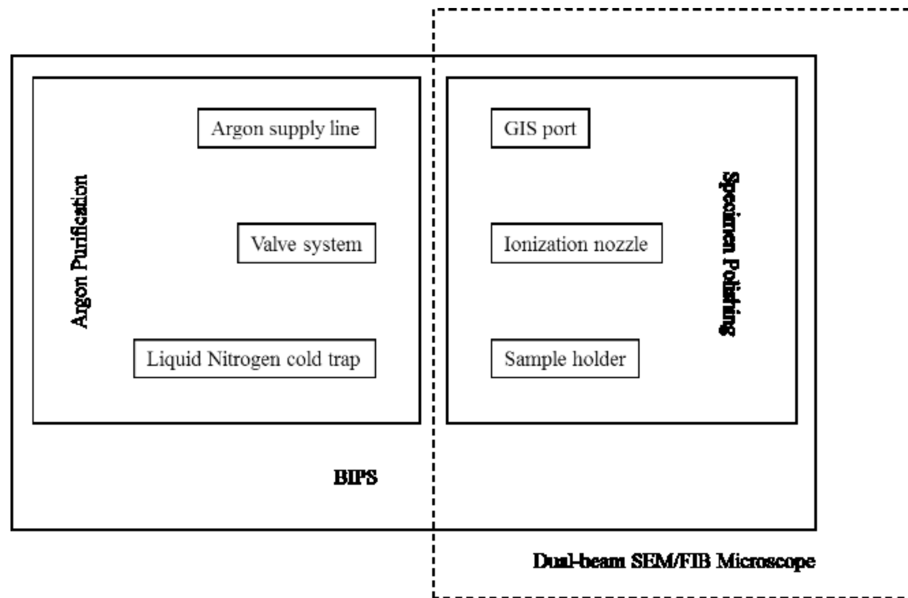

Fig. 4.2 A system scheme of the Beam Induced Polishing System (BIPS). It can be functionally divided into two parts located outside and inside of the SEM/FIB dual-beam tool.

4.1.1 Argon supply line

The Argon supply line consists of two steel gas line with an inner diameter of 5 mm, separated by a pressure regulator. The first part connects the compressed argon gas bottle with the pressure regulator. It is about 10 m long and at 10 bars of constant pressure. The pressure regulator connects the two parts of the line and has a pressure gauge on both side. The pressure in the second half of the line can be adjusted freely from 0 to 4 bars. In this case it is reduced to 1 to 2 bars. The pressure behind the pressure regulator is

defined as “line pressure” in the following text. The end of the supply line is connected with the valve system.

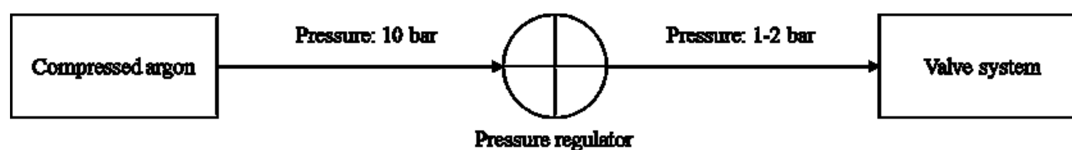

Fig. 4.3 Argon pressure from the supply line is reduced by a pressure regulator from 10 bars to 1-2 bars.

4.1.2 Valve system

The valve system controls the gas flow within the “argon purification” sector of the system. It consists of three pneumatic valves, one needle valve and one manual valve. The manual valve does not serve the purpose of argon purification. It is only an auxiliary valve for venting the pipeline before and after the operation (venting the pipeline via the GIS is too slow for practical use). A line valve separates the valve system from the argon supply line. A needle valve is located behind the line valve and limits the gas flux once the line valve is open. Followed by the needle valve are the pressure inlet valve and pressure outlet valve. The liquid nitrogen cold trap is located in between the inlet and outlet valves. It is responsible for the actual argon purification function.

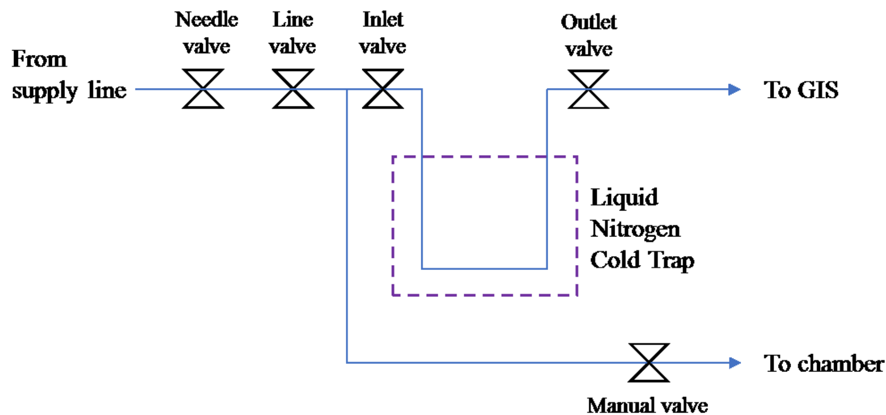

Fig. 4.4 A scheme of the valve system of BIPS. Needle and line valves isolate the rest of the system from the supply line. Inlet and outlet valves control the gas flow in and out of the LNCT.

4.1.3 Liquid Nitrogen Cold Trap

High purity argon gas is required to achieve a proper sputtering result. Impurities in the gas such as oxygen or water vapor increases oxidation during the milling process and suppress the sputter rate. These impurities may be originated from the gas supply due to imperfect manufacturing, or from the long pipeline in the form of adsorbates or from diffusion through seals or along the pipe itself. Particularly, water vapor will not only be absorbed on the inner surface of the pipeline after hardware installation, it also diffuses into the line from atmosphere through small leaks or rubber seals. Therefore, it is crucial to pump the entire pipeline to achieve an ultra-high vacuum for a certain period of time to evacuate the residual air from the installation. A better approach would be heating the pipeline during pumping.

Besides this global systematic method, another approach to get highly purified argon is to perform a "cleaning" procedure for each operation. This is done with a liquid nitrogen cold trap (LNCT) located between the inlet valve and outlet valve. The LNCT

consists of a liquid nitrogen Dewar flask and a spiral pipeline going in and out of the Dewar flask.

Fig. 4.5 Liquid nitrogen cold trap (LNCT) with a Dewar flask and a spiral pipeline going in and out of the flask.

Argon and impurity (mainly water) are condensed at liquid nitrogen temperature (-196°C) in the spiral when it is submerged in the Dewar flask. By increasing the distance between the spiral and the liquid nitrogen, the temperature rises above the boiling point of argon (-186 °C). Until the temperature returns to 0 °C, only argon can escape from the LNCT and water is trapped. A bundle of braided stranded copper wires is attached to the spiral and dipped into the liquid nitrogen, acting as a temperature buffer to prevents the abrupt temperature increase and to keep the spiral below 0 °C as long as possible.

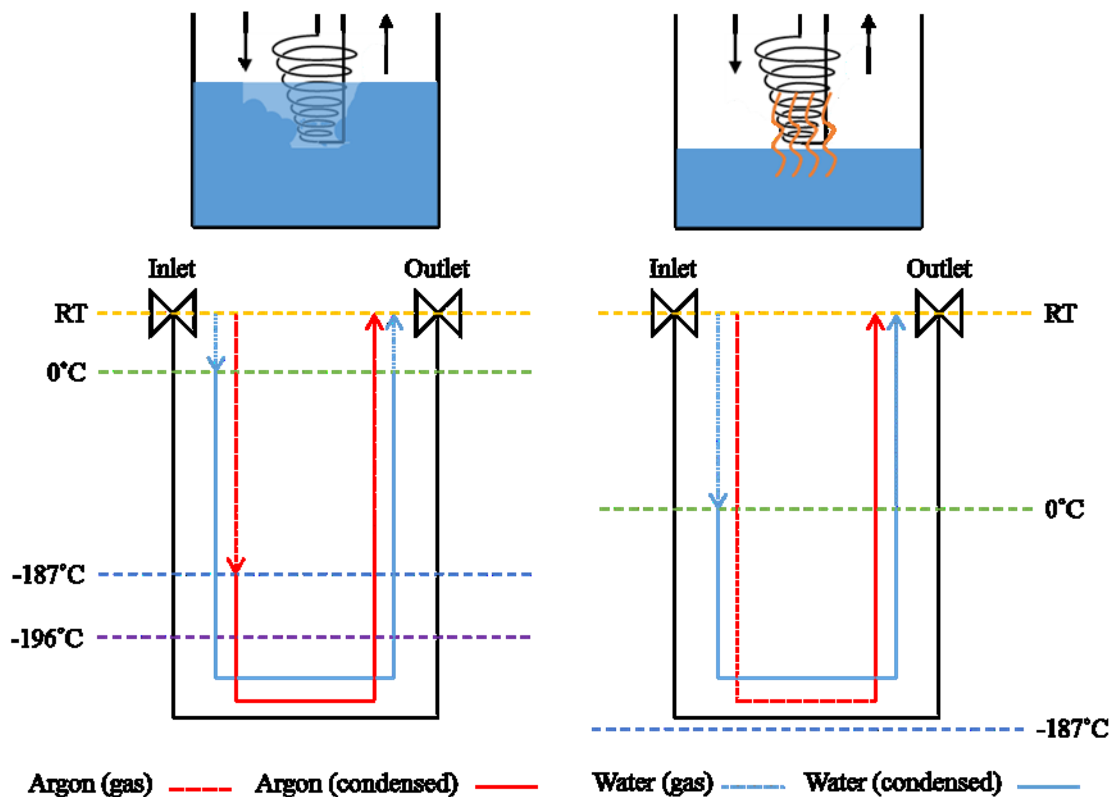

Fig. 4.6 Illustration of the argon purification in the LNCT. Due to existence of a temperature gradient between 0˚C and RT, a volume of water cannot be trapped in the LNCT.

However, in practice, the outlet valve is located outside of the Dewar flask. This creates a temperature gradient between room temperature (RT) at the outlet valve and the temperature at the spiral. That means, in this gradient, a volume of argon will not be purified, due to the existence of uncondensed water when the local temperature is above 0 °C. This principle is illustrated in Figure 4.6.

4.1.4 Gas Injection System (GIS) port

When sufficient purified argon has been built up at the exit of the LNCT with the temperature rise, the outlet valve is switched open. The argon is then guided into one of the ports of the Gas Inject System (GIS).

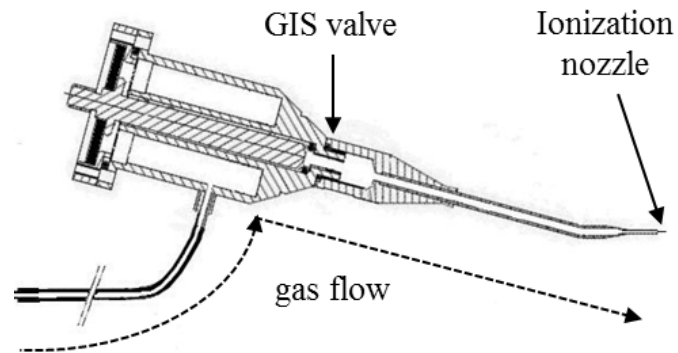

Fig. 4.7 A simplified sketch of the Gas Injection System (GIS) port of the BIPS system [9].

A vacant Gas Inject System (GIS) port is used to store the purified argon from outlet valve for the final polishing operation. The outlet valve remains open until the GIS reaches the desired pressure for operation.

4.1.5 Ionization nozzle

A tungsten nozzle with an inner diameter of 25 µm and an outer diameter of 100 µm is mounted as the outlet of the GIS. When the GIS valve is set open, the stored argon gas flows through the nozzle. The argon is then ionized before being delivered to the specimen by an electric field.

Figure 4.8 shows schematically how the argon is being ionized inside the nozzle. A "letterbox" opening is pre-fabricated using Focused Ion Beam milling near the end of the nozzle, creating access for the electron beam to ionize the argon gas flowing through. An SEM image of the "letterbox" opening on the nozzle is shown Figure 4.9.

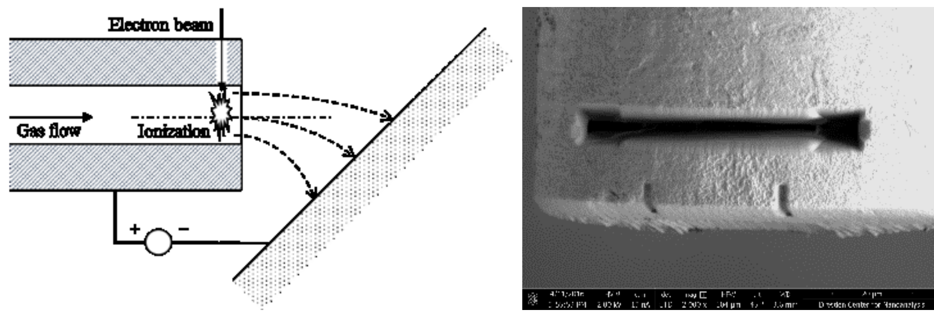

Fig. 4.8 (left) Schematic of the cross-section of the nozzle.
Fig. 4.9 (right) Top-view SEM image of the letterbox opening at the nozzle.

The "letterbox" opening should be as small as possible to minimize the disturbance to the gas flow inside the nozzle. However, it should be large/wide enough to allow the electron beam to scan across the whole inner diameter in order to have maximum ionization. The nozzle is mounted horizontally so that the electron beam penetrates through the opening from above without hitting the sidewalls. Ionization of the argon is triggered by both direct and indirect interaction with the electron beam. Between the two, a major part of the ionization is caused by the secondary electrons generated from the inner wall of the nozzle when the primary electron beam hits its surface. To optimize ionization yield, the electron beam acceleration voltage is set at 2 kV, achieving maximum secondary electron yield.

The nozzle has an electrical potential difference from the specimen surface. This is accomplished by a negative stage bias. The generated electrical field directs the e-beam generated ions towards the desired location on the specimen surface, subjected to the potential difference, ionization energy, gas flow pressure and spatial geometry. The location where the argon ions hit the specimen surface is mainly determined by the stage bias, specimen geometry, specimen material and spatial distance between nozzle and the specimen.

4.1.6 Sample holder

Eventually, the specimen to be polished in the BIPS system is a lift-out lamella. After extraction of the specimen from the bulk substrate, the lamella can be either still attached at the micro-manipulator, or already mounted on the TEM grid. The desired polishing surface faces both the ionization nozzle and the electron beam at 45˚, respectively. However, polishing the other side of the lamella may be more challenging if no custom made TEM grid is used. A possible solution is to compromise the imaging/monitoring the lamella during the BIPS process, i.e. imaging of the polishing pattern with the electron beam is not possible with the stage orientation during the process. This can be done by orienting the lamella with respect to the ionization nozzle and the electron beam direction as schematically shown in Figure 4.10.

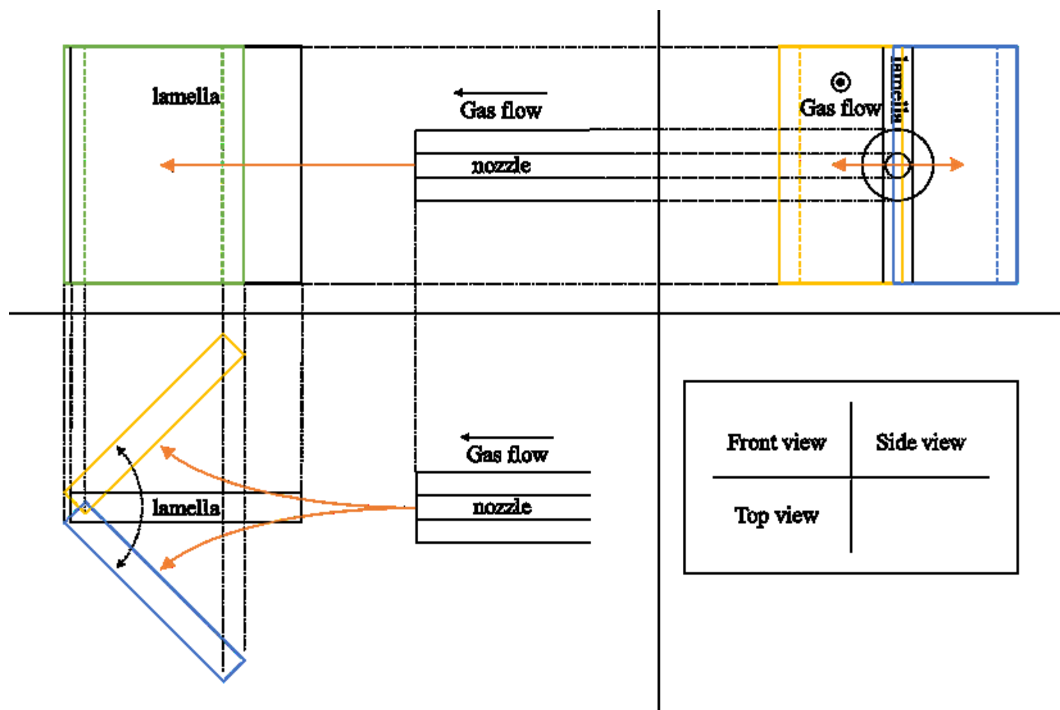

Fig. 4.10 A possible sample orientation for the BIPS process. Both sides of the lamella are polished but SEM imaging is not possible as the surface is parallel to the beam direction.

The lamella is vertically mounted and positioned so that the region of interest is approximately located at the same height of the ionization nozzle. By rotating the lamella along its vertical axis, the ionized argon is targeted onto the lamella by the electrical field created by the stage bias between the nozzle and the lamella. In this configuration, the electron beam direction is parallel to the sample surface. Therefore, SEM images of the pattern cannot be made [10].

A series of simulations with varying parameter sets were performed to successfully bombard the target region with argon ions. For this proof-of-concept study, such a lamella configuration was not established. Instead, a simple flat specimen substrate was tested.

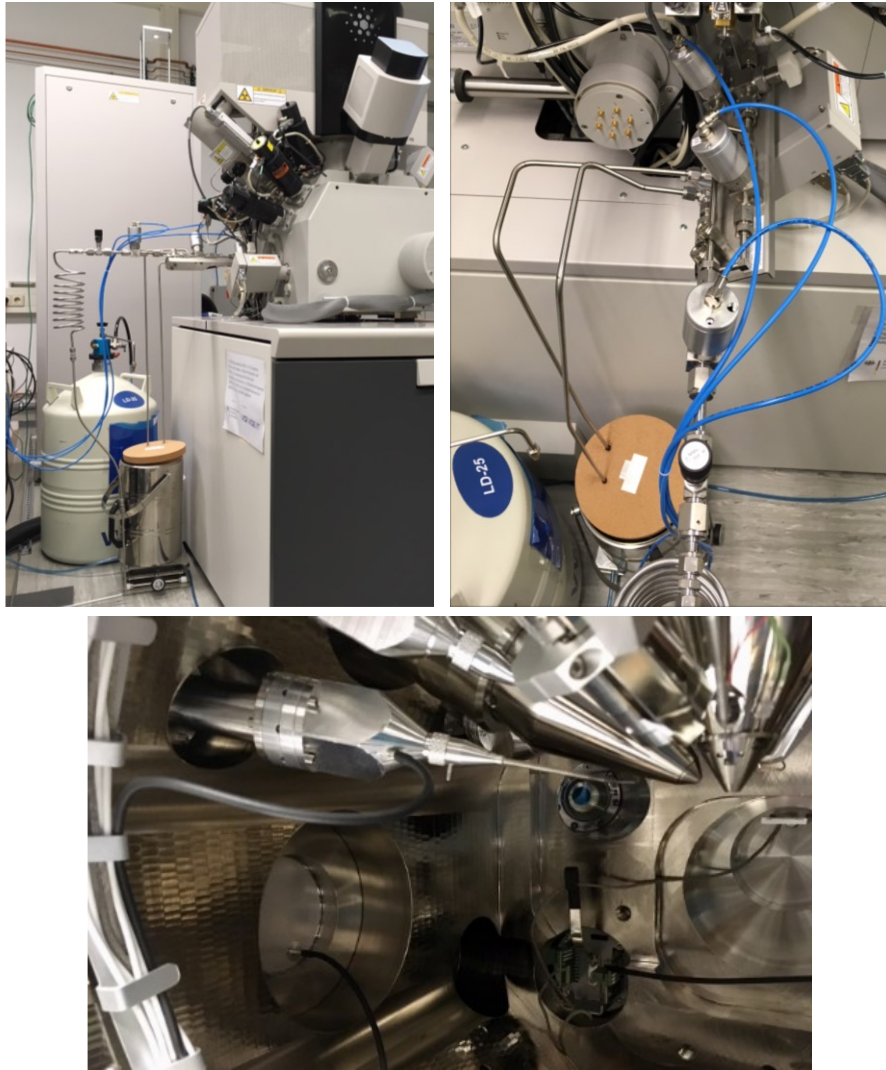

Fig. 4.11 Photos of the BIPS hardware configuration.

4.2 BIPS experiment procedure and results

The argon polishing process consists of both sputtering and oxidation. The challenge is to fine-tune the work flow among each subsystem to have the high purity argon at the nozzle, in which ionization happens, so that the sputter rate can exceed the oxidation rate on the specimen surface.

Once the system is stabilized, i.e. sputtering dominates oxidation on the specimen surface, a clear "BIPS spot" is seen. Typically, the spot has an elliptical shape with a bright halo around. The darker spot represents the bare specimen substrate after being polished by the ion beam and the bright halo is caused by the unwanted oxidation.

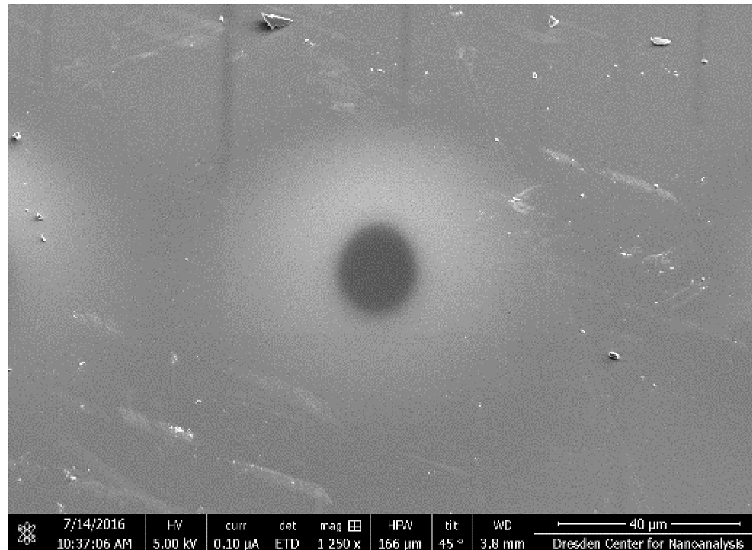

Fig. 4.12 SEM image of a typical "BIPS spot" with a dark center (bare specimen surface) and a bright halo (oxidation).

Parameters like milling time, stage bias or distance influences the size of the spot. In this thesis, BIPS experiments were performed on three different specimens named SiOx1, SiPt and SiOx2. For each specimen, six stage biases were tested, resulting in six different BIPS spots accordingly (300V/250V/200V/150V/100V/75V). Except for the argon pressure, all the other parameters were kept the same in all experiments, which are referred to as "standard parameters" in the following text.

- Specimen SiOx1: a pure silicon wafer fragment with unknown thickness of native oxide.
- Specimen SiPt: a fragment from a silicon wafer substrate coated with 23 nm platinum.

- Specimen SiOx2: a pure silicon wafer fragment with unknown thickness of native oxide.

E-beam Voltage	e-beam current	Milling time	Distance	Pressure
2 kV	100 nA	60 s	100 µm	2-1x10^{-5} mbar

Tab. 4.1 Standard parameters of BIPS procedure

As stated, a significant part of the ionization is caused by the secondary electrons generated at the nozzle inner sidewall when the electron beam scans over. At 2000 V acceleration voltage, the ionization from the argon gas reaches the highest yield as the secondary electron yield does. 100 nA is the largest e-beam current provided on the dual-beam tool used. As a principle, the stronger the electron beam current is, the stronger the generated ion flow will be. The milling time of the BIPS is the time that the electron beam scans (ionizes) the argon gas. Due to the non-synchronization between the valve action and beam switch, as well as beam blanking during the scanning, the argon gas flow last longer than the milling time. There exists gas flow before the ionization, after the ionization and during the beam blank. And the distance in the standard parameters and also shown in Figure 4.13 is the vertical distance between the bottom of the nozzle and the specimen surface.

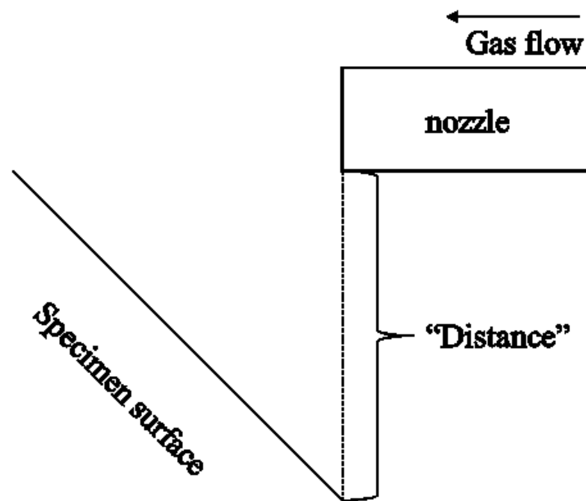

Fig. 4.13 Vertical distance between the nozzle and the specimen surface.

Depending on the state of the argon, the gas volume in the BIPS can be separated into three parts, as illustrated in Figure 4.14. The orange volume is considered unpurified argon under line pressure at room temperature constantly. Step 1 is to remove the residue gas/vapor from the previous operation behind this volume. The purification of the argon is done in steps 2 to 4 in the volume indicated in blue color. Purified argon escapes this part as gas form while leaving the water behind in the cold trap. After filling the GIS volume, colored in green, in step 5, the cold trap volume is set back to liquid nitrogen temperature in step 6. The GIS volume is rather limited and often not sufficient for usage of more than 10 polishes. When the GIS volume is depleted, step 3 should be repeated to obtain purified argon again.

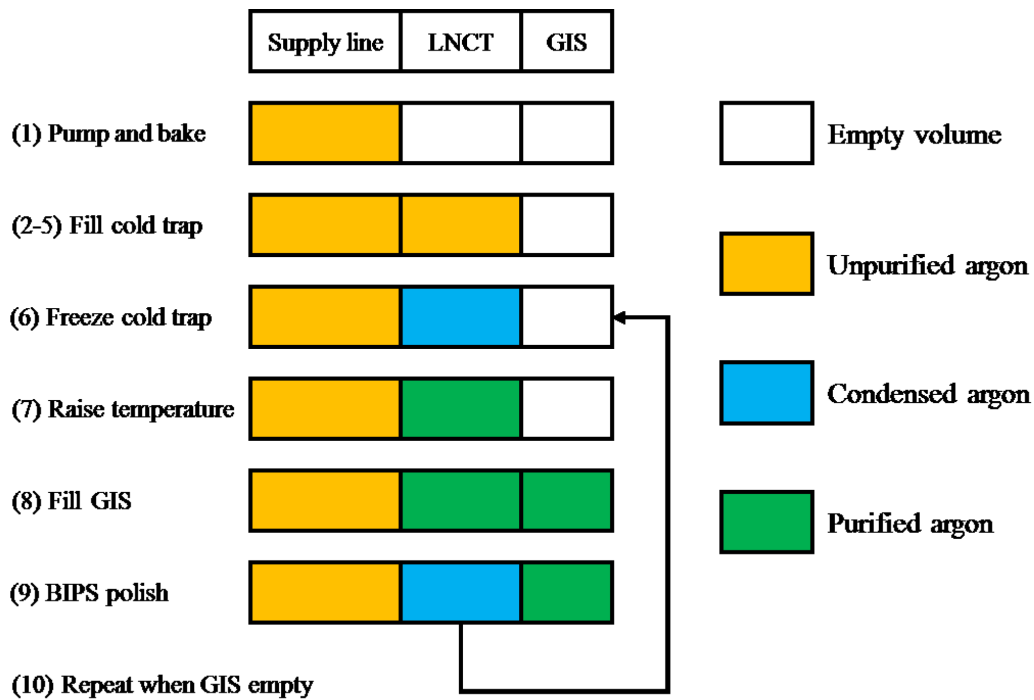

Fig. 4.14 Operation workflow of the BIPS procedure.

Although the experiments with these three specimens follow the same procedure as above, SiOx1 was fixed on a different sample holder from SiPt and SiOx2. Therefore, a sample exchange including chamber venting and re-pumping was performed after the BIPS experiment on specimen SiOx1. The initial argon pressure for each single BIPS experiment was in the range between 2×10^{-5} mbar and 1×10^{-5} mbar, where the pressure drop for a single polish was about 2×10^{-6} mbar. The experiment results are shown below from Figure 4.15 to 4.17 (Stage bias: (a) 300 V, (b) 250 V, (c) 200 V, (d) 150 V, (c) 100 V, (d) 75 V).

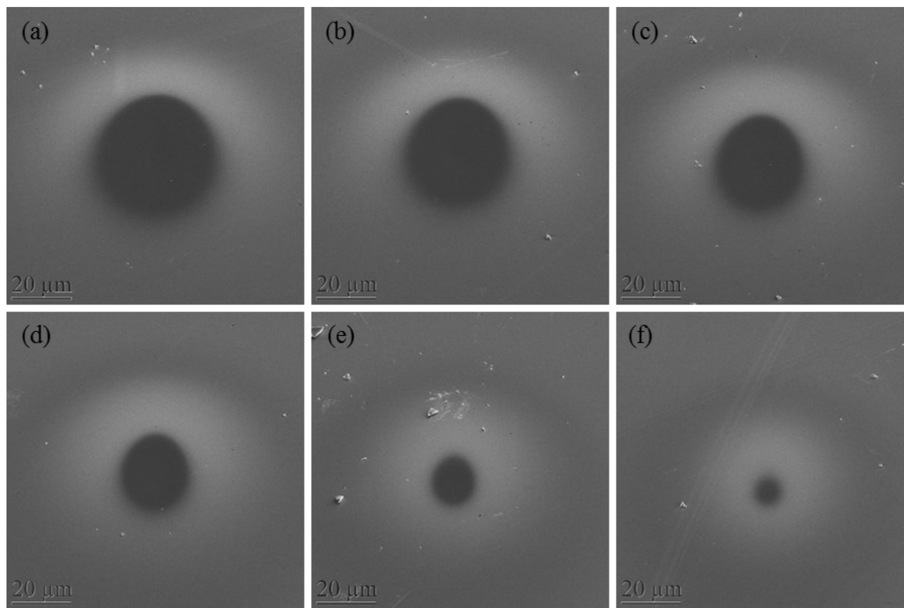

Fig. 4.15 BIPS spots on specimen SiOx1 with varies stage bias from 300 V to 75 V.

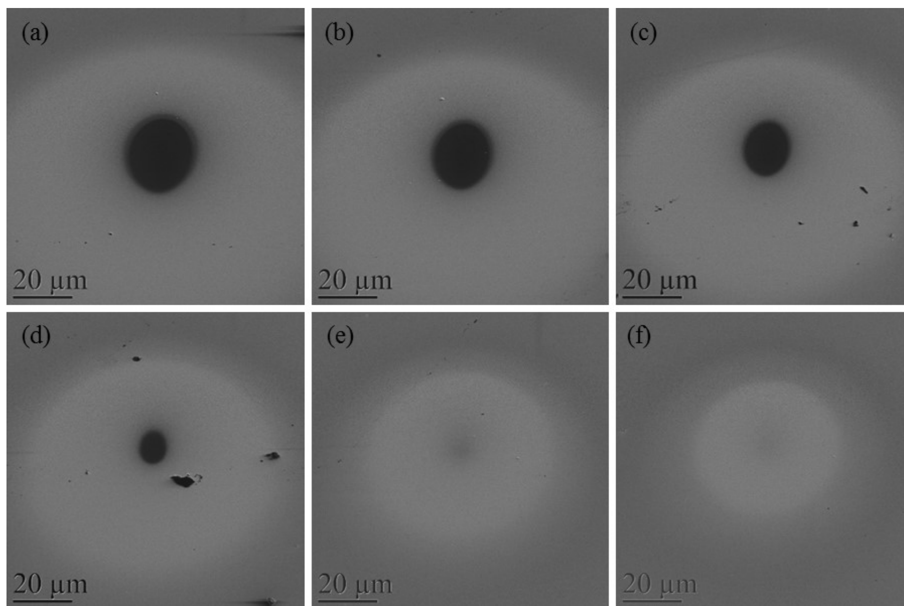

Fig. 4.16 BIPS spots on specimen SiPt with varies stage bias from 300 V to 75 V.

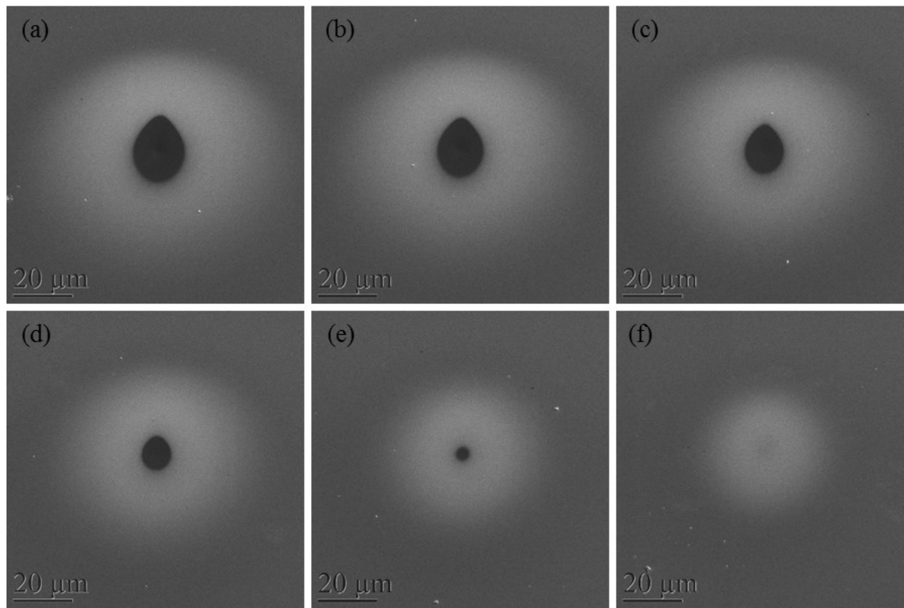

Fig. 4.17 BIPS spots on specimen SiOx2 with varies stage bias from 300 V to 75 V.

References

1. Giannuzzi, L., et al., *Focused ion beam milling and micromanipulation lift-out for site specific cross-section TEM specimen preparation.* MRS Online Proceedings Library Archive, 1997. **480**.

2. Kamino, T., et al., *A FIB micro-sampling technique and a site specific TEM specimen preparation method.* Introduction to Focused Ion Beams, 2005: p. 229-245.

3. Lomness, J.K., L.A. Giannuzzi, and M.D. Hampton, *Site-specific transmission electron microscope characterization of micrometer-sized particles using the focused ion beam lift-out technique.* Microscopy and Microanalysis, 2001. **7**(5): p. 418-423.

4. Klepeis, S., J. Benedict, and R. Anderson, *A grinding/polishing tool for TEM sample preparation.* MRS Online Proceedings Library Archive, 1987. **115**.

5. Huang, Z., *Combining Ar ion milling with FIB lift -out techniques to prepare high quality site -specific TEM samples.* Journal of Microscopy, 2004. **215**(3): p. 219-223.

6. Gatan *Precision Ion Polishing System II Datasheet*. 2015.

7. Pakzad, A. *Argon ion polishing of focused ion beam specimens in PIPS II system*. 2015; Available from: http://www.gatan.com/argon-ion-polishing-focused-ion-beam-specimens-pips-ii-system.

8. Mulders, J. and P. Trompenaars. *An in -situ Low Energy Argon Ion Source for Local Surface Modification*. in *European Microscopy Congress 2016: Proceedings*. 2016. Wiley Online Library.

9. Rasmussen, J., *Gas injection system*. 1995, Google Patents.

10. J. Huang, M.L., J. Mulders, P. Trompenaars, E. Zschech. *Beam induced polishing system and its application on a dual-beam microscope*. in *Microscopy Conference 2017*. 2017. Lausanne.

Chapter 5

Dynamic Binary Collision Approximation and its FIB Application

Experimental methods are intuitive and straightforward to demonstrate the ion-beam induced damage in solids, however, a better understanding of the damage mechanisms can be obtained from model-based simulations considering the basic relationship between ion-beam parameters and the induced damage. Furthermore, if the simulation method can be validated as a trustworthy way to predict such mechanisms, future experimental efforts can be substantially reduced using theoretical predictions or even spared. The only remaining experiments will be for calibration to achieve quantitative agreement between simulation and experiment, which might depend on certain tool parameters.

Several simulation approaches have been used to simulate the ion-solid interaction, which is the fundamental physics of interest in the Focused Ion Beam technique [1-11]. Molecular Dynamics (MD) simulations have been used to investigate the root cause of the Si amorphization at the atomic level. MD simulation is a type of simulation that considers all simulation bodies (atoms) in its computation volume and calculates their physical movements with the influence of the multi-body effect [12, 13]. It is very useful for investigating the fundamental root cause of the damage mechanism. By combining nanometer-scale MD simulations and experiments, *Pastewka et al.* assessed the amorphization of Si under low-voltage FIB milling of 1-5 kV [10].

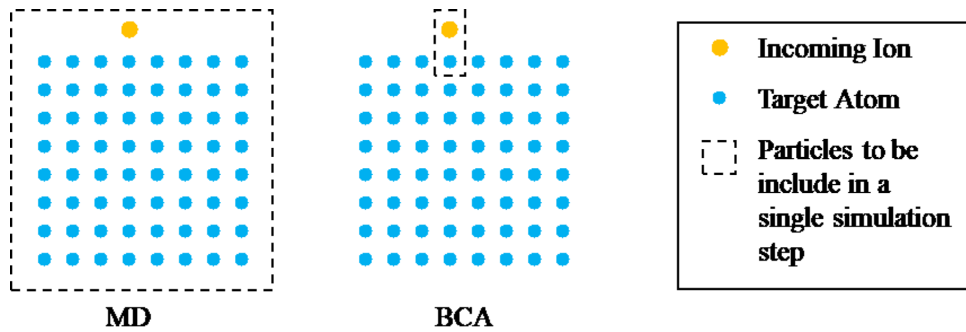

Fig. 5.1 Molecular Dynamics simulation considers all atoms in its computation volume at one calculation step, whereas BCA simulation only considers the two collision particles for a single calculation.

Although MD simulations can provide an insightful understanding of the amorphization mechanism, its significant computational power demand hold back its application-specific usage. Until the desktop computational power/efficiency for micrometer-scale MD simulations can reach a minute-basis, an alternative approach must be found. Binary Collision Approximation (BCA) simulations, on the other hand, are usually preferred for realistic-scale FIB simulations [14]. In contrast to MD simulations, the BCA method does not include the N-body effect in the calculation. Instead, BCA simulations only considers the two collision bodies in each simulation step. The simplified calculation makes it a better candidate to simulate "macro" processes such as micrometer-scale FIB milling, where the focus is beyond atomic level and the duration is usually on a minute scale. BCA simulations have been used to determine sputter yield and surface evolution during FIB induced micro/nano fabrication [6], and to predict the damage from low-dose ion implantation in Si using the damage energy density or the projected ion range in the substrate.

In this study, an extended BCA algorithm that includes dynamic processes during high-dose ion-solid interactions, is used to simulate the FIB process. The conventional

BCA model may face a critical problem for simulating the FIB process since it is characterized and distinguishes itself from other ion-solid interactions (such as ion doping) by a much higher ion dose that alters the substrate properties accordingly. The extended BCA model provides a solution. Since one essential goal is to determine the range of amorphization in silicon caused by the FIB process quantitatively, a validated model for amorphization is needed. Several theoretical models explain the process of ion-beam induced silicon amorphization [15]. In this chapter, an atomic level model that describes the Point Defect Density (PDD) of the FIB-milled substrate, which is further elaborated in the next session, is incorporated into the dynamic BCA simulation to calculate the amorphous layer thickness.

5.1 Ion-beam induced damage generation and accumulation

Depending on the energy transferred from the impacting ions to the target atoms, several types of structural modifications of the solid can occur from the ion-solid interactions. If the energy transferred is higher than a threshold energy, which is sufficient to displace a lattice atom from its original position, a Frenkel pair is created [16]. If the target atom obtains enough kinetic energy to create another Frenkel pair with another atom(s), a collision cascade is formed. For silicon, this threshold energy is between 11 to 30 eV [17-19].

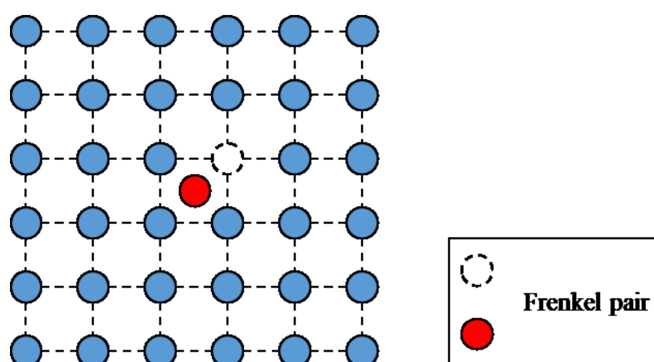

Fig. 5.2 A Frenkel pair is formed when an atom dislocates from its lattice position, creating an interstitial and a vacancy.

On the other hand, if the energy transferred is lower than the threshold energy, only local heating occurs, which is known as the thermal spike regime [13, 15]. In the thermal spike regime, local heating leads to the melting of significant volumes of materials. Although annealing of such melted volumes may recrystallize the material, in case of silicon, the solidification occurs at a rate much larger than the critical velocity for crystallization [15, 20]. Therefore, local melting of the cascade core usually results in

amorphous pockets. Both these two structural changes (Frenkel pairs and amorphous pockets) contribute to the crystalline-amorphous (c-a) transformation.

In the ion-solid interactions among different elements, the dominating c-a transformation can be different. To investigate the primary transformation in the process, MD simulations and BCA codes have been used to estimate the number of atoms displaced by a projectile [21]. MD simulations and BCA codes tend to have different predictions on the number of displaced atoms. BCA codes include merely the moving and stationary atoms in a single collision, whereas MD simulations treat the full dynamics of the collision and are more precise for the low energy regime (<200 eV).

Rutherford backscattering spectroscopy (RBS) and channeling experiments were used to extract the number of silicon atoms displaced from lattice sites at room temperature [15, 22, 23]. For an intermediate mass ion such as gallium, the BCA model predicts a smaller number of displaced silicon atoms at low ion energy regime compared to RBS measurement. However, for an ion energy of 1 MeV, the RBS measurements result in a smaller number of displaced silicon atoms compared to the BCA perdition. This observation indicates that, for gallium-ion-silicon-solid interaction, the silicon c-a transformation is the common result of both Frenkel pair and thermal spike regimes. Depending on the collision conditions, the dominating mechanism may change.

When thermal spike regime dominates the c-a transformation, heterogeneous overlapping of the amorphous pockets is the main cause of the silicon amorphization. But if Frenkel pair generation is dominating the damage production process, silicon

amorphization is a result of homogenous accumulation of the generated point defects, which are the lattice interstitials and vacancies of the Frenkel pairs.

Point defect density (PDD) represents the average atomic density of generated ion-generated point defects in the substrate. It can be used to characterize the c-a transition. At a critical PDD, the material experiences a c-a transition. The PDD can be analytically derived using a diffusion model. By comparing the analytically predicted PDD and the experimental TEM data of an ion-irradiated silicon substrate, Cerva and Hobler concluded the critical PDD of silicon for a c-a transition is 1.15×10^{22} cm^{-3} by finding the same PDD values of the c-a interfaces in the silicon substrate irradiated by different types of ions [24]. That means that the c-a transition occurs in silicon when its PDD is above 1.15×10^{22} cm^{-3}. As it is the property of silicon itself, the value of critical PDD is considered as a constant that does not subject to the collision conditions.

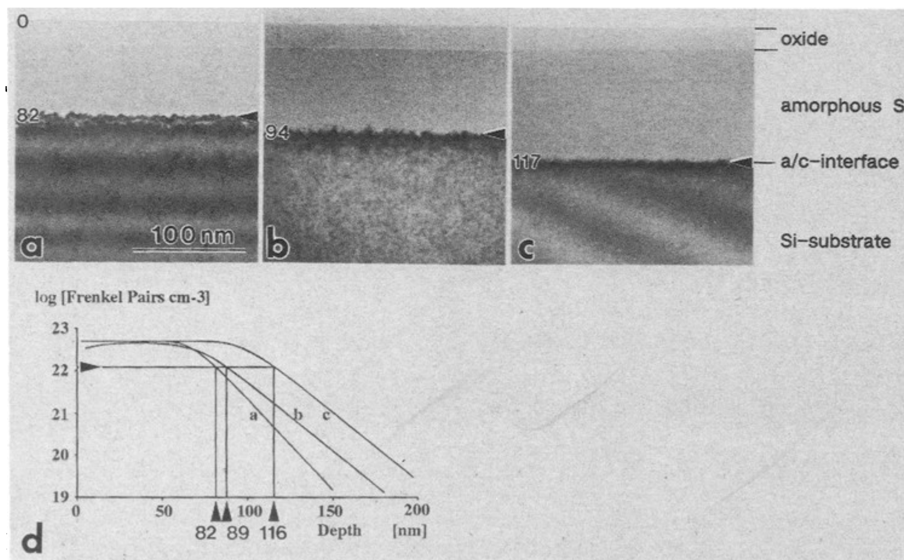

Fig. 5.3 Cerva and Hobler analytically derived the Frenkel Pair density and compared it to experimentally taken TEM images to find the critical Point Defect Density at the c-a interface [24].

5.2 Point Defect Density and Amorphous Layer Thickness

In addition to the analytical derivation of the Point Defect Density of silicon after ion irradiation, Binary Collision Approximation simulation is another approach to provide the distribution of the PDD. As mentioned above, the BCA simulation only considers the two parties in a single collision during each simulation step with a ballistic collision model. By monitoring the energy transferred during the collision and comparing it to the preset threshold energy for atom dislocation from the lattice, the simulation algorithm notes whether a point defect (Frenkel pair) is generated. In the one-dimensional case, the Point Defect Density, D_{pd}, is proportional to the ion dose N_d.

$$D_{pd}(z) = N_d \cdot d(z) \qquad \text{(Eq. 5.1)}$$

$d(z)$ is the number of collision events per unit volume and unit ion dose at substrate depth z, acquired from BCA simulation that exceed the threshold energy for dislocation.

In high dose ion-solid interaction, the probability of a target atom hit by the incoming ion or recoil being already an interstitial is unneglectable. Although this type of collision may have energy transferred higher than the threshold energy to dislocate silicon atoms from lattice, it does not generate a new point defect. It must be singled out from the collision events that generate point defects. The probability of a collision event resulting no new point defect is $D_{pd}(z)/N$. And therefore, the D_{pd} is modified [24-26].

$$D_{pd}(z) = N \cdot \left(1 - e^{-\frac{N_d \cdot d(z)}{N}}\right) \qquad \text{(Eq. 5.2)}$$

where N, the atomic density of silicon in this case, is 5×10^{22} cm^{-3}.

However, if the local Point Defect Density D_{pd} changes dynamically with each ion dose increment ΔN_d, i.e., D_{pd} is a function of both substrate depth z and N_d. $D_{pd}(z, Nd)$ can be given by the following differential equation [27].

$$\frac{\partial D_{pd}(z, N_d)}{\partial N_d} = d(z) \times \left(1 - \frac{D_{pd}}{N}\right) \qquad \text{(Eq. 5.3)}$$

Equation 5.3 reveals that at substrate depth z, the increment of Point Defect Density ΔD_{pd} per ion dose increment ΔN_d is given by the number of collision event times the probability of the event being able to generate a new point defect. The crystal-amorphous interface of the silicon can be found at $z = Z$, where $D_{pd}(Z)$ equals to the critical PDD 1.15×10^{22} cm^{-3}.

5.3 Amorphous layer thickness

TRIM (TRansport of Ions in Matter) is a well-known BCA-based simulation software for ion range and damage calculation in an amorphous material [28, 29]. It has been widely used by industry and academia for decades, providing reliable predictions for low-dose scenarios such as ion doping processes. However, it does not take into account any dynamic alteration of the material at high ion dose irradiation. Significant material transport occurs during the process. Atoms are sputtered away or redeposited at a different location, largely altering the properties of the substrate. As a static BCA approach, TRIM does not include such behaviors. By extending TRIM, TRIDYN (TRansport of Ions including DYNamic composition changes) on the other hand considers the dynamic alterations of local composition that arise from the ion irradiation [30, 31]. With this extended model, dynamic phenomena such as sputter erosion of the surface, atomic mixing and recoil implantation, which all occur to a major extent during the FIB process, are modelled. In TRIDYN, Equation 5.3 is well integrated into the algorithm to record the ion damage, i.e. Point Defect Density, in the substrate. By locating the c-a interface with critical PDD, the amorphous layer thickness can be determined.

In TRIDYN, simulations are performed for a 100-nm thick silicon substrate which is irradiated by gallium ions at 0.2, 0.5, 1, 2, 3, 4, 5, 8, 16 and 30 keV ion energy incident at a 5° glancing angle (85° to surface normal). A dose of 100 ion per nm^2 is set for one complete run. It has been ascertained that this final dose is sufficient to achieve a stationary state at all applied ion energies. In the simulations, there are two energy parameters that have to be paid attention. The displacement threshold energy of silicon,

E_d, which is set to 15 eV in this thesis, is of the most importance. It is the threshold energy for a displacement of an atom from its lattice and a Frenkel pair is generated. Although there is no universal recognized value on the displacement threshold energy of silicon, it is often set to 15 eV for simulations [29]. Naturally, lower E_d generally leads to a higher number of displacement collision events. The cutoff energy, at which the trajectories of ions and recoil atoms are terminated, is set equal to the minimum surface binding energy in the system (i.e. 2.82 eV), to minimize the simulation time. Ideally the cutoff energy should be as low as possible to achieve more accurate results. But setting a value lower than the minimum binding energy in the system, not only significantly increases the simulation efforts but also contributes little to the result accuracy. When a moving ion/atom has a kinetic energy lower than the binding energy of the target atom, no displacement collision will occur.

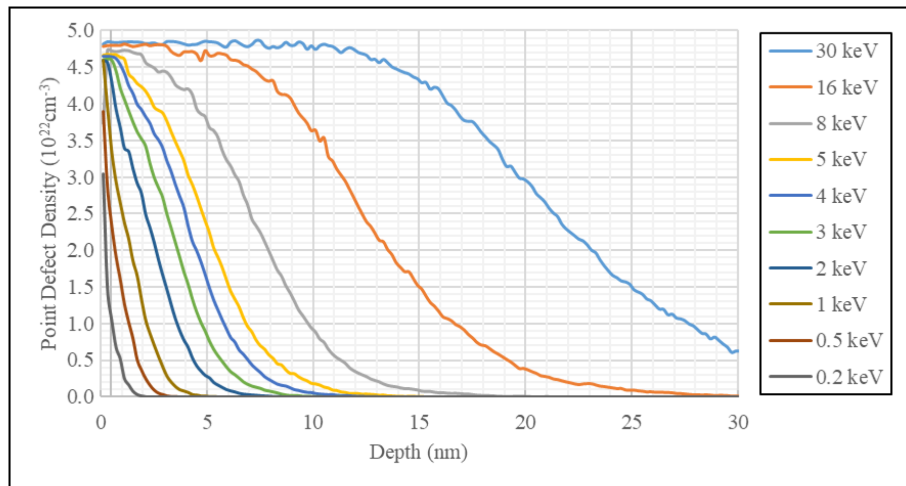

Fig. 5.4 TRIDYN (dynamic BCA) simulated PDD distribution along the depth of a gallium-ion-milled silicon substrate with several ion energies.

The PDD distribution along the substrate depth from 10 TRIDYN simulations are plotted in Figure 4.4, as well as 10 TRIM simulations with the static BCA model using

the same parameters for comparison, plotted in Figure 5.5. Note that although the depth in the two graphs both reflect the same physical value at the end of the simulation, the evolution of the substrate is different. In the static simulation, depth $z = 0$ represent the original substrate surface. It does not change throughout the whole simulation process. In contrast, in the dynamic simulation, the depth $z = 0$ represent an evolving substrate surface. It changes its position to the original surface position because of the surface erosion caused by sputtering during the process.

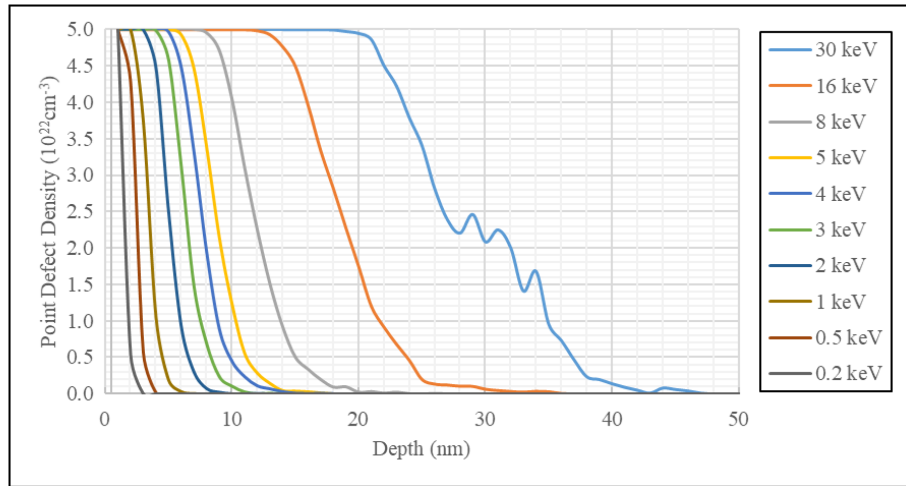

Fig. 5.5 TRIM (static BCA) simulated PDD distribution along the depth of a gallium-ion-milled silicon substrate with several ion energies.

In both figures, the c-a interface is found at depth Z where each PDD distribution meets the critical PDD $D_{pd} = 1.15 \times 10^{22}$ cm^{-3}. The values are show in Table 5.1.

Ga ion energy (keV)	30	16	8	5	4
TRIDYN c-a interface (nm)	26.7	16.1	9.5	6.7	5.7
TRIM c-a interface (nm)	35.0	22.0	14.0	11.0	9.0
Ga ion energy (keV)	3	2	1	0.5	0.2
TRIDYN c-a interface (nm)	4.7	3.5	2.1	1.3	0.5
TRIM c-a interface (nm)	8.0	6.0	4.0	3.0	2.0

Tab. 5.1 C-a interface position predicted by TRIDYN and TRIM simulations for several ion energies, determined by the depth of the critical Point Defect Density.

A gallium ion energy of 30 keV is the mostly used ion energy in FIB applications. The c-a interface in silicon is usually observed between 20 nm and 30 nm in the substrate depth for this ion energy. The static model predicts a Z value (35 nm) outside of this range, whereas the dynamic model predicts a value (26.7 nm) within the experimentally observed range. Although it is premature to say that the TRIDYN value of Z reflects a true prediction of the c-a transition interface without accurate experimental validation, the relatively convincing numbers, compared to what TRIM provides, gives an indication that the TRIDYN model is a better physics-based model for damage prediction of the FIB process.

5.4 Gallium concentration

In addition to silicon amorphization, ion implantation is another most concerned sample modification or damage caused by Focused Ion Beam milling. Gallium is the most commonly used Liquid Metal Ion Source (LMIS) in commercial FIB tools. Implanted gallium can significantly modify the properties of the specimen such as conductivity or the sputter yield under the same FIB conditions. In FIB, gallium ions are accelerated to sputter the specimen atoms away from the substrate, however, the ions are unavoidably implanted into the specimen if their collision path end in the substrate. Depending on the collision and beam conditions, the concentration of the implanted gallium varies. Even if gallium already exists in the original specimen, such implantation could introduce significant property alterations. As a crucial step to systematically reduce the FIB introduced gallium implantation in the specimen using an optimized sample preparation recipe, an accurate estimation of the concentration of implanted gallium is needed.

Similar to predicting the Point Defect Density of a FIB milled substrate, the implanted gallium may not be truly reflected by the conventional static BCA model as it does not simulate the dynamic alternation caused by FIB. In this session, the dynamic BCA model is used to predict the gallium concentration of a gallium-ion-irradiated silicon substrate in a high ion-dose scenario, i.e. using FIB milling.

Figure 5.6 shows the depth profiles of the implanted gallium concentration in a silicon substrate after being irradiated by a dose of 100 gallium ions per nm^2 with a glancing angle of 5° at varies ion energies.

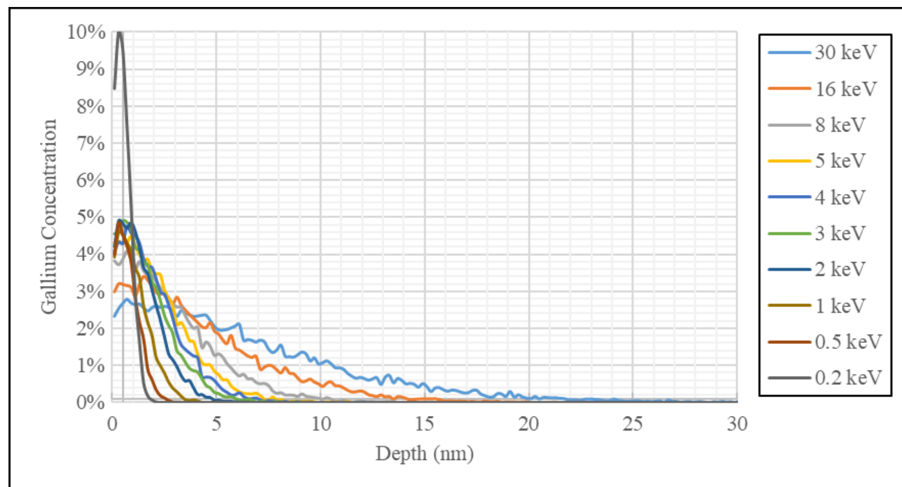

Fig. 5.6 TRIDYN (dynamic BCA) simulated gallium concentration along the depth of gallium-ion-milled silicon substrate with several ion energies.

For comparison, the corresponding depth profiles of implanted gallium simulated by TRIM are plotted in Figure 5.7. Both prediction models show the tendency that the distribution curve becomes steeper as the ion energy lowers. Lower energy FIB milling may implant a higher percentage of gallium into the silicon substrate than the higher ion energy FIB milling, but this higher concentration decays faster along the substrate depth. Despite this similarity, the TRIM simulation results in on average one order of magnitude

higher gallium concentration than the TRIDYN simulations. In practice, FIB sample preparation using a 5-kV ion energy as the last step to remove/reduce the damage of the sample is not unusual. If the TRIM perdition suggests the reality, such doing may leave a gallium implantation of up to 20%, which is a substantial number for a “clean-up” procedure. On the other hand, the TRIDYN predicts a value of 5%, which is relatively an acceptable number.

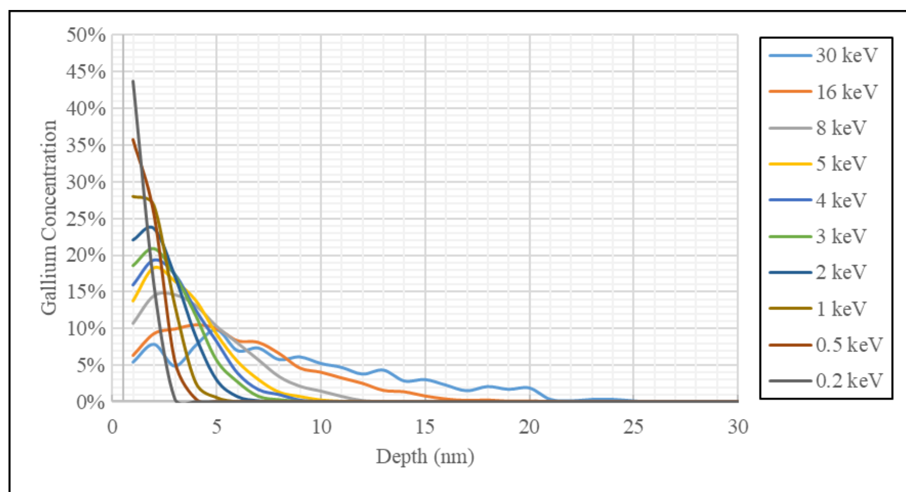

Fig. 5.7 TRIM (static BCA) simulated gallium concentration along the depth of gallium-ion-milled silicon substrate with several ion energies.

5.5 Milling Rate

The optimization of the FIB recipe heavily relies on the needed time to spend on each preparation step in order to employ only the necessary effort for preparation, which is especially important for industrial applications such as process control and physical failure analysis in semiconductor manufacturing. A FIB recipe usually is a series of steps that consist of applying gallium ion beam with decreasing ion energy to the specimen. Gallium ions with lower energy introduce less damage to the specimens, however, the

removal rate of the substrate material, i.e. milling rate, decreases, not to mention the loss of spatial resolution and local dose density due to bigger beam diameter.

To achieve the best compromise for ion energy selection and milling time is a crucial task. If FIB milling with higher ion energy takes too long, undesired damage may affect the region of interest; Instead, if FIB milling with lower ion energy is used to avoid unnecessary damage, it is important to apply it with only the minimum amount of time needed because the preparation time significantly increases for low-energy ion milling.

The development of a time-optimized recipe for TEM lamella preparation needs the input of initial parameters like thickness of the material to be removed, material properties and beam conditions. Among those, the FIB milling rate R should be a constant given in the recipe. It can be experimentally determined. However, R depends on the material system (ion species and substrate materials) and beam conditions. Experimental measurement of the milling rate of all possible cases and parameter space is unrealistic. The determination of R based on simulation, either on the fly or effortlessly setting up a look-up table beforehand, is a practical approach to solve the problem.

The static BCA model is unfortunately unable to accomplish this task. In the static approach, the target material is considered to be intact as in its original state in the beginning of each ion irradiation. The calculation of the removal rate R however requires the relationship establishment between the progressing ion dose and the substrate material quantity, i.e., substrate surface regression. On the other hand, apart from being able to dynamically alter the target material properties per ion dose increment, the dynamic BCA model can also trace the eroded target surface position. The eroded surface is the result

of sputtering from the ion bombardment. By tracing the distance of target surface with respect to its original position at each ion dose increment, the unit milling rate R at a certain beam condition in the material system can be simulated.

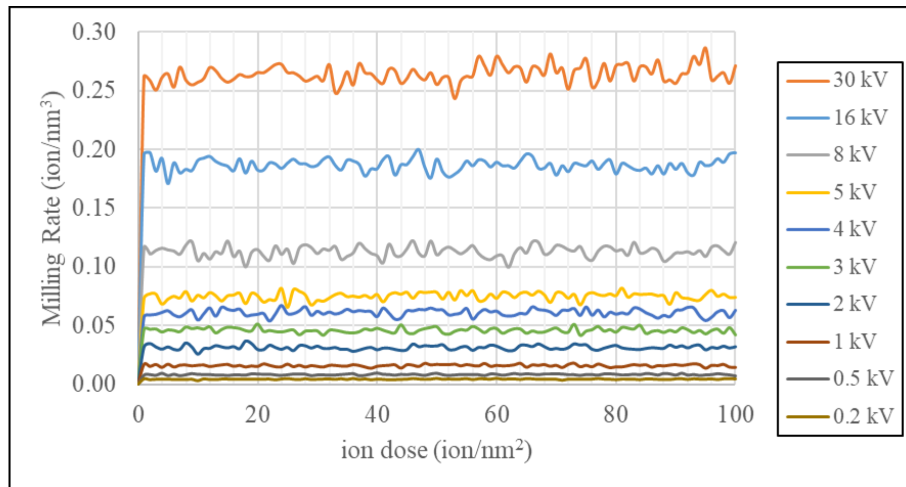

Fig. 5.8 Milling rate of gallium ions on silicon substrate in progression of the ion dose in the TRIDYN simulation with several ion energies in 5° glancing angle.

Figure 5.8 shows the milling rate progressions in TRIDYN simulations. The silicon substrate was simulated to be milled by gallium ions with several ion energies with a 5° glancing angle. The milling rate reaches to a stable value right at the beginning of each simulation and remains stable throughout the simulation process with an insignificant deviation.

Ion energy (keV)	**30**	**16**	**8**	**5**	**4**
R (ion/nm²)	0.264	0.187	0.113	0.076	0.061
σ (×10⁻³ ion/nm²)	7.5	5.4	4.8	3.3	2.9
Ion energy (keV)	3	2	1	0.5	0.2
R (ion/nm²)	0.046	0.031	0.016	0.009	0.005
σ (×10⁻³ ion/nm²)	2.1	1.8	1.0	0.6	0.3

Tab. 5.2 Mean milling rate R and its standard deviation with corresponding ion energy in mentioned TRIDYN simulations.

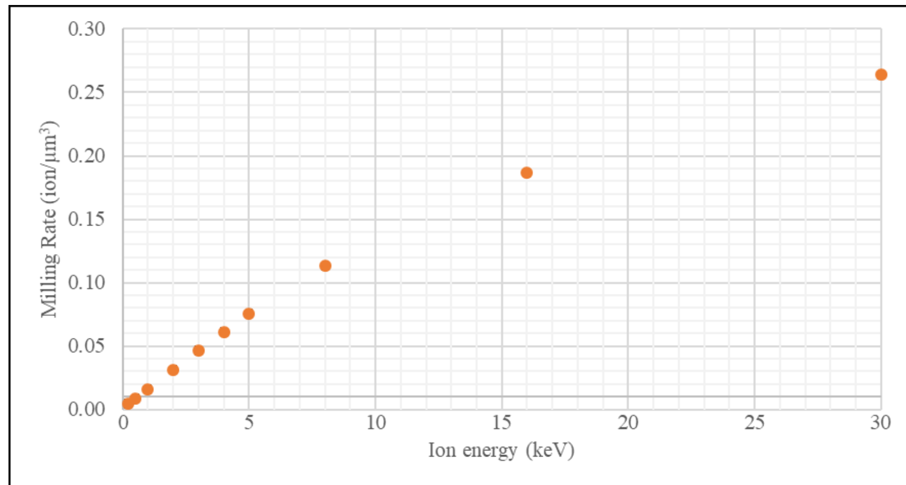

Fig. 5.9 Milling rate of several ion energy are plotted and suggests a near logistic distribution, which implies a potential physical limit.

Figure 5.9 plots the mean value of the Milling Rate R with the mentioned simulation conditions corresponding to each simulated ion energy. The distribution within the energy range shows a linearity for low energies and an exponential saturation for high energies. Such distribution could be described with a logistic function, which indicates there might be a potential physical limit of the Milling Rate described by the maximum value of the logistic function.

References

1. Barone, M.E. and D. Maroudas, *Defect-induced amorphization of crystalline silicon as a mechanism of disordered-region formation during ion implantation.* Journal of Computer-Aided Materials Design, 1997. **4**(1): p. 63-73.

2. Caturla, M.-J., et al., *Ion-beam processing of silicon at keV energies: A molecular-dynamics study.* Physical Review B, 1996. **54**(23): p. 16683.

3. De La Rubia, T.D. and G. Gilmer, *Structural transformations and defect production in ion implanted silicon: A molecular dynamics simulation study.* Physical review letters, 1995. **74**(13): p. 2507.

4. Eckstein, W., *Computer simulation of ion-solid interactions*. Vol. 10. 2013: Springer Science & Business Media.

5. Hofsäss, H., K. Zhang, and A. Mutzke, *Simulation of ion beam sputtering with SDTrimSP, TRIDYN and SRIM.* Applied Surface Science, 2014. **310**: p. 134-141.

6. Kim, H.-B., et al., *Simulation of ion beam induced micro/nano fabrication.* Journal of Micromechanics and Microengineering, 2007. **17**(6): p. 1178.

7. McCaffrey, J., M. Phaneuf, and L. Madsen, *Surface damage formation during ion-beam thinning of samples for transmission electron microscopy.* Ultramicroscopy, 2001. **87**(3): p. 97-104.

8. Narayan, J., et al., *Atomic structure of ion implantation damage and process of amorphization in semiconductors.* Journal of Vacuum Science & Technology A: Vacuum, Surfaces, and Films, 1984. **2**(3): p. 1303-1308.

9. Nordlund, K., et al., *Defect production in collision cascades in elemental semiconductors and fcc metals.* Physical Review B, 1998. **57**(13): p. 7556.

10. Pastewka, L., et al., *Surface amorphization, sputter rate, and intrinsic stresses of silicon during low energy Ga+ focused-ion beam milling.* Nuclear Instruments and Methods in Physics Research Section B: Beam Interactions with Materials and Atoms, 2009. **267**(18): p. 3072-3075.

11. Smith, R., *Atomic and ion collisions in solids and at surfaces: theory, simulation and applications*. 2005: Cambridge University Press.

12. Alder, B.J. and T.E. Wainwright, *Studies in molecular dynamics. I. General method.* The Journal of Chemical Physics, 1959. **31**(2): p. 459-466.

13. Nastasi, M., J. Mayer, and J.K. Hirvonen, *Ion-solid interactions: fundamentals and applications*. 1996: Cambridge University Press.

14. Robinson, M.T. and I.M. Torrens, *Computer simulation of atomic-displacement cascades in solids in the binary-collision approximation.* Physical Review B, 1974. **9**(12): p. 5008.

15. Pelaz, L., L.A. Marqués, and J. Barbolla, *Ion-beam-induced amorphization and recrystallization in silicon.* Journal of applied physics, 2004. **96**(11): p. 5947-5976.

16. Emtsev, V., T. Mashovets, and V. Mikhnovich, *Frenkel pairs in germanium and silicon.* Soviet Physics-Semiconductors, 1992. **26**(1): p. 12-25.

17. Loferski, J. and P. Rappaport, *Electron voltaic study of electron bombardment damage and its thresholds in ge and si.* Physical Review, 1955. **98**(6): p. 1861.

18. Sayed, M., et al., *Computer simulation of atomic displacements in Si, GaAs, and AlAs.* Nuclear Instruments and Methods in Physics Research Section B: Beam Interactions with Materials and Atoms, 1995. **102**(1-4): p. 232-235.

19. Kerbiriou, X., et al., *Silicon displacement threshold energy determined by electron paramagnetic resonance and positron annihilation spectroscopy in cubic and hexagonal polytypes of silicon carbide.* Journal of nuclear materials, 2007. **362**(2-3): p. 202-207.

20. Brown, R., D. Maroudas, and T. Sinno, *Modelling point defect dynamics in the crystal growth of silicon.* Journal of crystal growth, 1994. **137**(1-2): p. 12-25.

21. Bukonte, L., et al., *Comparison of molecular dynamics and binary collision approximation simulations for atom displacement analysis.* Nuclear Instruments and Methods in Physics Research Section B: Beam Interactions with Materials and Atoms, 2013. **297**: p. 23-28.

22. Christel, L., J. Gibbons, and T. Sigmon, *Displacement criterion for amorphization of silicon during ion implantation.* Journal of Applied Physics, 1981. **52**(12): p. 7143-7146.

23. García, L.J., et al., *Monte Carlo simulation of silicon atomic displacement and amorphization induced by ion implantation.* Journal of Applied Physics, 2011. **109**(12): p. 123507.

24. Cerva, H. and G. Hobler, *Comparison of transmission electron microscope cross sections of amorphous regions in ion implanted silicon with point-defect density calculations.* Journal of The Electrochemical Society, 1992. **139**(12): p. 3631-3638.

25. Hobler, G. *Net point defect concentrations after ion implantation in silicon*. in *The 4th International Symposium on Process Physics and Modeling in Semiconductor Technology*. 1996. Los Angeles.

26. Hobler, G., *Simulation der Ionenimplantation in ein-, zwei- und dreidimensionalen Strukturen*. 1988, Technische Universitaet Wien. p. 372.

27. Huang, J., et al., *Si amorphization by focused ion beam milling: Point defect model with dynamic BCA simulation and experimental validation.* Ultramicroscopy, 2018. **184**: p. 52-56.

28. Biersack, J.P. and L. Haggmark, *A Monte Carlo computer program for the transport of energetic ions in amorphous targets.* Nuclear Instruments and Methods, 1980. **174**(1-2): p. 257-269.

29. Ziegler, J.F., M.D. Ziegler, and J.P. Biersack, *SRIM–The stopping and range of ions in matter (2010).* Nuclear Instruments and Methods in Physics Research Section B: Beam Interactions with Materials and Atoms, 2010. **268**(11-12): p. 1818-1823.

30. Möller, W., W. Eckstein, and J. Biersack, *Tridyn-binary collision simulation of atomic collisions and dynamic composition changes in solids.* Computer Physics Communications, 1988. **51**(3): p. 355-368.

31. Möller, W. and W. Eckstein, *Tridyn—A TRIM simulation code including dynamic composition changes.* Nuclear Instruments and Methods in Physics Research Section B: Beam Interactions with Materials and Atoms, 1984. **2**(1-3): p. 814-818.

Chapter 6

Discussion and Conclusions

Experimental data and simulation results of three addressed aspects in Focused Ion Beam sample preparation - material removal (milling) rate, ion implantation and material amorphization - have been presented in this thesis. These experiments and simulations are subjected to FIB conditions for advanced low-damage preparation. Typical features are the use of multiple ion energies, high incident angle and high ion dose, which distinguish them from scenarios typical for ion doping processes. In this chapter, experimental data and simulation results are discussed individually and together, to demonstrate that the systematic approach that has been performed in this thesis is suitable for advanced FIB applications that require low sample damage.

Issues and challenges mentioned in the motivation are reviewed, and in addition, conclusions are derived. At the end and outlook is given for further advanced in FIB sample preparation.

6.1 Discussion of Experiments and Simulations

6.1.1 FIB milling rate

In chapter 2, a simple and efficient method was used to measure the gallium ion FIB milling rate for a silicon specimen at several accelerating voltages. Eight experiments were performed and twenty-four measurements were adopted. The corresponding milling rate was calculated by measuring the depth of the FIB-created pattern and by normalizing it with the applied dose. Such a dose-based unit is preferred against a time-based unit such as nm per second. It can avoid the inconvenience of multiple beam current selection and beam blanks in the actual FIB applications.

In chapter 4, the dynamic Binary Collision Approximation algorithm TRIDYN is performed to simulate the surface recession in the FIB conditions. Therefore, the milling rate was determined by the recessed surface normalized by the simulated ion dose. The TRIDYN version used in this thesis supports merely one-dimensional simulation. Three-dimensional effects are not taken into consideration. That means, no ion beam scanning pattern was simulated, which facilitates the sputtering during the actual FIB milling.

The FIB milling rate depends on the FIB conditions such as ion energy, ion species, substrate material, incident angle, etc. A scanning strategy for FIB milling is always tailored and optimized for specific materials and applications. This strategy defines how the ion beam moves from one location to another one within the defined milling pattern. The total milling rate can be improved because each individual scan spot has an optimal incident angle locally, which is different from the angle between the incident ion and the

sample surface. This practical improvement of the scanning strategy is unable to be simulated in the one-dimensional algorithm. However, it becomes less significant if the ion energy is low. The ion beam size increases with lower ion energy. For an ion beam size comparable to the defined milling pattern, the change of the local incident angle is no longer prominent.

Figure 6.1 shows both the experimentally determined gallium FIB milling rate of a silicon substrate and the TRIDYN predicted milling rate for several ion energies. A systematic underestimation of the milling rate from simulation is clearly seen for ion energies above 1 keV. This difference can be caused by simulating only a one-dimensional FIB milling process which is an approximation.

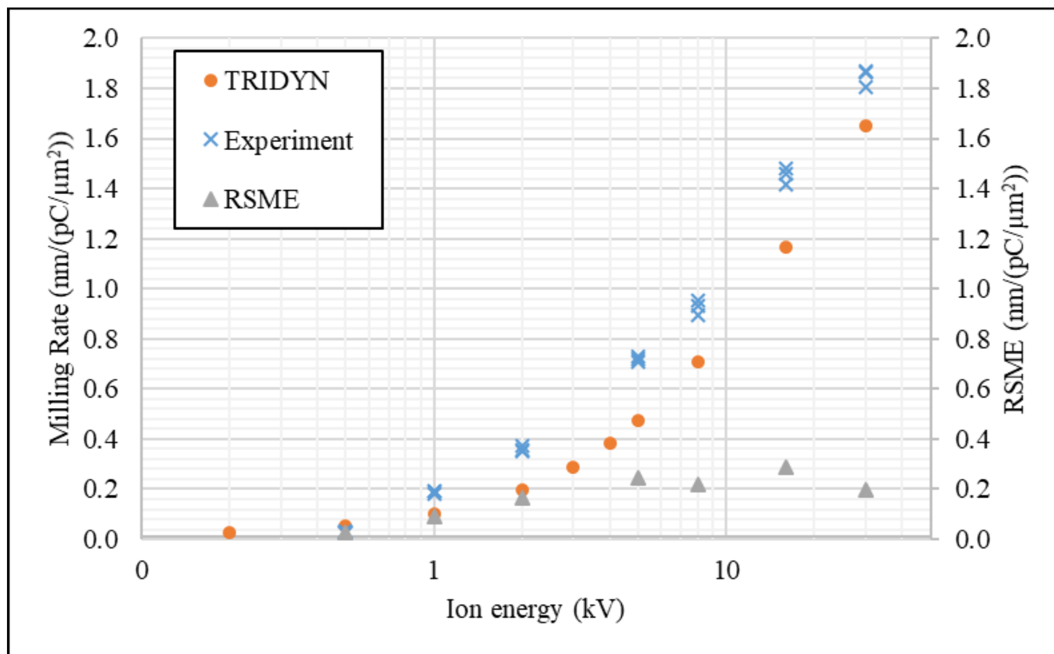

Fig. 6.1 Experimental gallium FIB milling rate and the TRIDYN calculated prediction as a function of the ion energy.

This explanation can be verified by introducing a three-dimensional simulation to the TRIDYN algorithm. However, the low root-mean-square error (RMSE) of below

0.4 nm/(pC/μm^2) proofs that the dynamic BCA model (TRIDYN algorithm) is already well applicable to predict the FIB milling rate. It is essentially advantageous compared to the conventional model (TRIM algorithm) which is unable to trace the progressively moving substrate surface.

6.1.2 Gallium Ion Implantation

In chapter 2, the FIB-induced gallium ion implantation is investigated with Atom Probe Tomography. Benefiting from the fact that FIB is one of the most common techniques for APT sample preparation, no additional analytical techniques or special designed experiments were needed. Crystalline silicon specimens were prepared with FIB for APT experiments to study the three-dimensional distribution of gallium ions in the silicon specimen, implanted during the sample preparation process. Three sets of tomography data were successfully acquired, and the gallium distributions of arbitrary sampling volumes were extracted.

In Chapter 4, the dynamic BCA-based algorithm TRIDYN was used to simulate the FIB process and to predict the gallium ion concentration in the silicon substrate. Like the predicted PDD distribution, the predicted gallium concentration along the substrate depth shows a significant difference between the dynamic and static approaches (TRYDYN versus TRIM) for identical FIB conditions.

Ion energy (keV)	30	16	8	5	4	3	2	1	0.5	0.2
TRIDYN	3%	3%	4%	4%	5%	5%	5%	5%	5%	10%
TRIM	10%	11%	15%	18%	19%	21%	24%	28%	36%	44%

Tab. 6.1 Peak concentration of gallium in the silicon substrate predicted by TRIDYN and TRIM for identical FIB conditions.

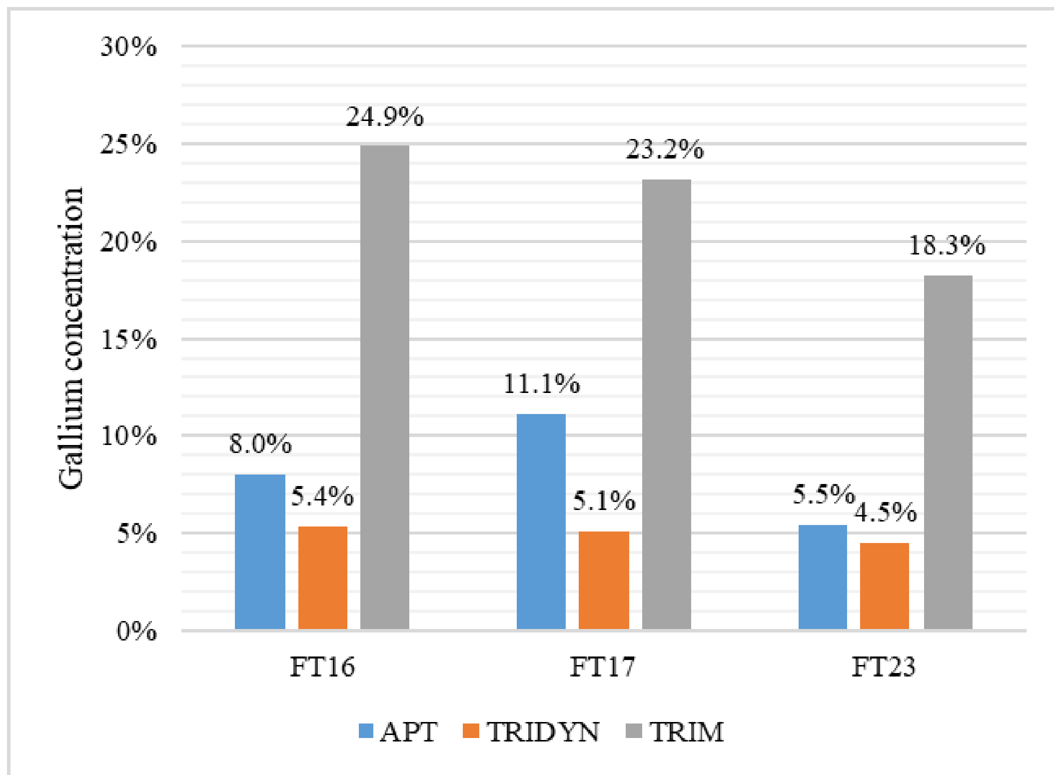

Fig. 6.2 Peak gallium concentration based on APT experiments for three specimens, and the corresponding TRIDYN and TRIM simulation results.

For the three specimens, Figure 6.2 shows the measured peak gallium concentration from APT tomography data and the predictions from TRIDYN and TRIM simulations, respectively. It shows a good consistency of TRIDYN predictions and APT experimental results, with a RMSE less than 6%, whereas in contrast, TRIM shows a much higher predicted value with an error of about 17%. This proofs that the dynamic BCA model is eligible to describe the gallium ion depth distribution in silicon substrate, implanted by FIB.

6.1.3 FIB-Induced Silicon Amorphization

In chapter 2, silicon amorphization caused by FIB milling is examined using Transmission Electron Microscopy. Crystalline silicon specimens were prepared using FIB to a certain geometry that enables TEM to visualize the FIB induced amorphization on the silicon specimens. After the images of the amorphous region had been acquired, a systematic method with classical edge detection algorithm was used to determine the location of the crystalline-amorphous interface of the silicon. This method avoids errors caused by human intervention, and consequently, it provides the basis for an increased level of automation of the analysis procedure.

In chapter 4, the dynamic BCA-based TRIDYN algorithm was used to simulate the FIB process. It was shown that under typical FIB conditions (high ion dose and high incident angle), TRIDYN and its static origin TRIM predict different distributions of the Point Defect Density in the silicon substrate. Using a critical PDD of 1.15×10^{22} cm^{-3}, the prediction of the c-a interface (i.e. amorphous layer thickness) from both TRIDYN and TRIM simulations were deducted from the respective PDD distributions. Because of the difference between the PDD distributions for these two algorithms, the predicted thickness from TRIM simulations was about 30% higher than that from TRIDYN simulations.

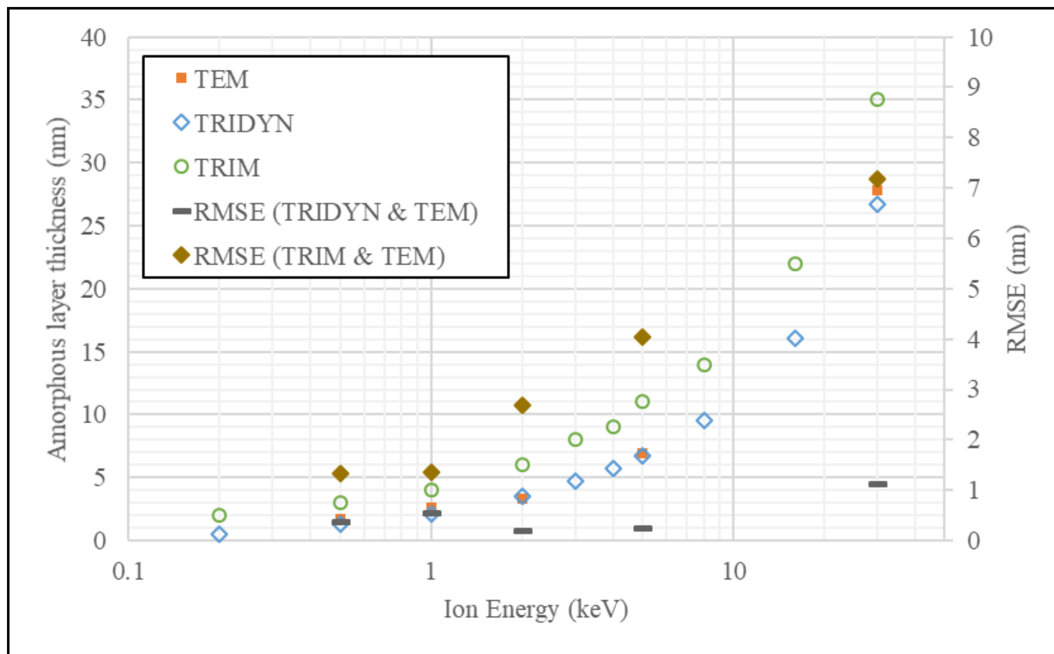

Fig. 6.3 Experimentally determined and TRIDYN/TRIM predicted FIB-induced amorphous layer thicknesses of silicon as a function of ion energy for identical beam conditions.

Figure 6.3 shows the FIB-induced amorphization layer thickness determined from TEM experiments and predicted from TRIDYN/TRIM simulations as a function of the ion energy, for identical beam conditions. Comparing to the experimental values, the TRIM simulation clearly overestimates the amorphous layer thickness, with a maximum RMSE up to 7.2 nm. On the other hand, the predicted amorphous layer thickness data from the dynamic approach simulation, TRIDYN, is in a much better agreement with the experiments, with RMSEs below 1.1 nm.

6.1.4 Reduced Sample Damage and Optimization of FIB Sample Preparation

At the beginning of this thesis, it was mentioned that it is a well-accepted practice to use multiple ion energies in the FIB sample preparation process, in order to achieve

minimum final damage in a reasonable period of time. Higher ion energy FIB milling removes material rapidly while lower ion energy FIB milling refines the result. The key of an advanced FIB sample preparation recipe for a certain application is to find the minimum total sample preparation time by optimizing each preparation (ion energy) step. The optimization contains multiple FIB parameters for the successive preparation procedure, which ideally should be predicted from the before-mentioned and validated dynamic BCA model, given the FIB conditions.

The optimization process is explained below from Equations 6.1 to 6.5. Considering t is the time to be spent for a certain ion energy of FIB milling, given by:

$$t = (D - d) \cdot R^{-1} \quad \text{(Eq. 6.1)}$$

D is the depth of the material to be removed before reaching the ROI. d is the damage layer thickness. Depending on the application, d can be the amorphous layer thickness, the depth of maximum ion implant concentration allowed or the maximum of the two. R is the FIB milling rate per unit time for certain FIB milling conditions.

The total FIB milling time T is given by:

$$T = \sum_{i=1}^{N} t_N \quad \text{(Eq. 6.2)}$$

N is the number of ion energies used in the recipe, descending according to the energy level. It is determined by the damage layer thickness d_N for the lowest ion energy.

$$t_i = \begin{cases} (D - d_1) \cdot R_1^{-1}, & i = 1 \\ (d_{i-1} - d_i) \cdot R_i^{-1}, & i > 1 \end{cases} \quad \text{(Eq. 6.3)}$$

In practice, N is usually between 2 and 5, with the initial ion energy of 30 keV (for $i = 1$). Equation 5.4 provides the relationship between the milling rate per unit dose and area r, milling rate per unit time R with respect to a certain ion beam current I and milling area A. The total FIB milling time T can be easily calculated with recursion.

$$R = r \cdot I \cdot A \quad \text{(Eq. 6.4)}$$

Therefore,

$$t_i = \begin{cases} (D - d_1) \cdot (r_1 \cdot I_1 \cdot A)^{-1}, & i = 1 \\ (d_{i-1} - d_i) \cdot (r_i \cdot I_i \cdot A)^{-1}, & i > 1 \end{cases} \quad \text{(Eq. 6.5)}$$

In applications, the damage layer thickness after FIB milling using the lowest ion energy, d_i, is defined according to the application requirements. By referring d_i to the dynamic BCA simulation model, the maximum allowed ion energy when $i = N$ is found. The choice of N is somehow arbitrary and paradoxical. Reducing N simplifies the recipe. However, the total preparation time T might increase if $r_i \ll r_1$, although increasing I_i may in turn mitigate the problem. Nevertheless, the optimized FIB recipe with the individual time for each step and with the total preparation time is obtained.

For an advanced operation, if the damage layer should be as thin as possible for applications like ultra-thin TEM lamella preparation, the BIPS procedure can be included in the optimized recipe as the last step.

6.2 Conclusions

This thesis has focused on the Focused Ion Beam (FIB) technology using an advanced sample preparation methodology to mitigate the material damage. An experimentally validated model has been used for simulation (BCA-based TRIDYN algorithm) to predict FIB milling rate, ion implantation and material amorphization in FIB applications. Together with a novel design of an in-situ ion polishing system, optimized FIB sample preparation recipes can be developed systematically and efficiently, for both materials science and increasingly demanding semiconductor applications.

At the beginning of this thesis, we have stated that novel FIB applications, particularly in semiconductor industry, posted new challenges to optimize sample preparation recipes. In this thesis, several aspects of the FIB applications were addressed, and the following parameters were studied systematically: milling rate, amorphization and ion implantation. SEM, TEM and APT experiments were designed and executed, to provide a feasible and efficient way to evaluate these parameters quantitatively. The introduction of the dynamic BCA model and the resulting application of the TRIDYN algorithm for simulation brought the recipe optimization for sample preparation to the next level. Based on a comparison of the model predictions with the experimentally determined data, the BCA-based TRIDYN algorithm was validated. That means, simulations based on TRIDYN provide reliable input for FIB recipes. Such a forecast is extremely valuable for novel applications and new materials. Invaluable time can be saved from trials of FIB experiments of untested materials.

The preparation of samples with low damage can be optimized further using an in-situ beam-induced ion polishing system (BIPS) which was implemented into a dual-beam SEM/FIB system. Such a BIPS system provides the possibility to include an extra in-situ operation in the recipe, to remove the remaining FIB-induced damage, for applications with extreme requirements to sample quality, e.g. for ultrathin TEM lamellae in semiconductor industry. Moreover, with BIPS, the FIB systems are empowered with the ability of advanced micro-fabrications like local surface modification, prism surface preparation or ultra-thin TEM lamella preparation.

Other than providing a systematic methodology to achieve damage-reduced optimized FIB sample preparation recipes, this thesis brings the FIB operation closer to a full automation level. FIB recipes can be generated without human intervention and automation-scripting of the FIB tools will be able to adopt those recipes to achieve unattended operations. Such an advanced Focused Ion Beam technology is a significant part of highly automated microscopic analysis. This thesis provides a contribution to realize this goal.

JIN HUANG

Contact

jin.huang@gmx.com

Work Experience

Reliability Engineer | Infineon Technologies AG, Munich
From 01.2019

Wissenschaftlicher Mitarbeiter | TU Dresden, Germany
11.2013 – 06.2018

- Dresden Center for Nanoanalysis (DCN) & Center for Advancing Electronics Dresden (cfaed)
- BMBF project: Material integration and kinetics of reliability-limiting degradation mechanisms in 1D-electronic systems
- Optimization of equipment for material characterization and modification in cooperation with project partner (Beam Induced Polishing System)

Intern | Globalfoundries, Dresden, Germany
06.2012 – 08.2012

- Physical failure analysis of semiconductor devices (CMOS 32nm technology)
- Electron Backscatter Diffraction analysis
- Defect analysis of metal contacts and optimization of the analysis with Focused-Ion-Beam Microscope

Intern | UC Web (Alibaba Group), Guangzhou, China
04.2007 – 06.2007

- Big Data Analysis for UX improvement on mobile devices

Education

Doctor of Philosophy | TU Dresden, Dresden, Germany
11.2013 – 12.2018

- Faculty of Electrical and Computer Engineering
- Thesis: “Advanced Focused Ion Beam: Preparation Optimization and Damage Mitigation”
- High resolution 3D X-ray tomography
- Nanocharacterization with Atom Probe Tomography
- Conducting training on operation of SEM/FIB microscopes
- Creating automated operation scripts
- Presentations on international conferences, e.g. Germany, Switzerland, Austria and USA

Master of Science | Masdar Institute, Abu Dhabi, UAE
GPA: 3.88 out of 4.0 (with Honorable Mention Award)
09.2011 – 06.2013

- Department: Microsystem Engineering
- Thesis: “Novel Fiber Optic Sensors: from 2D Surface Strain Mapping to Picolitre-Volume Fluid Monitoring”
- Microfabrication of structured glass fibers

- Cleanroom experience
- Optical backscatter (Rayleigh) measurement with optical fibers to characterize mechanical stress / deformation
- Finite Difference Time Domain (FDTD) simulation
- Project on Sustainable Energy Management: Energy Autonomous Household
- Presentations on international conferences, e.g. Singapore, Japan

Bachelor of Engineering | Guangdong University of Technology, Guangzhou, China

GPA: 90% out of 100% (top 2% of class, awarded scholarship)
09.2007 – 06.2011

- Major: Electronic Information Science and Technology (ECE)
- Member of student union: Liaison and PR for commercial sponsorship and event organization
- Freescale Smart Car Contest: Autonomous Race Car - Embedded System Programming, Hardware Realization and Image Recognition
- Courses: Analog and Digital Circuit Design, Computer Aided Design with AutoCAD, Digital Signal Processing, Computer Architecture, etc.

Skills

Technology & Fundamentals

- Broad knowledge of microelectronics, semiconductor fabrication physics, optics / photonics and ion-solid interactions
- Over 4 years of experience on electron microscopy (SEM/FIB)
- Experience of characterization, verification and testing of new concepts and hardware designs on SEM/FIB instrumentation
- Statistical data processing of experiment measurements
- Machine Learning and Deep Learning with neural networks

Programming

- Embedded system programming on different microcontroller platforms, e.g. ARM-based, Xilinx FPGA.
- Object-oriented Programming for app development
- Compile languages, VHDL, Python, C/C++/Object C, JAVA and MATLAB
- Ab initio and Monte Carlo Simulations: SRIM (Stopping and Range of Ions in Matters), MEEP (MIT Electromagnetic Equation Propagation)
- Distributed Video Coding in Wireless Sensor Networks (ZigBee): Embedded System Programming
- Feature Recognition on SEM Images with DNN: Python, OpenCV, Caffe, TensorFlow

Communication & Management

- Experience of working in an intensive multi-cultural team environment.
- Experience of presentations to international audience overseas.
- Experience of providing introduction level training on microscopes at a university lab.
- Project experience: Establishment of sensor system, own Apple iOS App development (Offer24, Oppointo)

Languages

- Chinese (Mandarin and Cantonese): native
- English: C2 professional
- German: B1 intermediate